TURBULENCE GENERATION USING LOCALIZED SOURCES OF ENERGY: DIRECT NUMERICAL SIMULATIONS AND THE EFFECTS OF THERMAL NON-EQUILIBRIUM

A Dissertation

by

AGUSTIN FRANCISCO MAQUI

Submitted to the Office of Graduate and Professional Studies of
Texas A&M University
in partial fulfillment of the requirements for the degree of

DOCTOR OF PHILOSOPHY

Chair of Committee,	Diego A. Donzis
Committee Members,	Rodney D. W. Bowersox
	Simon W. North
	Sharath S. Girimaji
Head of Department,	Rodney D. W. Bowersox

May 2016

Major Subject: Aerospace Engineering

ABSTRACT

Turbulence in high-speed flows is an important problem in aerospace applications, yet extremely difficult from a theoretical, computational and experimental perspective. A main reason for the lack of complete understanding is the difficulty of generating turbulence in the lab at a range of speeds which can also include hypersonic effects such as thermal non-equilibrium. This work studies the feasibility of a new approach to generate turbulence based on laser-induced photo-excitation/dissociation of seeded molecules. A large database of incompressible and compressible direct numerical simulations (DNS) has been generated to systematically study the development and evolution of the flow towards realistic turbulence. Governing parameters and the conditions necessary for the establishment of turbulence, as well as the length and time scales associated with such process, are identified. For both the compressible and incompressible experiments a minimum Reynolds number is found to be needed for the flow to evolve towards fully developed turbulence. Additionally, for incompressible cases a minimum time scale is required, while for compressible cases a minimum distance from the grid and limit on the maximum temperature introduced are required. Through an extensive analysis of single and two point statistics, as well as spectral dynamics, the primary mechanisms leading to turbulence are shown. As commonly done in compressible turbulence, dilatational and solenoidal components are separated to understand the effect of acoustics on the development of turbulence. Finally, a large database of forced isotropic turbulence has been generated to study the effect of internal degrees of freedom on the evolution of turbulence.

To my father,

my great inspiration who made this all possible.

ACKNOWLEDGEMENTS

This work was supported by the Airforce Office of Scientific Research (Grant No. FA9550-12-1-0443). The computational resources of Extreme Science and Engineering Discovery Environment (XSEDE), Texas Advanced Computing Center (TACC - University of Texas at Austin), and Texas A&M Supercomputing Facility were used to perform the simulations presented.

I would like to express my deepest gratitude to my advisor, Professor Donzis, for guiding me through my PhD. His expertise in high performance computing and fluid mechanics, combined with his dedication and ability to teach, have made him the perfect mentor. It is hard to find the right words to express how grateful I am for allowing me to be his first student. His extensive understanding of the physics of turbulence, his constant pursuit for excellence, and the intellectual curiosity with which he explores new aspects of the field have been a true inspiration. All the aforementioned qualities, combined with his humility and work ethics, have made working with him a privilege.

I am also thankful for the opportunity I had to interact with distinguished scholars in the field of turbulence. A special thank goes to Dr. Rubinstein who I had the opportunity of learning from at several conferences. I would also like to thank Drs. Bowersox, Girimaji and North for being part of my committee and for sharing with me their boundless knowledge in the different aspects of this work. I am specially grateful to Dr. Girimaji for teaching me about turbulence inside and outside of the classroom. The same goes to Dr. Bowersox who has helped me with

the different aspects and complexities of hypersonic flows. Dr. Sánchez-González has also been extremely helpful in describing the details and parameters of the laboratory experiments. I would also like to thank Dr. Leeland Carlson for being an inspiration during my undergrad and for motivating me to pursue my PhD.

I am also in debt with the excellent staff of our department, whose help in solving everyday issues has made this possible. I would specially like to thank Ms. Letherman and Ms. Knabe who have constantly gone beyond their duty to help me since the first day I started my PhD. Ms. Veals, Ms. Gilbert, and Ms. Marianno have also been extremely helpful, as have been Mr. Munnerlyn and Mr. Pollard for their support with IT issues. I would also like to express my gratitude to the Scholarships and Financial Aid Department at Texas A&M University for the constant support with grants and scholarships.

My girlfriend Stephanie has made this journey much more cheerful. I cannot thank her enough for supporting and helping me throughout the hardest times of my PhD. My lab mates Aditya, Shriram, Chang-Hsin and Sualeh have also supported and helped me every step of the way. My relationship with Aditya and Shriram is one that extends far beyond the lab. I have learned from them and I take with me a friendship that will last a life time. Also, a big thanks to the innumerable friends who have made this possible: Javier, Rodrigo, Marcos, Jose, Antonio, Koko, Ranu, Fede, Maxi, Alvaro, Matias, Mauricio, Vasco, Juan, Pedro, and Tomas.

Finally, I am most thankful to my family who has supported me unconditionally since I started my Bachelor's. My father devoted his life to make my higher education possible. Through his inspirational achievements he has made me believe that

anything is possible. He always had the right words to motivate me when things did not turn out as I expected. As he would always say, “A farmer will always have to wait for his crops to grow, just be patient and results will come”. My mother, through her unconditional support and boundless love, has always been a constant thrust for my work. She has always believed in me, more than I believe in myself, and has encouraged me to pursue new challenges. Her occasional visits with my sister have always cheered me up and have helped me feel a little closer to home. My brother and best friend, Diego, has been a role model to me for as long as I can remember. He has been an inspiration in the way he lives his life both professionally and personally. I have always relied on him for advice and no matter how busy he was, he has always found the time to help me when I needed it most. My sister, whose joyful optimism and love are unrivaled, has also been a great motivation. And last but not least, a big thanks to my grandparents Fernando and Alejandra who have always been there for me.

TABLE OF CONTENTS

Page

CHAPTER Page

LIST OF FIGURES

FIGURE Page

FIGURE Page

FIGURE Page

LIST OF TABLES

CHAPTER I

INTRODUCTION

High speed flight is a recurring topic in the field of aerospace engineering. In some instances it is unavoidable, like the case of re-entry vehicles. As vehicles in space approach the earths atmosphere, they can be traveling at tens of times the speed of sound. There is also great interest in hypersonic speeds for both space and air travel, given flight times are drastically reduced. One of the major challenges faced by hypersonic vehicles (scram-jets, re-entry) is heat insulation. High speeds typically lead to extreme temperatures that are a real threat to the materials used (Walker *et al.*, 2008; Masaki & Yakura, 1969). Another challenge in air breathing hypersonic vehicles is attaining efficient combustion. A solution to the former may come from exchanges of molecular degrees of freedom, while the latter may be improved by mixing enhancements from small scale turbulence (Buckmaster *et al.*, 2012).

This study aims at providing fundamental understandings that can be used to solve these problems from a fluid dynamics stand point, rather than improving the materials used or injection techniques for enhanced mixing. We propose a new concept to establish turbulence using photo-excitation of the molecules that comprise the fluid. This concept was inspired by the experimental use of lasers to photo-dissociate seeded molecules, whose fragments possess different degrees of thermal non-equilibrium (TNE) which are then used to obtain measurements of temperature, for example. Details on this technique can be seen here in Refs. (47; 46; 88; 89). In this photo-dissociation process molecular fragments can have very large speeds. For

example, NO_2 excited with 355 nm produces fragments with velocities in excess of (Hsu *et al.*, 2009*a*) 1000 m/s. Diatomics such as Cl_2 present velocities of about (Booth *et al.*, 2012) 1700 m/s. If the flow comprises enough seeded molecules, the fragments may create a macroscopic perturbation which can in turn trigger turbulence. This is even more so if the fluid itself is made up of molecules susceptible to the photo-dissociation process just described.

Laser induced concentrated energy sources (LICES) may be a feasible method for improving combustion in air-breathing hypersonic vehicles. Furthermore, there are well known interactions between TNE and turbulent transport (Fuller *et al.*, 2014), so understanding these effects can help improve the efficiency of such grid, or could lead to techniques for reducing translational temperature (Donzis & Maqui, 2016). Nonetheless understanding the complex interaction between grid generated compressible turbulence and TNE is a remarkably ambitious project which must be taken a step a time. Consequently the efforts to understand the complex physics behind LICES is divided into three steps, each with its own milestone.

The first is understanding the physics behind grid (LICES) generated turbulence in incompressible flows. This is a simplified version of LICES where there are no thermodynamic effects and we call LIKES: localized intense kinetic energy sources. There are vast amounts of literature of incompressible grid turbulence, so this first step can help us validate the concept while understanding the main mechanisms for generating turbulence based on concentrated energy sources such as LICES or LIKES. The incompressible simplification also makes the problem computationally more tractable. The second step is to add compressibility effects, and hence the

additional complexity of interacting fluid and thermodynamic variables. This step is focused on the feasibility of improving hypersonic combustion by LICES generated turbulence. The last and final step is to add the effect of thermal non-equilibrium to compressible turbulence. This could potentially lead to techniques for reducing translational temperature in hypersonic vehicles. A background and literature review with the main accomplishments in these fields will be given next.

I.A. Background and literature review: Grid generated turbulence

High-Reynolds number turbulent flows are observed in a wide variety of engineered and natural systems. Due to the importance of our ability to predict and control these flows, substantial efforts have been made over the decades to understand their behavior and fundamental principles. As a result of the well-known complexities of high-Reynolds number flows, most of our understanding has benefited from data from physical laboratory experiments and computational simulations, each with its own limitations and strengths. The accuracy of measurements in physical laboratory experiments, and computational power in numerical simulations are two of the main bottlenecks towards achieving higher realistic Reynolds numbers.

One of the first approaches to study turbulence dates back to as early as 1934 and came in the form of grid turbulence in a physical laboratory experiment. The pioneering work of Simmons & Salter (92) utilized what is now known as a "passive" grid. The name comes from the fact that a solid, non-moving grid is placed in a uniform flow creating perturbations which grow in space to eventually become turbulence further downstream. Following Simmons & Salter came the very influential paper

by Taylor (99). Passive grids have proven to be very simple and effective in creating homogeneous turbulence (Gence, 1983), thus widely used (11; 31; 50). Nonetheless, they possess certain limitations, which among others include the achievable Reynolds number and the persistent degree of anisotropy observed as turbulence decays. Since most related theoretical work on turbulence assumes the flow to be in a state of isotropy, even if only local, achieving this condition is fundamental for comparing theoretical and experimental results.

A measure of the anisotropy of the flow downstream of the grid is the relation between the streamwise and transverse root-mean-square velocity components u'/v', which is unity for a perfectly isotropic state. Grant & Nisbet (35) among others have reported the issue of anisotropy in the flow behind a square mesh grid. Consistent with other experimentalist, they found that the streamwise velocity fluctuations are higher than transverse velocity fluctuations. Comte-Bellot & Corrsin (11) attempted to overcome this issue by passing the flow through an axisymmetric contraction, originally suggested by Prandtl (80). With a slight contraction of 1.27 to 1, the flow remains isotropic with equal lateral and axial mean square components. However, similar experiments with contractions (Uberoi & Mahinder, 1957) reveal that the anisotropy returns. It was also observed that the turbulence resulting from passive grids is fairly insensitive to the geometry and characteristics of the grid. Even though there is an effect on the rate of decay of turbulence, the ratio of u'/v' is independent of geometry with no clear proclivity towards equipartition (Uberoi & Wallis, 1967).

The limitations of passive grids led to the introduction of "active" grids which, as the name suggests, have movable parts or inject a secondary flow in the form of a

jet with the main purpose of introducing momentum to the flow. Extensive research has been published with this type of grids, with a focus on trying to achieve isotropic turbulence at high Reynolds numbers. One of the first successful approaches to active jet grids was that of Mathieu & Alcaraz (69) as described by Gad-el Hak & Corrsin (38). They significantly increased the turbulence intensity compared to passive grids but there were some limitations regarding the degree of isotropy in the flow. Gad-el Hak & Corrsin (38) improved the homogeneity of the flow by introducing controllable nozzles while retaining high turbulent intensity. Since then, a number of different active grids have been used including oscillating grids (14), vibrating grids (91), and rotating grids (74). Implementing an active grid devised by Hideharu (40), Mydlarski & Warhaft (1996) span a range of Taylor Reynolds numbers (R_λ) from 50 to nearly 500. Some of the drawbacks with this type of grid are the increased complexity and the difficulty in changing the grid to study possible geometrical effect. However, the increased turbulence intensity from active grids show that it is possible to generate high Reynolds number turbulence in reasonable-sized facilities.

In all the efforts mentioned above, an issue of practical relevance is the determination of the distance from the grid necessary to obtain fully developed turbulence. Close to the grid, clearly the flow will not be turbulent, statistically isotropic or even homogeneous. The distance from the grid at which the flow is considered fully turbulent is often taken as the point where the decay of turbulent energy follows a power law (Mohsen, 1990; Sinhuber *et al.*, 2015), though other quantities have also been used. Two quantities typically observed are the 4/5-th law in the inertial range and the skewness of the velocity gradient, which have been documented in

Refs. (98; 96).Nonetheless, there seems to be no systematic study of the effect of different grid parameters on this location.

Our objective here is to study the generation of turbulence from localized intense kinetic energy sources (LIKES). This configuration resembles the active jet grids described above, or as we will see later, it also resembles grid turbulence passed through a contraction. The mechanism is also present in the concept of generating turbulence with LICES. Using this method to generate turbulence can provide several advantages over the known traditional active and passive grids. The alignment of the lasers can be easily modified to study the effect of grid geometry. Changing the seeded molecules or the intensity of the lasers can also modify the strength of the perturbations. This provides a wide range of easily modified parameters that can be tuned according to user based needs. Furthermore, since the lasers can be turned on and off, these can be dynamically activated to enhance turbulence and may be useful for industrial applications. As turbulence small scales are required for efficient mixing and combustion (Dimotakis, 2005), a potential application of this concept is to improve efficiency of combustion in hypersonic air-breathing vehicles such as scramjets, where streamwise vortices can increase macro and micro mixing for improved hypersonic combustion (Buckmaster *et al.*, 2012). This non-invasive grid may increase mixing without increasing the overall combustor losses.

Even though there are numerous advantages and applications for this new concept to generate turbulence, several questions arise with the practical implementation of LIKES. The first and most important is whether realistic turbulence can be generated. Furthermore, if it is possible, can it be generated within the confinements of

a laboratory wind tunnel? In order to answer these questions and study the physics of this type of flow, direct numerical simulations (DNS) are used to analyze the evolution of flows with LIKES. Direct numerical simulations can also provide more insight on the physical processes that lead to the creation or shortcomings of grid generated turbulence. In physical experiments it is difficult to obtain measurements near the grid. This, however, is not a problem with DNS which in general can provide information as the flow evolves in both time and space. Although there is a vast literature on both physical experiments of grid turbulence and DNS of isotropic turbulence, there is virtually no literature on DNS of grid generated turbulence. The numerical experiments presented here will allow us to study the feasibility of generating and controlling turbulence from intense localized sources of kinetic energy as the one obtained from photo-excitation of molecules while at the same time further understanding general physical mechanisms behind passive and active grids to generate turbulence.

A detailed study of incompressible flows starting from concentrated kinetic energy sources will be given in the next following sections.

I.B. Background and literature review: Hypersonic combustion and turbulence

Combustion of hypersonic air-breathing vehicles such as scramjets has been a subject of study for several decades. Two of the earliest works to propose combustion at supersonic speeds were that of Ferri (1960) and Dugger (1961). In a scramjet, air at the inlet is compressed and decelerated from hypersonic to super-

sonic speeds, where the fuel residence at the combustor is of approximately 1ms (Ladeinde *et al.*, 2009). Of course there are numerous difficulties associated with achieving controlled combustion at such conditions. As summarized in the review article by (Ferri, 1973), these issues include but are not limited to: performance of supersonic combustion flame (Curran *et al.*, 1996), complex interactions between fluid dynamics and combustion, extremely short residence time in the combustor (Kumar *et al.*, 1989), and a rapid decay in mixing efficiency of supersonic flows compared to subsonic (37; 3; 73; 32; 58).

Of particular interest here is the issue of mixing efficiency. A large number of methods have been proposed for enhanced mixing in scramjet engines, most of which can be found in the historical survey by (Seiner *et al.*, 2001). These include both passive and active mechanisms for controlled forced mixing of fuel and oxidizer. Some of the most known passive methods include ramp fuel injectors, tabs, shock/shear layer interaction and cavities. Ramp fuel injectors induce a pair of counter-rotating streamwise vortices (Rogers *et al.*, 1998) coupled with shock and expansion waves to increase mixing. Both compression and expansion style ramps have been tested in the literature. Stouffer *et al.* (1993) have shown that although compression ramps provide larger vorticity and fuel/air mixing, expansion ramps yield higher combustion efficiency from mixing at the small scales. The strong axial vorticity generated by compression ramps tends to suppress the growth of transverse scales. Similar to ramp style fuel injectors, tabs also introduce counter-rotation streamwise vorticity and lead to separated flow. Grosch *et al.* (1997) have shown a large increase in mixing with low performance losses when using numerous tabs. From linear theory, Ribner (1954)

demonstrated that turbulence is amplified upon interaction with a plane shock wave. A number of studies in this canonical configuration supported this conclusion (Lee *et al.*, 1997; Mahesh *et al.*, 1997; Donzis, 2012). Even in more realistic settings, such as a scramjet combustor, mixing was found to be greatly increased upon interaction with oblique shocks (Menon, 1989).

Passive methods are practical solutions for increased mixing but they are typically constrained to specific flight conditions. On the other hand, the harsh environment of scramjet combustors makes active methods more challenging to implement. Nonetheless, several authors have proposed these methods as potential candidates for increased mixing in scramjets. Some of the active mixing methods include vibrating wires, piezoelectric actuators, pulsed jets, and acoustic excitation among others. Vandsburger & Ding (1993) have shown that mixing can be doubled when placing a wire across jet shear layer. Although difficult in practice, newer methods with wires fixed at the nozzle exit, with the other end free to oscillate, suggest accelerated energy transfer to small scales through vortex shedding (Seiner *et al.*, 2001). A similar concept developed by Wiltse & Glezer (1998) uses piezoelectric actuated flaps at the trailing edge of a nozzle. Driven at the resonance frequency, their measurements show a notable increase in small scale turbulence.

In summary, small scale turbulence is greatly desired to achieve efficient mixing and combustion (Dimotakis, 2005). Therefore, it is not surprising that all the mentioned methods, both passive and active, attempt to accelerate the creation of small scale turbulence structures. Some of the passive methods provide efficient mixing without significant combustor losses, however these are typically fine tuned

for a specific Mach number range. Active methods have the potential of increasing small scale turbulence at a wide range of conditions, yet the feasibility of practically applying these methods is questionable.

Implementing LICES might be a solution to the limitations of both active and passive methods. Although active, LICES would require no movable parts within the combustor. This new method can provide several advantages over the passive and active methods available. The alignment of laser can be easily modified to provide variable grid geometry for adaptable conditions. The lasers can also be pulsed to generate acoustics at certain frequencies. As demonstrated by Bogdanoff (1994), acoustic excitation can deliver shear layer instability waves for enhanced mixing efficiency. This non-invasive grid may be actively controlled for changing conditions without increasing combustor losses. While there are numerous advantages with this new concept, several questions arise about the feasibility of such method. The most important question is whether this type of grid can generate isotropic turbulence. Additionally, one needs to address whether it can be tuned to trigger turbulence at short distances such that it may be used for improving the efficiency of scramjet combustors. Answering these questions for conventional active and passive grids has been a subject of study for nearly a century, as described in the previous section. There is vast literature on the main mechanisms leading to turbulence using active grids for incompressible flows (De Silva & Fernando, 1994; Shy *et al.*, 1997). However, there is a very little work on grid turbulence where compressibility effects become significant ($M > 0.3$), and even less in highly compressible hypersonic flows.

The early work of Honkan & Andreopoulos (1992) and Honkan *et al.* (1994)

used shock tubes to study the interaction between upstream turbulence and normal shocks. Briassulis *et al.* (2001) studied the main mechanisms leading to the creation of grid generated turbulence in weakly compressible flows. However, reaching the transonic-supersonic region imposes several difficulties. As described by Zwart *et al.* (1997), the flow behavior becomes extremely sensitive to geometry an supply pressure in the range $0.7 < M < 1$. Unsteady shocks develop in the test section that affect the results and the measuring techniques. It is clear that generating grid turbulence at hypersonic speeds is not a trivial problem, and hence the lack of literature. In the current work we propose studying this problem using direct numerical simulations (DNS) which with the tremendous detail they generate, allow us to obtain a large number of quantities that are extremely difficult or expensive to obtain experimentally.

With DNS we may also study more complex physics behind a grid based on LICES. The photo-excitation/dissociation of molecules introduces additional internal degrees of freedom, such as vibrational and rotational, that lead to thermal non-equilibrium (TNE). There are well known interactions between TNE and turbulent transport (Fuller *et al.*, 2014; Donzis & Maqui, 2016), so understanding the effects on LICES can further help improve the efficiency of such grid. The numerical study presented here will allow us to determine the feasibility of generating turbulence from localized sources of energy while further understanding grid generated turbulence in hypersonic flows.

I.C. Background and literature review: Thermal non-equilibrium and turbulence interactions

In many flows, the molecular structure and state of the constituent fluid plays a significant role on the macroscopic behavior of these flows. In such situations, some molecular modes of energy, especially those associated with longer time scales, may not be in thermal equilibrium and the flow is thus said to be in thermal non-equilibrium (TNE). This situation is encountered in low-temperature glow plasmas, flows behind shock waves and supersonic expansions and can be recreated in laboratories with lasers to excite specific molecular modes (Rich & Treanor, 1970; Rich *et al.*, 1996). TNE has also a significant effect on reaction rates in reacting flows and heat transfer characteristics in hypersonic vehicles. Although the asymptotic behavior of simple steady laminar flows in TNE has been studied before (**?**), very few studies have focused on the interaction of turbulent fluctuations with TNE. These numerical (Liao *et al.*, 2010) and experimental (Fuller *et al.*, 2014) studies, nonetheless, shown strong coupling between them. However, no general or systematic study is available to determine, for example, how the distribution of energy in different modes is affected by turbulence and how this depends on turbulence statistics as well as molecular properties. This is the thrust for the present study. Our objective here is to determine general statistical features of energy modes, in particular molecular vibration of diatomic molecules, when the flow is turbulent and in TNE. We show that, due to the non-linear nature of partially excited vibrational modes, turbulent fluctuations create statistically steady states that, unlike laminar flows, do not approach thermal equilibrium at long times. This has implications on the distri-

bution of energy in different modes, namely, vibrational, translational and rotational molecular modes.

If turbulence can be used to store energy in the vibrational or rotational mode, rather than the translational mode, this has a big potential for heat reducing techniques in hypersonic vehicles. For example, for a re-entry or a hypersonic vehicle we may design a method such that a laser sheet foresees the molecules in the flow before they come in contact with the vehicle. This could increase energy in vibration and decrease the translational temperature. Furthermore, if a turbulent flow could potentially store more vibrational energy than a laminar flow, we can simultaneously use the LICES to create turbulence. Of course, this could have negative implications on the drag of the vehicle, but the wide range of application of LICES are worth noting.

I.D. Objectives of the present work

In this work we have propose to:

1. Implement localized intense kinetic energy sources (LIKES) in a massively parallel incompressible Navier-Stokes code.

2. Generate a large database of incompressible flows based on LIKES and characterize the evolution and transition to turbulence.

3. Understand the main mechanisms leading to turbulence based on LIKES.

4. Implement laser induced concentrated energy sources (LICES) in a massively parallel compressible Navier-Stokes code.

5. Generate a large database of compressible flows based on LICES and characterize the evolution and transition to turbulence.

6. Understand the main mechanisms leading to turbulence based on LICES, including the effect of thermodynamic variables and dilatational motions.

7. Understand the effect of thermal non-equilibrium in steady state isotropic compressible turbulence.

This work is done in collaboration with the National Aerothermochemistry group at Texas A&M University led by Dr. Bowersox, and the chemistry departments at Texas A&M University and Texas Tech University led by Dr. North and Dr. Hase respectively. The close interaction between the different collaborators has also been a primary objective of this work. We have relied on the experimental evidence to model the hydrodynamics of the photo-dissociation process as accurately as possible. In turn, our simulations provide the parameters for designing the laboratory experiments of the current work presented.

CHAPTER II

DIRECT NUMERICAL SIMULATIONS

In this chapter we describe the numerical schemes used and numerical implementation of the previously described problem. Direct numerical simulations (DNS) of both incompressible and compressible flows are solved using two different numerical schemes which will be described below. For incompressible flows, the nature of the incompressible Navier-Stokes equations and the periodic boundary conditions make pseudo-spectral methods the best approach to solve this problem. On the other hand, the compressible Navier-Stokes, which use non-periodic boundary conditions, are solved using compact-schemes. In this chapter we present the governing equations along with the numerical scheme and initial conditions/forcing used to model the photo-dissociation of molecules. The governing equations for thermal non-equilibrium, which are coupled with the compressible Navier-Stokes equations, are also shown.

In this chapter we also present a novel numerical method for implementing the Helmholtz decomposition in non-periodic domains. This is done through a modified windowing technique which will be presented in vast detail.

Although units are excluded for simplicity of the notation, all non-normalized quantities in this chapter, as well as the following chapters, are in the International System of Units (SI).

II.A. Incompressible numerical scheme and initial conditions

In order to study the physics of the previously described problem, we performed direct numerical simulations (DNS) in a periodic domain of size $(2\pi)^3$ using a pseudo-spectral code. This code provides unique resolution capabilities in terms of small-scale resolution that allow studying the problem at an affordable computational cost. The flows is assumed to be incompressible which is justified given the low speeds considered here and is consistent with the literature for turbulence generated with passive and active grids. The latter, as shown below, presents important similarities with our flow. During the photo-excitation process described above, however, this may not be entirely satisfactory. Our interest, nonetheless, is in the fundamental hydrodynamic processes that occurs shortly after photo-excitation, when the thermodynamic variables have reached equilibrium and the flow can be considered incompressible. Thus, our results for this particular way of generating intense localized kinetic energy, are valid shortly after the photo-excitation process which is assumed to be fast compared to flow time scales.

Thus our simulations are based on the incompressible Navier-Stokes equations given by

$$\begin{aligned} \frac{\partial u_i}{\partial x_i} &= 0 \\ \frac{\partial u_i}{\partial t} + u_j \frac{\partial u_i}{\partial x_j} &= -\frac{1}{\rho}\frac{\partial p}{\partial x_i} + \nu \frac{\partial^2 u_i}{\partial x_j^2} \end{aligned} \tag{2.1}$$

which are solved according to the Rogallo (1981) formulation: non-linear terms are computed in physical space and aliasing errors are controlled by a combination of truncation and phase shifting. Time advancement is performed with an explicit

second-order Runge-Kutta scheme with a time step size set by a CFL condition. The resulting time resolution is between one and two orders of magnitude smaller than the average Kolmogorov time scale. Viscous terms are treated exactly by the use of an integrating factor in wave-number space.

There are several numerical difficulties associated with implementing LIKES as initial conditions. The primary issue arises from having contrasting concentrated regions of very large velocities and a stagnant background. This creates large gradients that are difficult or very expensive to treat numerically. This is discussed next.

II.A.1. Implementation of LIKES

To reproduce the intense kinetic energy sources generated by e.g. photo-dissociation or jet grids, velocity perturbations must be introduced in concentrated regions or so called LIKES, as shown in Fig. II.1. These perturbations are assumed to possess a Gaussian distribution in the plane of the perturbation, which can be justified from experimental observations of the photo-dissociation process (North & Hall, 1997; North *et al.*, 1997). The fragment departure direction, which defines the perturbation velocity vector, has for the most part an angular relationship with the polarization of the photolysis light (Houston, 1987; Dixon, 1986). Therefore, it is expected that a preferential direction of photo-dissociation will favor one component of velocity dependent on the polarization of the laser. This is also the case for jet grids as well as passive grids followed by a contraction, as will be seen in Sec. III. If perturbations are implemented on a single component of the velocity field, namely the z-component, then $\partial u_i/\partial x_i \neq 0$ and continuity is not satisfied, thus a second component of velocity

is needed to satisfy continuity. These two components of the velocity field can either be introduced in physical or Fourier space. However, truncation of the highest wave numbers, for aliasing control, when transforming from physical to Fourier space alters the velocity field, smoothing the perturbations. Since the Fourier transformation of a Gaussian is a Gaussian itself, this issue is resolved by introducing the perturbations in Fourier space where continuity can also be satisfied trivially. As represented in Fig. II.1, the LIKES are implemented along x cutting through the $y-z$ plane and perturbations are introduced in w. Continuity is then satisfied by introducing perturbations in u. In order to generate a random spatial distribution of perturbations consistent with experiments, the velocity is constructed as a sum of Gaussians along x with random amplitude and phases. The initial velocity field in three dimensions becomes:

$$\begin{aligned} \hat{w} &= \sum_{l_y,l_z=0}^{n_y,n_z} \sum_{\beta=1}^{\beta_0} \pm w_0 \times \\ &\exp\left[-c_x\pi^2 k_x^2 - \iota 2\pi k_{sx}(\beta)k_x - c_y\pi^2 k_y^2 - \frac{\iota l_y k_y 2\pi}{n_y} - c_z\pi^2 k_z^2 - \frac{\iota l_z k_z 2\pi}{n_z}\right] \end{aligned} \tag{2.2}$$

and the u component of velocity can then be trivially obtained from Eq. 2.1a in Fourier space:

$$\hat{u}k_x + \hat{w}k_z = 0 \tag{2.3}$$

where n_y, n_z are the number of LIKES along y and z respectively. The total number of LIKES, $n_y \times n_z$, is N_l. β_0 is the number of perturbations along x ($\pm$ is to alter between positive and negative perturbations for each β). To distribute the

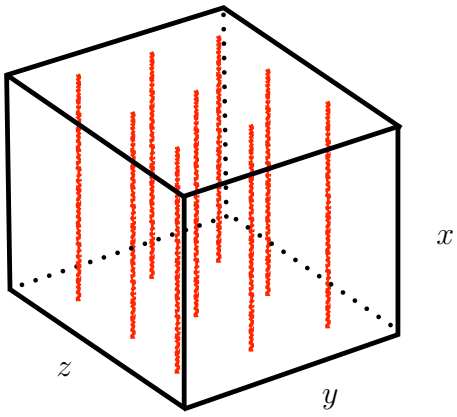

Figure II.1. Representation of nine LIKES as initial conditions ($N_l = 9$).

perturbations along x, $k_{sx}(\beta)$ takes a random number between 0 and 1 for each β. $k_{x,y,z}$ are the wave numbers and $c_{x,y,z}$ determine the width of the Gaussian in x, y, and z respectively. For all simulations, $c_y = c_z$ which will be denoted as c_{yz} ($c_{yz}^{1/2}$ is proportional to the radius of the LIKES in the y-z plane) . Increasing the value of $c_{x,y,z}$ will lead to wider Gaussians and thus smoother gradients. When transformed to physical space, a single perturbation ($\beta = 1$, $l_{y,z} = 0$) follows the distribution:

$$w_p = \kappa_0 \exp\left(-\frac{x^2}{4\pi^2 c_x} - \frac{y^2+z^2}{4\pi^2 c_{yz}}\right) \tag{2.4}$$

where $\kappa_0 = w_0/(\pi^3 c_x c_{yz}^2)^{1/2}$ is the amplitude of the perturbation. As mentioned previously, a series of perturbations are randomly distributed along the LIKES in the x-axis. For the present simulations, we use $\beta_0 \approx 100$ though the results presented here are unaffected by this specific value.

For an a-priori estimate of the resulting velocity field accounting for the random distribution of negative and positive perturbations along the LIKES, we need to

approximate the number of perturbations that will overlap or cancel each other. The degree of cancellation can be accounted for by assuming an effective number of active perturbations, β_e, instead of the total β, which we find in our cases to be close to 1/2. From the full width at half maximum, it is also possible to estimate the average number of perturbation that would fill the length of the domain without overlapping with other perturbations. Using standard probability concepts on binomial trials, we find the probability of two overlapping perturbations to be $p_2 = \beta_e!/(2!(\beta_e - 2)!)\,(1/20)^2\,(1-1/20)^{\beta_e-2}$, while that of non-overlying perturbations is simply $p_1 = 1 - p_2$. Integrating the velocity squared multiplied by these probabilities to estimate the rms, the velocity distribution becomes:

$$\begin{aligned} w &\approx w_p \left(\left(\frac{N_l \beta_e}{(2\pi)^3} \int_{-\pi}^{\pi}\int_{-\pi}^{\pi}\int_{-\pi}^{\pi} (p_1 + 4p_2) w_p^2 dxdydz \right)^{1/2} \right)^{-1} w_0 \\ &\approx \kappa \exp\left(-\frac{x^2}{4\pi^2 c_x} - \frac{y^2+z^2}{4\pi^2 c_{yz}} \right) \end{aligned} \tag{2.5}$$

where $\kappa = \alpha w_0/(N_l c_x^{1/2} c_{yz}(p_1+4p_2)\beta_e)^{1/2}$ is the estimated amplitude of the total sum of perturbations and $\alpha = (2^6/\pi^3)^{1/4}$. For simplification the error function involving c_x and c_{yz} which appears after the integration has been dropped, as they are very close to 1 when evaluated for all the cases. In summary, the initial velocity is a function of several parameters, namely, w_0, N_l, β_e, and the width of the Gaussian c_x and c_{yz}. However, in practice they cannot be chosen arbitrarily. For example, how much energy we can introduce in the form of LIKES will depend on the maximum gradient that can be resolved by the numerical scheme. The next section is dedicated to determining this criterion.

II.A.2. Convergence study

Introducing LIKES can be very challenging numerically. The nature of the random localized perturbations creates very strong gradients that may be hard to capture. To assess whether the numerical scheme can capture the imposed perturbations one needs to perform a grid convergence study. For this, one first needs to identify the parameters controlling the initial conditions and then relate these with the grid spacing.

The four parameters that determine the initial velocity distribution are w_0, N_l, c_x and c_{yz} (β is constant for all cases, so it is not considered). All four control the amplitude of the velocity perturbation while only the third and fourth determine the width of influence. Increasing w_0 or decreasing N_l will makes the amplitude of the perturbation larger, while decreasing c_x or c_{yz} makes the distribution narrower. Both changes will lead to stronger gradients in the initial condition. As shown above, however, all the parameters can be accounted for in κ, which determines the magnitude of w given w_0, N_l, and $c_{x,yz}$.

To determine the resolution needed to capture the maximum gradient, we consider the worst case scenario. To do so, we need to understand where and in which direction the maximum gradient occurs. Even though the narrowest Gaussians are along x ($c_x < c_{yz}$), the accumulation of perturbations provides a significant amount of cancellation between them that smoothens the gradients in x and yields an effective $c_{yz} < c_x$. With this in mind, and since from continuity $\hat{u} = k_z/k_x\hat{w}$, the maximum gradient is found in the first component of velocity. However, we note that the analysis below would apply equally well if the maximum gradient is in an-

other direction by simply considering that particular gradient and direction in the formulae that follow.

To guarantee adequate resolution for the sharpest gradient we must then have:

$$\left.\frac{\partial u}{\partial \alpha}\right|_{max} \sim \frac{\kappa}{\gamma \Delta \alpha} \tag{2.6}$$

where κ is the amplitude of the perturbation, α is either y or z (due to symmetry in the y-z plane), and γ is the number of grid points required to properly resolve the gradient. Substituting $\Delta\alpha = 2\pi/N$ (N is the number of grid points along y or z) and the highest resolvable wavenumber (Rogallo, 1981) $k_{\max} = \sqrt{2}N/3$ (on a N^3 grid) into Eq. (2.6), and using Eq. (2.4) on the left-hand side, we rewrite Eq. (2.6) as

$$G \equiv \frac{3k_{\max}\sqrt{c_{yz}}}{2} \tag{2.7}$$

where γ has been absorbed by the new parameter G, which quantifies the resolution of the sharpest gradients generated by the Gaussians. The higher G, the more points are used to resolve the sharpest gradients which are thus better resolved. Well resolved simulations are then expected to performed on a grid resolution such that G greater than some $G_{\min}$ still to be determined. This convergence criterion is based on kinematic considerations and, while necessary, is found to be insufficient to guarantee convergence of the simulation.

Numerical experiments reveal that a second, dynamical, condition is required for convergence. Velocity fluctuations at scales smaller than the Kolmogorov scale are highly damped by viscous effects and are commonly assumed to have a negligible contribution to the dynamics of flow. In non-dimensional form, one expects the

Reynolds number based on these scales to be small. Similarly, the numerical grid must be fine enough such that its Reynolds number is also small to account for fluctuations in the order of the length scale $\eta \sim 1/k_{\max}$ (Yakhot & Sreenivasan, 2005). If again as a worst case scenario we take the maximum velocity in the flow, $w_{\max}$, then the Reynolds number:

$$R_k = \frac{w_{\max}\frac{1}{k_{\max}}}{\nu} = \frac{\kappa}{k_{\max}\nu} \tag{2.8}$$

must be smaller than some threshold $R_k^{\max}$ presumed to be order 1. Suitable values for $R_k^{\max}$ and $G_{\min}$ must be found through numerical experiments. To do so, the evolution of the space averaged dissipation rate $\langle\epsilon\rangle$ is used, as it is known to be sensitive to small scale resolution. Several authors have used the peak of the dissipation in decaying flows, or the maximum mean enstrophy to determine the onset of turbulence. Starting with a typical energy spectrum, Yamamoto & Hosokawa (1988) have shown that by the peak of the mean dissipation, turbulence is fully developed based on the **?** (K41) premise and the skewness of the velocity gradient, among other quantities. Similar observations have been made by **??**, making $\langle\epsilon\rangle$ a reasonable choice for both convergence and to determine the onset of fully developed turbulence. The latter will be throughly studied. In Fig. II.2 we show typical evolutions of the average dissipation rate for different resolutions. We can see that the value of the maximum dissipation changes with resolution and so does the location of the peak with respect to time. These two parameters, $\langle\epsilon\rangle^*$ and τ^* thus, which will be studied extensively below, appear as natural choice for determining when the simulation becomes grid independent. The relative error is computed using the highest resolution available

(N_{max}):

$$\varepsilon_{\langle\epsilon\rangle^*} = \frac{\left|\langle\epsilon\rangle^*_N - \langle\epsilon\rangle^*_{N_{\max}}\right|}{\langle\epsilon\rangle^*_{N_{\max}}} \tag{2.9}$$

The error for these two quantities can be seen in Fig. II.3 as a function of G, where an error below 2% is considered converged. From the plots it becomes apparent that a $G_{\min}$ in the order of 10 is required, but this does not guarantee convergence as mentioned above. The two convergence criteria are then combined into Fig. II.4 to obtain the region of converged simulations.

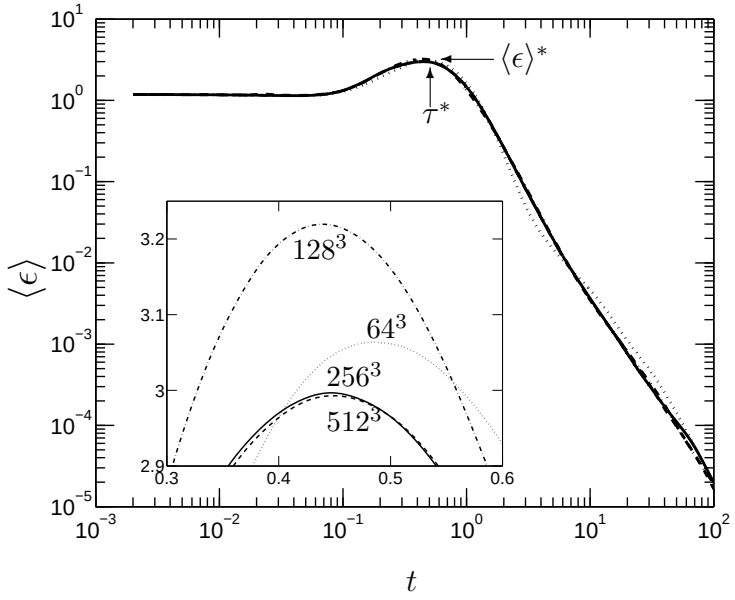

Figure II.2. Averaged dissipation rate for resolutions 64^3 to 512^3, with fixed initial conditions. Inset: peak of dissipation in linear scales.

By examining all the database we can establish that well resolved simulations require $G_{\min}$ larger than 5 and $R_k^{\max}$ smaller than 10. The region on the bottom right of Fig. II.4 contains all the converged simulations. Note that a few cases lie outside of the convergence region which shows our criterion is slightly conservative, thus

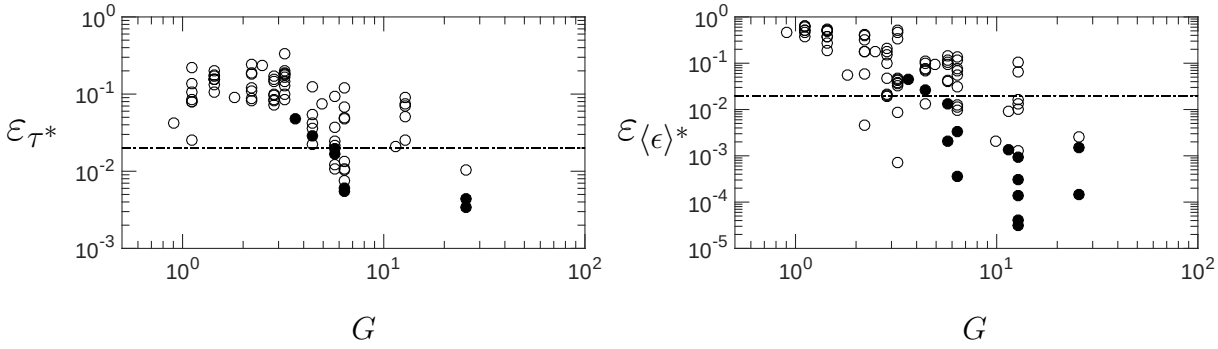

Figure II.3. Relative error for τ^* and $\langle\epsilon\rangle^*$ as a function of G for different initial conditions with varying $k_{\max}$, w_0, N_l, and c_{yz}. Closed symbols satisfy the $R_k^{\max}$ criterion while open symbols do not. Horizontal dash-dot line represents 2% error.

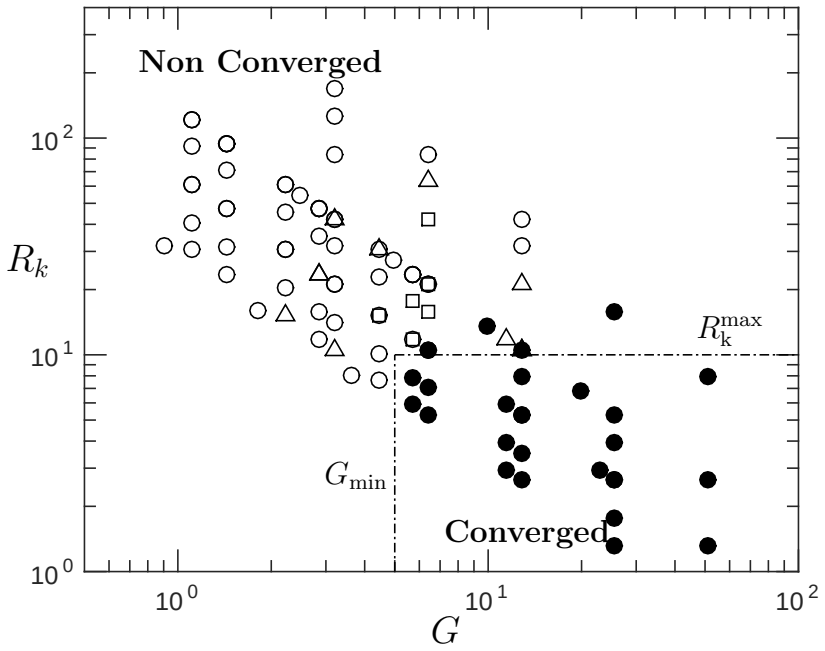

Figure II.4. Convergence of mean dissipation. Squares have satisfied the minimum error for τ^*, while triangles have satisfied $\langle\epsilon\rangle^*$. Closed circles have satisfied both τ^* and $\langle\epsilon\rangle^*$ criterion's for convergence, while open circles have not satisfied either. Vertical and horizontal dash-dot lines correspond to $G_{\min}$ and $R_k^{\max}$ respectively.

assuring convergence for all our simulations. In other words, all data here present an error of less than 2%. Table II.1 contains all the simulations that satisfy the two convergence criterion. The database has a wide range of viscosities, N_l, shape of Gaussian $c_{x,y,z}$, and grid resolutions up to 1024^3.

Case	$N_l^{1/2}$	κ	ν (10^{-3})	c_x (10^{-3})	c_{yz} (10^{-3})	N	G	R_k	R_I	R_λ^*	R_λ^{2*}
1	2	6.3	3	0.4	5.0	512	25.6	5.2	286	42	31
2	3	8.4	4	0.4	5.0	512	25.6	5.2	430	48	35
3	3	10.8	4	0.4	3.0	512	19.8	6.7	333	46	32
4	4	3.1	3	0.4	5.0	256-1024	12.8-25.8	1.3-5.2	286	44	33
5	4	7.0	3	0.4	1.0	512-1024	11.5-22.9	2.6-5.8	128	32	24
6	4	9.1	3	0.4	0.6	512	8.9	7.4	99	28	21
7	4	11.1	7	0.4	0.4	512	7.2	3.9	35	17	13
8	4	3.1	2	0.4	5.0	256-512	12.8-25.6	3.9-9.9	430	54	38
9	4	3.1	6	0.4	5.0	128-512	6.4-25.6	1.3-5.3	143	40	40
10	4	7.0	6	0.4	1.0	256-512	5.7-11.5	2.9-5.9	64	22	17
11	4	9.1	6	0.4	0.6	512	8.9	3.8	50	20	15
12	4	6.3	3	0.4	5.0	512-1024	25.6-51.2	2.6-5.3	573	61	40
13	4	14.0	3	0.4	1.0	1024	22.9	5.9	256	45	32
14	4	6.3	6	0.4	5.0	256-512	12.8-25.6	2.6-5.3	286	44	33
15	4	14.0	6	0.4	1.0	512	11.45	5.9	128	32	24
16	4	18.2	6	0.4	0.6	512	8.9	7.6	99	28	21
17	4	18.8	3	0.4	5.0	1024	51.2	7.9	1718	95	60
18	6	2.1	3	0.4	5.0	128-512	6.5-25.6	1.8-7.0	286	50	37
19	6	4.7	3	0.4	1.0	256-512	5.7-11.5	3.9-7.9	128	40	29
20	6	6.0	3	0.4	0.6	512	8.9	5.1	99	38	27

Table II.1. Table for converged simulations with number of lines N_l, initial perturbation κ, fluid viscosity ν, width of gaussian $c_{x,y,z}$, number of grid points along one direction N, convergece criterions G and R_k, initial conditions Reynolds number R_I, and Taylor Reynolds number evaluated at τ^* and $2\tau^*$.

II.B. Compressible numerical scheme and forcing

The DNS code solves the full compressible Navier-Stokes equations using compact finite differences of sixth-order (Lele, 1992). The compressible Navier-Stokes equations can be written as:

$$\frac{\partial \rho}{\partial t} + \frac{\partial}{\partial x_i}\left(\rho u_i\right) = 0 \tag{2.10}$$

$$\frac{\partial}{\partial t}\left(\rho u_j\right) + \frac{\partial}{\partial x_i}\left(\rho u_j u_i\right) = -\frac{\partial}{\partial x_i}\left[p\delta_{ij} - \mu\left(\frac{\partial u_i}{\partial x_j} + \frac{\partial u_j}{\partial x_i} - \frac{2}{3}\delta_{ij}\frac{\partial u_k}{\partial x_k}\right)\right] + \rho f_u, \tag{2.11}$$

$$\frac{\partial(\rho e)}{\partial t} + \frac{\partial}{\partial x_i}\left(\rho e u_i\right) = \frac{\partial}{\partial x_i}\left[-p\delta_{ij}u_j + k\frac{\partial T}{\partial x_i}\right] + \sigma_{ij}S_{ij} + \rho f_e \tag{2.12}$$

where, ρ is density, u_i is the i^{th} component of velocity, p is pressure, e is internal energy per unit mass, T is temperature, k is thermal conductivity, and f is an additional forcing term implemented through velocity or internal energy f_u and f_e respectively. $S_{ij} = 1/2(\partial u_i/\partial u_j + \partial u_j/\partial x_i)$ is the strain rate tensor, and the σ_{ij} is the viscous stress tensor given by:

$$\sigma_{ij} = \mu\left(\frac{\partial u_i}{\partial x_j} + \frac{\partial u_j}{\partial x_i} - \frac{2}{3}\delta_{ij}\frac{\partial u_k}{\partial x_k}\right) \tag{2.13}$$

where the viscosity μ has a power law dependence based on temperature following Sutherland's Law, and the internal energy is related to temperature through the perfect gas law. The non-linear terms are computed using a skew-symmetric formulation (Blaisdell *et al.*, 1996; Ducros *et al.*, 2000) , and time advancement is perform with an explicit third-order low storage Runge-Kutta scheme (Williamson, 1980). The time step size is controlled with a Courant Friedrichs Lewy (CFL) condition.

Further details on the numerical as well as computational aspects of the code can be found in Jagannathan & Donzis (2012); Donzis & Jagannathan (2013); Jagannathan & Donzis (2015).

The additional forcing term f is used to introduce the LICES. These are introduced at $t = 0$ as initial conditions and then at regular time intervals specified through a forcing frequency H_f. This parameter is introduced as an additional control parameter for a LICES grid as lasers can be turned on and off in actual experiments. The nature of the strong perturbations introduced by the LICES imposes several numerical difficulties. The primary issue arises from having contrasting regions of concentrated large velocities on a stagnant background. This creates large gradients that are difficult or very expensive to treat numerically. The following section will describe how the LICES are numerically implemented to provide converged statistics.

II.B.1. Implementation of LICES

From experimental observations of the photo-dissociation process (North & Hall, 1997; North *et al.*, 1997), the area of influence of velocity or temperature perturbations may be approximately described by:

$$\alpha = \alpha_m - \alpha_m/(1 + \exp[g\,(b - \sqrt{x^2})] \tag{2.14}$$

where α_m is the magnitude of the perturbation, b is the affected width, and g determines the gradient between the unaffected region and the maximum perturbation. Both b and g are based on inspection of vibrationally excited nitric oxide (Sánchez-González *et al.*, 2012*a*,*b*), although these may be modified for other molecules. To

reproduce a grid based on LICES, perturbations perpendicular to the x-z plane are randomly distributed along lines in x and z. The number of lines, or namely LICES, along x and z are n_x and n_z, with the total number being $N_l = n_x + n_z$. Throughout the chapter the subscript l corresponds to quantities evaluated at the LICES.

The velocity u_{i_l} and temperature T_l along the LICES may then be described by:

$$\alpha_{i_l} = \alpha_{\mathrm{ref}_i} + \sum_{l_x=1}^{n_x} \left(\alpha_{m_i} - \frac{\alpha_{m_i}}{1 + \exp\left[g \left(b - \sqrt{(y - y_l)^2 + (z - z_l(l_z))^2} \right) \right]} \right) w_x(l_x) + \sum_{l_z=1}^{n_z} \left(\alpha_{m_i} - \frac{\alpha_{m_i}}{1 + \exp\left[g \left(b - \sqrt{(x - x_l(l_x))^2 + (y - y_l)^2} \right) \right]} \right) w_z(l_z) \tag{2.15}$$

where α is either velocity or temperature, α_{ref} is the reference value, x_l and z_l are the location of each LICES in the x and z planes, and y_l is the location of the grid in y, which for the simulations presented is at $\pi/4$ away from the inlet. The random distribution along each LICES is given by a sum of $\zeta_{\max}$ sine waves described by:

$$w_{x,z} = \sum_{\zeta=1}^{\zeta_{\max}} \left(\sum_{\kappa=1}^{\kappa_{\max}} \sin\left[\kappa x + \mathrm{rnd}(\kappa, \zeta) \right] \right) \tag{2.16}$$

where κ is an integer to determine the frequency, with upper bound fixed by $\kappa_{\max}$. The phase shifting is provided by rnd, a random number between 0 and 2π which changes for each ζ and κ, as well as for each l_x and l_z such that no two LICES have the same random distribution. For the velocity perturbations w varies between -1 and 1, while for the temperature perturbations it varies between 1 and 1.15, such that fluctuations are 15% of T_m. A graphical representation of a grid thus generated can be seen in Fig. II.5. Applying these perturbations involves having very

large gradients and strong fluctuations in both fluid and thermodynamic variables. It is therefore crucial to asses whether the numerical scheme used can capture accurately the imposed perturbations. The following section will describe the resolution criterion to guarantee properly resolved simulations.

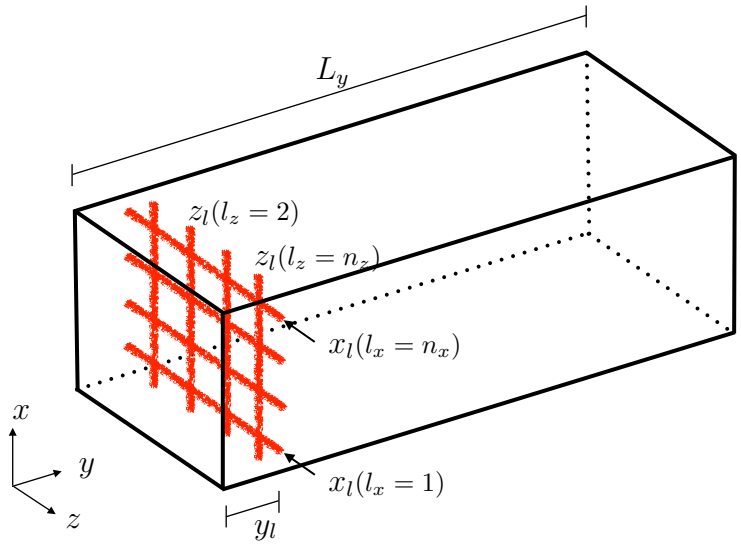

Figure II.5. Schematic of grid based on LICES with $n_x = 4$ and $n_z = 4$. Each red line represents one LICES at a particular x_l or z_l location (dimensions not to scale).

II.B.2. Convergence study

Representing the strong fluctuations in velocity and temperature from the photodissociation of molecules is a very challenging numerical problem. The perturbations create very large gradients in both velocity and temperature. Thus, one needs to perform a numerical study to guarantee grid converged results. Furthermore, it would be useful to find resolution criteria that can, a priori, identify appropriate simulations parameters for a given condition. This is our purpose next.

With the distribution proposed in Eq. (2.16) the parameters that have a first order effect on the resolution are: u_m, T_m, g, and b. For the functional forms of the perturbations and the values of $\kappa_{\max}$ used, one finds that the largest gradients will scale with the parameter g.

Following II.A.2 a first requirement for a simulation to accurately resolve regions of intense but concentrated fluctuations is to require the grid spacing Δx to be small enough to capture the largest gradient imposed. Formally this can be expressed as $u_{\max}/\Delta x \sim (\partial u/\partial x)_{max}$ where $u_{\max}$ is the largest velocity and $(\partial u/\partial x)_{max}$ is the largest gradient imposed at the LICES. Using Eq. (2.14) we can compute the maximum gradient imposed as well as the maximum velocity to form a non-dimensional resolution parameter:

$$G \equiv \frac{2N_x}{\pi\, g} \tag{2.17}$$

which has to be larger than some minimum value. This kinematic parameter, however, while necessary is found to be insufficient to guarantee converged simulations from extensive analysis of our DNS database. Consistent with II.A.2, a second dynamic parameter was necessary to assure accuracy.

This dynamic parameter was found to take the form of a Reynolds number using the parameters that define the LICES. Extensive analysis of our DNS database suggest that the appropriate resolution Reynolds number can be defined as:

$$R_k = \frac{\sqrt{K_0}\,\Delta x}{\nu(\langle T\rangle_l)} \tag{2.18}$$

where $K_0 = 1/2\,\langle u_1^2 + (u_2 + u_{\mathrm{ref}_2})^2 + u_3^3\rangle_l$ is the total kinetic energy of the system at $t = 0$. Angular brackets are used for spatial averages, where the subscript indicates the location. In this case, $\langle\rangle_l$ indicates that the averages are taken over volume

occupied by the LICES. If averages are taken along y over $x-z$ planes $\langle\rangle_y$ will be used. Similarly for $\langle\rangle_x$ and $\langle\rangle_z$.

To approximate the energy introduced strictly based on initial conditions, the mean velocity $\langle u\rangle_l$ can be taken as the integration of the distribution Eq. (2.16) in the $y-z$ plane over the area affected by the lines. Simplifying this analysis to a single line, the mean becomes:

$$\begin{aligned}\langle u_l\rangle &\approx u_{\text{ref}} + \frac{1}{\pi r_l^2}\int_{-\infty}^{\infty}\int_{-\infty}^{\infty} u_m - \frac{u_m}{1+\exp\left[g\left(b-\sqrt{y^2+z^2}\right)\right]}\,dy\,dz \\ &= \frac{-2\pi u_m Li\left[2,-\exp[g\,b]\right]}{\pi(r_l\,g)^2}\end{aligned} \tag{2.19}$$

where the Li is the Polylogarigthm function $Li[n,k] \equiv \sum_{k=1}^{\infty} z^k/k^n$ and r_l is the radius of the LICES where the perturbation is is greater than 1% of the maximum u_m. Solving for r_l and substituting back into Eq. (2.19), the mean velocity becomes:

$$\langle u_l\rangle \approx u_{\text{ref}} + u_m - \frac{u_m}{1+\exp\left[g\left(b-\sqrt{\frac{\left(g\,b+\log\left[99\right]\right)^2}{g^2}}\right)\right]} \tag{2.20}$$

The length scale in Eq. (2.18) taken to be the grid spacing $\Delta x = L_x/N_x$, where N_x is the number of grid points along x. For all the simulations the grid spacing is the same in all directions, that is, $\Delta x = L_x/N_x = \Delta y = L_y/N_y = \Delta z = L_z/N_z$. The kinematic viscosity is formed using Sutherland's Law for viscosity with the mean temperature of the LICES and reference density, assuming the instantaneous change of density is small:

$$\nu(\langle T_l \rangle) = \left(\frac{C_{v_1}(T_{\text{ref}} + \langle T_l \rangle)^{3/2}}{(T_{\text{ref}} + \langle T_l \rangle) + C_{v_2}} \right) / \left(\frac{p_{\text{ref}}}{R \langle T_l \rangle} \right) \tag{2.21}$$

where C_{v_1} and C_{v_2} are Sutherland's Law coefficients, T_{ref} and ρ_{ref} are the reference temperature and density of the flow, R is the universal gas constant and $\langle T \rangle_l$ is calculated using Eq. (2.20) with temperature instead of velocity.

To establish the convergence criterion a suitable variable must be chosen to asses grid convergence. Since variables dominated by small-scale activity such as velocity gradients or dissipation are more sensitive to resolution effects, a natural candidate is the averaged dissipation rate $\langle \epsilon \rangle$. The relative error can be computed using the highest resolution available to approximate the exact value.

$$\varepsilon_{\langle \epsilon \rangle} = \frac{|\langle \epsilon \rangle_N - \langle \epsilon \rangle_{N_{\max}}|}{\langle \epsilon \rangle_{N_{\max}}} \tag{2.22}$$

The error for mean dissipation rate ε_ϵ as well as that for mean turbulent kinetic energy ε_K, similarly defined, can be seen in Fig. II.6. The error for mean dissipation rate appears to collapse for all simulations as $\sim R_k^3$. The error for K shows more spread than the dissipation rate, +but it is approximately two orders of magnitude smaller for all values of R_k. Thus we consider simulations to be grid converged if ε_ϵ is below 2%, which corresponds to $R_k \lesssim 40$. DNS also demonstrates that satisfying this condition for R_k simultaneously satisfies the kinematic condition for G.

II.C. Thermal non-equilibrium governing equations

In order to study the effects of thermal non-equilibrium, we may treat diatomic molecules as a harmonic oscillator, where the evolution of vibrational energy of a

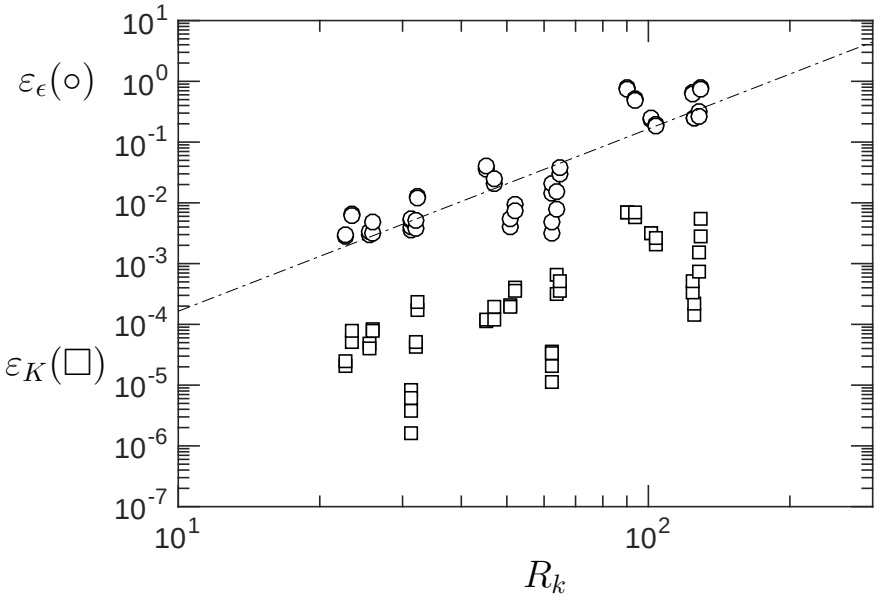

Figure II.6. Error of mean dissipation rate and turbulent kinetic energy as a function of resolutions Reynolds number R_k for simulations with different $\langle u_l \rangle$, $\langle T_l \rangle$, g and N. Circles correspond to ε_ϵ, while squares correspond to ε_K.

fluid element convected by the macroscopic velocity u_i can be written as (Hirschfelder *et al.*, 1954):

$$\frac{\partial(\rho e_v)}{\partial t} + \frac{\partial(\rho e_v u_i)}{\partial x_i} = \frac{\partial}{\partial x_i}\left(D\frac{\partial e_v}{\partial x_i}\right) + \frac{\rho}{\tau_v}\left(e_v^* - e_v\right) \tag{2.23}$$

where u_i is the advecting velocity field and D is the diffusion coefficient. The diffusion coefficient is taken to be the same as that for translational energy, which may be written in terms of the Prandtl number Pr as:

$$D = \frac{\mu\gamma}{Pr} \tag{2.24}$$

where γ is the ratio of specific heats. The last term in Eq. (2.23) represents the exchange mechanism between translational and vibrational energy modes according to Landau-Teller relaxation (Landau & Teller, 1936). From quantum mechanics, the

vibrational energy per unit mass for harmonic oscillators in thermodynamic equilibrium with translational temperature T is given by

$$e_v^* = \frac{R\theta_v}{e^{\theta_v/T} - 1} \tag{2.25}$$

where θ_v denotes the characteristic vibrational temperature and R is the universal gas constant. The translational and rotational energies are assumed to be in equilibrium, which is justified given the relatively small number of collisions needed for equilibration (Hirschfelder *et al.*, 1954). We denote the combination of both energies as $e = e_t^* + e_r^* = (5/2)RT$, where the asterisk is dropped in e for simplicity of the notation. τ_v corresponds to the characteristic relaxation time, which can also be computed from theoretical considerations as:

$$\tau_v = \frac{c_1^{\tau_v}}{p} e^{(c_2^{\tau_v}/T)^{1/3}} \tag{2.26}$$

where $c_1^{\tau_v}$ and $c_2^{\tau_v}$ are constants which depend on the molecular system (Hirschfelder *et al.*, 1954). As in past studies (e.g. Olejniczak & Candler, 1995; Bertolotti, 1998), Eq. (2.23) is solved along with the compressible Navier-Stokes equations Equations (2.10) to (2.12). For these simulations, compact finite differences of tenth order with penta-diagonal system of equations are used. Numerical details of the simulations can be found in (Jagannathan & Donzis, 2015).

To reach a state of stationary homogeneous isotropic turbulence, a stochastic forcing is used at the largest scales using the solenoidal (SF) and dilatational (DF) modes in Eq. (2.11), as well as a combination of SF with stochastic forcing also in the internal energy equation Eq. (2.12) (EF). Details on the specifics of the forcing may be found in (Donzis & Jagannathan, 2013). Purely solenoidal forcing (SF)

is obtained with $s = 1$; purely dilatational forcing (DF) is obtained with $s = 0$. The reason for using multiple forcing schemes is to assess universal aspects of the flow as well as to reach regimes difficult to access otherwise such as those with very strong temperature fluctuations enabled by EF. To maintain a statistically steady state, energy is removed from the system uniformly so that the mean temperature is kept constant as in (Donzis & Jagannathan, 2013). Consistent with results in the literature (e.g. Wang *et al.*, 2010), our simulations show that results are insensitive of the details of the energy removal mechanism (Jagannathan & Donzis, 2015).

II.D. Numerical computation of Helmholtz decomposition: Windowing

Understanding the effect of compressibility in turbulent flows can further help understand the different energy exchange mechanisms that enhance or inhibit turbulence. It is often useful to isolate compressibility effects using the so-called Helmholtz decomposition which separates the velocity field into a dilatational and a solenoidal component. In the absence of boundary effects or periodic boundary conditions, the velocity field may be written as:

$$\mathbf{u} = \mathbf{u^s} + \mathbf{u^d} \tag{2.27}$$

where the solenoidal component $\mathbf{u^s} = \nabla \times \psi$ satisfies $\nabla \cdot \mathbf{u^s} = 0$, while the dilatational $\mathbf{u^d} = \nabla \phi$ satisfies $\nabla \times \mathbf{u^d} = 0$ (Sagaut & Cambon, 2008). This decomposition can be trivially done in Fourier space, where the Fourier transform of $\mathbf{u^s}$, $\hat{\mathbf{u}}^{\mathbf{s}}(\mathbf{k})$ is orthogonal to the wave number vector $\mathbf{k}$, and $\hat{\mathbf{u}}^{\mathbf{d}}(\mathbf{k})$ is parallel to $\mathbf{k}$. The variance of $\mathbf{u}$, which is related to the kinetic energy, can also be split into a solenoidal and dilatational part, where the ratio of dilatational to total velocity variance: $\chi = \langle u_i^d u_i^d \rangle_* / \langle u_i u_i \rangle_*$

provides a measure of compressibility at the large scales, or energy containing range (Lele, 1994; ?; ?). This decomposition has been vastly used in literature for homogeneous compressible box turbulence with periodic boundary conditions (Lele, 1994). However, a much more challenging situation is to perform such a decomposition in a non-homogeneous flow. This is a well known open problem (Sagaut & Cambon, 2008). In the absence of periodicity, the velocity field may not be transformed to Fourier space without introducing large errors at high wavenumbers from the discontinuity that appears at the boundaries of the non-periodic direction. In the next section we propose a new method that allows for Helmholtz decomposition in non-periodic domains. The method we propose is based on classical windowing techniques, such as the Tukey or Blackman, used for signal processing. A detail description of the method and error study follows in the next section.

II.D.1. Windowing

There has been substantial work in the field of signal processing devoted to windowing of signals. Fourier series can represent any signal as a sum of sines and cosines, where the signal is of infinite length. When we have finite length signals, Discrete Fourier transforms must be used to recover the information of the signal. Discrete Fourier transforms, commonly implemented as Fast Fourier Transforms (FFT) require the signal to be periodic, such that it can be repeated to approximate an infinite signal. When a signal is not periodic, this procedure will introduce discontinuities at the boundaries which lead to spectral leakage (Harris, 1978) and consequently the appearance of artificial frequencies. To avoid this discontinuity, the signal can be

made periodic by matching the function value at the boundaries. This is most easily done by forcing the boundaries values and their derivative to zero which is simply implemented by multiplying the function, say f, by a "window" function wi. The signal to be transformed to Fourier space is now $f(y)\mathrm{wi}(y)$, when transformed along the y axis. A detailed summary of windows and their properties can be found in Harris (1978). A classical window is the Tukey window, which may be expressed as (Geckinli & Yavuz, 1978):

$$\mathrm{wi}(y) = \begin{cases} 1 & |y| < \beta\pi \\ \dfrac{1}{2} + \dfrac{1}{2}\cos\left(\dfrac{|y| - \beta\pi}{1-\beta}\right) & \beta\pi \leqslant |y| \leqslant \pi \end{cases} \tag{2.28}$$

for a domain of $L_y = 2\pi$ with origin at 0 (from -π to π). The parameter β determines the amount of domain windowed as well as the smoothness of the transition from 1 to 0 close to the boundaries, as can be seen from Fig. II.7(left) where two different β are shown. For simplicity we will call the left and right boundaries of the domain y_{in} and y_{out} respectively, and define $y_{\mathrm{wi}_1} = y_{\mathrm{in}} + \beta\pi$ and $y_{\mathrm{wi}_2} = y_{\mathrm{out}} - \beta\pi$, which represent the starting regions for the window. We apply the window along y where the velocity field is non-periodic by $u_i(x, y, z) = u_i(x, y, z)\mathrm{wi}(y)$. A typical windowed velocity field is shown in Fig. II.7(right). After a window is applied, the velocity field becomes periodic and can be transformed to Fourier space such that the Helmholtz decomposition may be applied.

One way of assessing how much windowing distorts the original signal is by computing, for example, velocity gradients in Fourier space, transforming them back to physical space and comparing the results to velocity gradients computed in physical

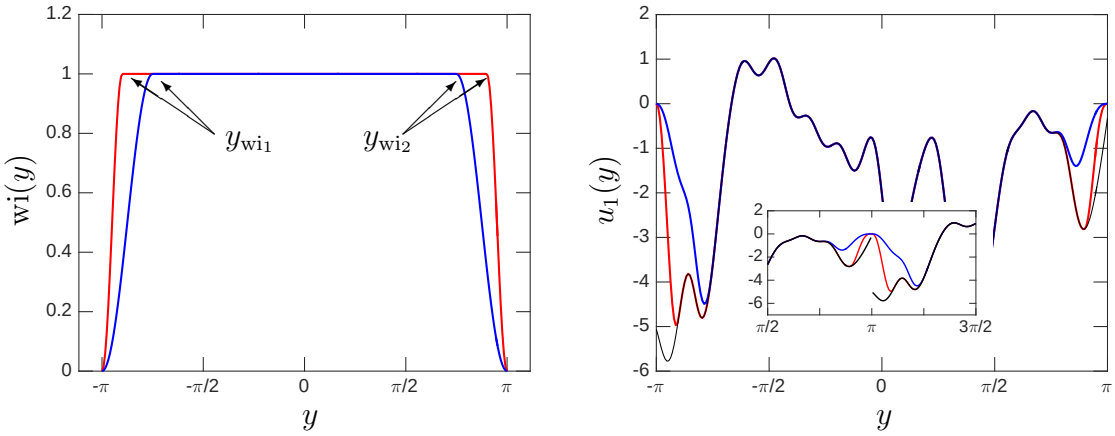

Figure II.7. Left: Tukey window with β =0.8 (blue) and β =0.9 (red). Right: window applied to sample velocity at a particular x and z location. Inset shows the discontinuity generated when the signal is repeated in space and the effect of windowing.

space using high-order differential methods. We use sixth order compact schemes, as described by Lele (1992). Compact schemes offer spectral-like resolution and have been widely used in literature for turbulent flows (e.g. Lee *et al.* (1991); Petersen & Livescu (2010)).

To compare the gradients computed with spectral methods (with windowing) and compact schemes, a segment of 2π is taken at the end of the domain along the axial (y) direction, such that the domain is of size $(2\pi)^3$. The last segment length of 2π is chosen as the flow is turbulent, or nearly turbulent at this location, though other locations have been tested and results are still consistent.

Applying any classical windowing method forces the velocity field at the inlet and outlet to 0. Consequently, the variance of velocity and velocity gradients over the planes where the windowing is effective is reduced. To understand how the velocity field is modified by windowing, we compute the error for the variance of velocity gradients between spectral methods, after windowing is applied, and sixth

order compact schemes. Fig. II.8 shows the relative error for the variance of velocity gradients. The first and third components of velocity are periodic, therefore the error between spectral and compact schemes should be zero if no windowing is applied ($\beta = 1$). On the other hand, for $\beta = 1$, the error will be largest for the second component due to the effect of spectral leakage. Decreasing β will reduce the error on the second component, but will introduce error on the first and third. This is so because all velocity fluctuations in the x-z plane go to zero at the boundaries. From Fig. II.8 we find the minimum error for $\partial/\partial x_2$ at approximately $\beta = 0.8$ for u_1 and u_3 and at $\beta = .75$ for u_2.

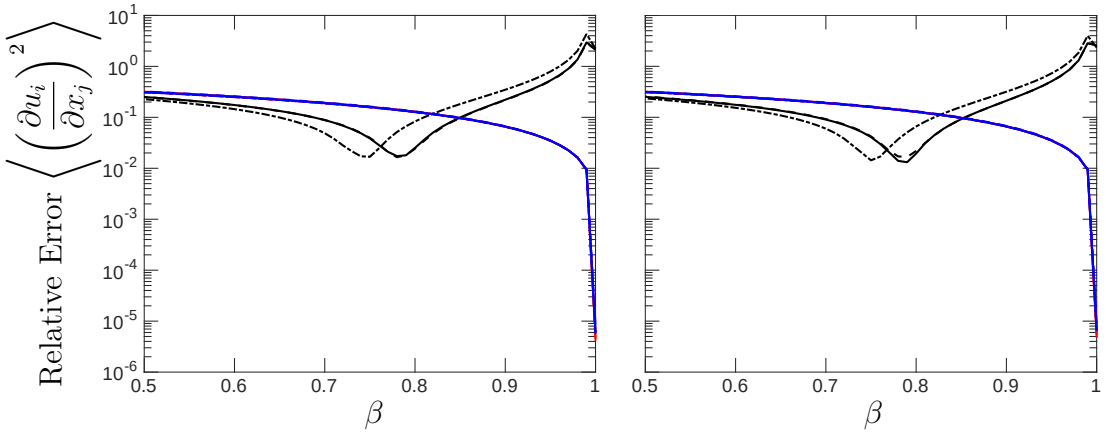

Figure II.8. Relative error for variance of velocity gradients $\left\langle \left(\frac{\partial u_i}{\partial x_j} \right)^2 \right\rangle$ between spectral and sixth order compact schemes for different β using the Tukey window. Different colors represent $j = 1$ (blue), 2 (black), 3 (red), and line styles $i = 1$ (solid), 2 (dash-dot), 3 (dashed). Left and right correspond to two cases with different Reynolds number.

With other classical window methods, such as the Blackman, we have seen similar results. With conventional windows, where the derivatives at the boundaries are matched by taking the values to zero, the variance over the entire plane is drastically

reduced. The velocity fluctuations in the x-z plane goes to zero at the boundaries. Therefore, applying a window in the y component also has a large impact on gradients along the x and z components. As the error decreases along y, it increases along the other two components, making it hard to find an adequate β. To minimize the effect of reduced fluctuations in x and z, we propose a new windowing technique. Instead of matching the derivative at the boundaries by forcing the velocity to zero, we fit a cubic polynomial between y_{wi_2} and y_{wi_1} for each point on the x-z plane. The proposed window can be written as:

$$\mathrm{wi}(x,y,z) = \begin{cases} 1 & |y| < \beta\pi \\ \dfrac{c_1(x,z)\xi(y)^3 + c_2(x,z)\xi(y)^2 + c_3(x,z)\xi(y) + c_4(x,z)}{u_i(x,y,z)} & \beta\pi \leqslant |y| \leqslant \pi \end{cases} \tag{2.29}$$

for a domain of $L_y = 2\pi$ with origin at 0 (from -π to π), where ξ is a transformed y coordinate. The transformed y coordinate ξ shifts the first half of the domain by $+\pi$, from the inlet to $L_y/2$, such that it connects the outlet and inlet. The effect of using ξ instead of y is that the discontinuity will appear in the middle of the domain as oppose to the inlet and outlet, as shown in the inset of Fig. II.9b.

In order to match the velocity as well as the derivative of the function at the two boundaries one obtains four equations for the four unknown coefficients in Eq. (2.29). The resulting system is then:

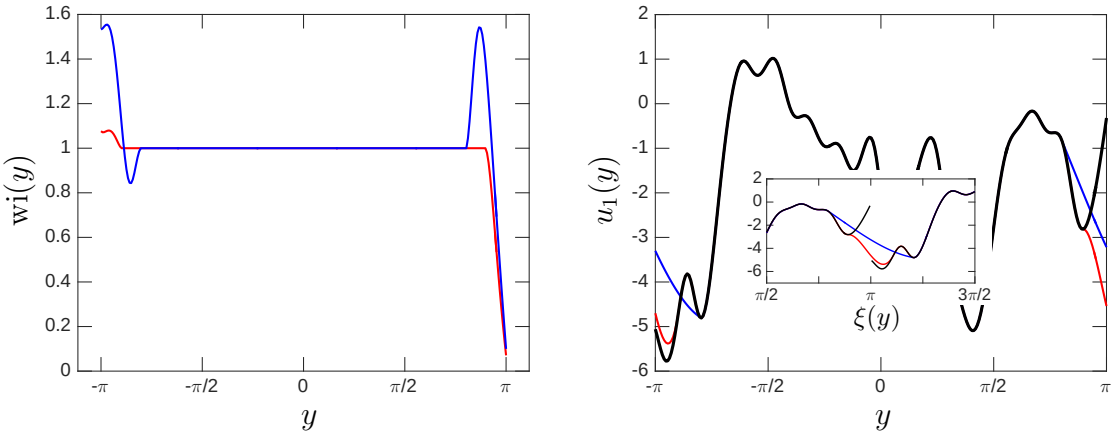

Figure II.9. Left: Cubic window with $\beta = 0.8$ (blue) and $\beta = 0.9$ (red). Right: window applied to sample velocity at a particular x and z location. Inset shows the velocity as a function of the transformed coordinate ξ and the effect of windowing.

$$\begin{bmatrix} \xi(y_{\mathrm{wi}_1})^3 & \xi(y_{\mathrm{wi}_1})^2 & \xi(y_{\mathrm{wi}_1}) & 1 \\ \xi(y_{\mathrm{wi}_2})^3 & \xi(y_{\mathrm{wi}_2})^2 & \xi(y_{\mathrm{wi}_2}) & 1 \\ 3\xi(y_{\mathrm{wi}_1})^2 & 2\xi(y_{\mathrm{wi}_1}) & 1 & 0 \\ 3\xi(y_{\mathrm{wi}_2})^2 & 2\xi(y_{\mathrm{wi}_2}) & 1 & 0 \end{bmatrix} \begin{bmatrix} c_1(x,z) \\ c_2(x,z) \\ c_3(x,z) \\ c_4(x,z) \end{bmatrix} = \begin{bmatrix} u_i(x, y_{\mathrm{wi}_1}, z) \\ u_i(x, y_{\mathrm{wi}_2}, z) \\ \frac{\partial}{\partial y} u_i(x, y_{\mathrm{wi}_1}, z) \\ \frac{\partial}{\partial y} u_i(x, y_{\mathrm{wi}_2}, z) \end{bmatrix} \tag{2.30}$$

for each x and z, such that the value and derivative at y_{wi_1} and y_{wi_2} are matched with the original velocity field. This minimizes the effect of reduced variance in the x-z planes where the window is effective. With this windowing technique, the relative error for derivatives along x and z is nearly constant and below 2% from $\beta = 0.8$ to $\beta = 0.98$. Similarly to the Tukey window, the error for derivatives along y decreases with decreasing β. However, the minimum is now found to be at approximately $\beta = 0.9$, and consistent for the three components of velocity. This windowing method has also shown to be consistent for different set of initial conditions as seen in Fig. II.10.

Applying this new windowing method with $\beta = 0.9$ bounds the error for the

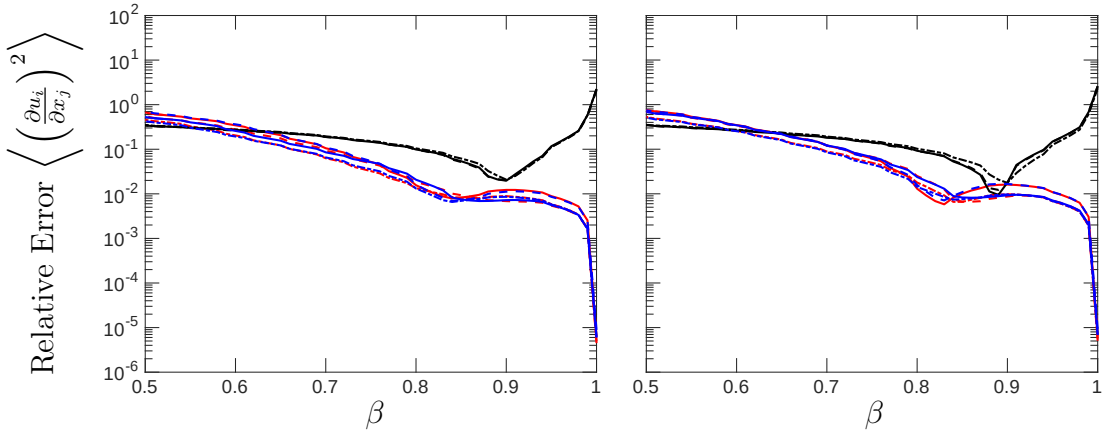

Figure II.10. Relative error for variance of velocity gradients $\left\langle \left(\frac{\partial u_i}{\partial x_j}\right)^2 \right\rangle$ between spectral and sixth order compact schemes for different β using the cubic window. Different colors represent $j = 1$ (blue), 2 (black), 3 (red), and line styles $i = 1$ (solid), 2 (dash-dot), 3 (dashed). Left and right correspond to two cases with different Reynolds number (same simulations as Fig. II.8).

variance of velocity derivatives to approximately 2%, independent of initial conditions and domain location. We may then apply the Helmholtz decomposition to study the effect of dilation on the large scales.

CHAPTER III

TURBULENCE GENERATION IN INCOMPRESSIBLE FLOWS

III.A. Flow evolution

The flow evolution towards a fully turbulent state will depend on a number of parameters characterizing the simulations and initial conditions. These are summarized in Table II.1. Some will have a first order effect, while others are not as determinant in the evolution. The next few sections will try to address what the dominating parameters are, and how energy is re-distributed from the LIKES to the rest of the domain to create fully developed turbulence.

III.A.1. Characteristic time scales

A typical evolution of the mean dissipation and the Taylor's Reynolds number is shown in Fig. III.1. Initially, independent of how high the Reynolds number is, the flow is not turbulent. It has not evolved sufficiently to forget the initial condition and create all the relevant scales of motion that characterize such a flow. From Fig. III.1a, we find that before the mean dissipation starts to decay, it peaks at a characteristic time scale. We call this time τ^*, which we find, depends on the initial conditions and flow properties. It will be shown in future sections that the maximum dissipation becomes an important parameter in the evaluation of the onset of turbulence, consistent with results in the literature (Yamamoto & Hosokawa, 1988; **?**; **?**). The maximum dissipation and the corresponding R_λ are marked on Fig. III.1

as $\langle\epsilon\rangle^*$ and R_λ^* respectively.

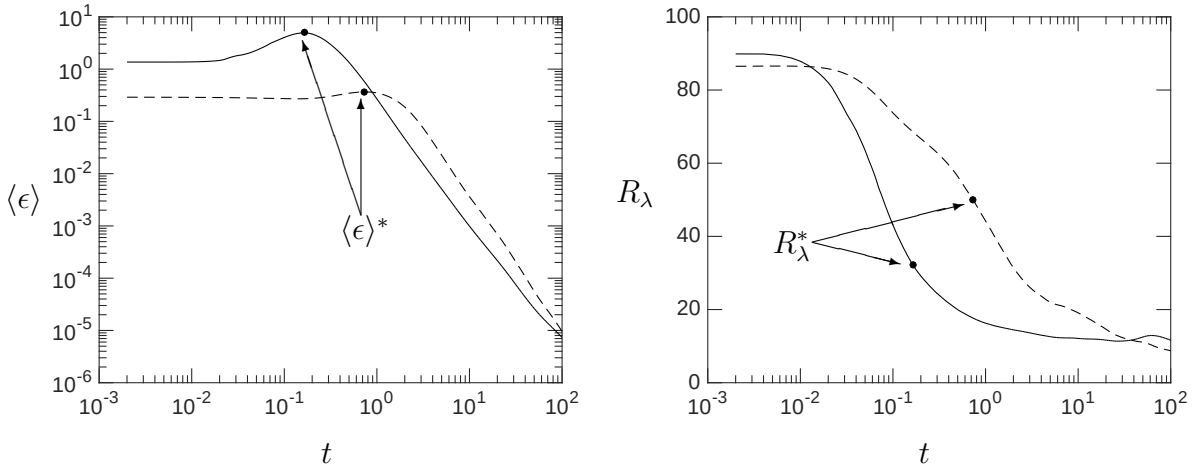

Figure III.1. Evolution of $\langle\epsilon\rangle$ and R_λ for two cases with different viscosity, N_l, and initial perturbation. Solid lines correspond to case 5 from Table II.1 while dashed lines correspond to case 18. Point of maximum averaged dissipation marked on both plots (τ^*).

An objective of this chapter is to identify the transition of the flow to fully turbulent. There are several measures to determine such a condition, including skewness of the velocity gradient, root mean square velocity ratios, and isotropic spectra relations among others which are studied next.

III.A.1.a. Velocity and velocity gradients

To quantify the effectiveness of LIKES to generate turbulence we now focus on statistics widely used to characterize turbulent flows behind physical grids as well as other canonical flows. One measure of the energy transfer for large to small scales and the generation of vortical motions is the skewness of longitudinal velocity gradients (S_{u_x},S_{v_y},S_{w_z}), which for fully developed turbulence approaches the value

of (Tavoularis *et al.*, 1978; Sreenivasan & Antonia, 1997) -0.5. The evolution of S_{u_x} in our simulations is seen in Fig. III.2 for two representative cases. Again, marked in

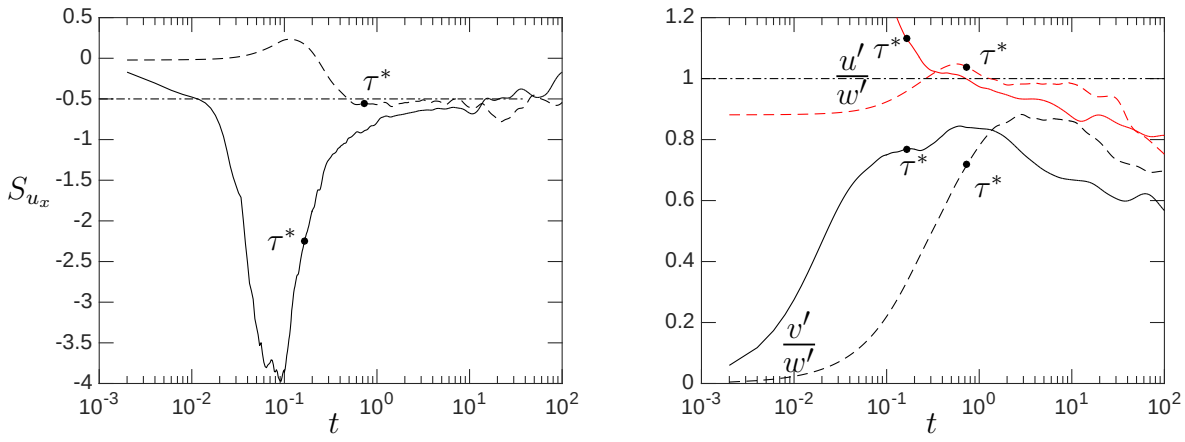

Figure III.2. Evolution for skewness of the velocity gradient S_{u_x} left and ratio of root mean squared velocities right. Same initial conditions as Fig. III.1. Colors on right figure correspond to u'/w' (red) and v'/w' (black). Horizontal dash-dot lines correspond to fully developed isotropic turbulence.

black circles are the corresponding τ^* for both cases. At the peak of the dissipation, we see that only one of the cases has reached $S_{u_x} \approx -0.5$. This indicates that τ^* is not in general a measure of when a fully developed state has been achieved. As we will see shortly, however, τ^* is an indicator provided some conditions are satisfied at $t = 0$.

The ratio of the root mean squared velocities (denoted by a prime), shown in Fig. III.2b, can also be used to study large scale anisotropy. Initially, the y-component of velocity is zero and so is the ratio v'/w'. On the other hand, there is an initial perturbation in the x-component of velocity to satisfy continuity, so $u'/w' \neq 0$ at $t = 0$. Two different behaviors can be seen in the figure, for u'/w' and

v'/w' respectively. While u'/w' asymptotes at unity, v'/w' asymptotes at approximately 0.8 after τ^*, a departure also observed in experiments (11; 38; 74) due to the inhomogeneity caused by the initial conditions. Given that the two simulations shown have different initial conditions, it appears that the trend to isotropy at all scales will depend on these, and that τ^* will not always be sufficient to guarantee fully developed turbulence.

III.A.1.b. Spectra and isotropy

If realistic turbulence is established at $t = \tau^*$, it is expected that the flow acquire also structural signatures of fully developed turbulence. For example, we can expect the three-dimensional spectrum to approach, under K41 (**?**) scaling, that of isotropic turbulence at the same Reynolds number. Fig. III.3 shows the spectra for two simulations (a and b) with different initial conditions at four different times in the evolution of the flow, namely $t = 0$, $0.1\,\tau^*$, and $2\,\tau^*$. The difference between the simulations is the Reynolds number based on the initial conditions R_I, which will be presented in the following section. For now we will focus on Fig. III.3b, which has the highest R_I. Initially the spectrum is defined by the initial conditions and is thus, not expected to be universal in the sense of K41. However, as the flow evolves in time and reaches τ^* it collapses with the spectrum for isotropic turbulence (dashed-dot) from a steady state simulation using stochastic forcing (e.g. Refs. (25; 34)), consistent with K41 small-scale universality. Since it is a relatively low R_λ flow, there is not a well defined inertial range.

Furthermore, if turbulence is expected to acquire a universal behavior indepen-

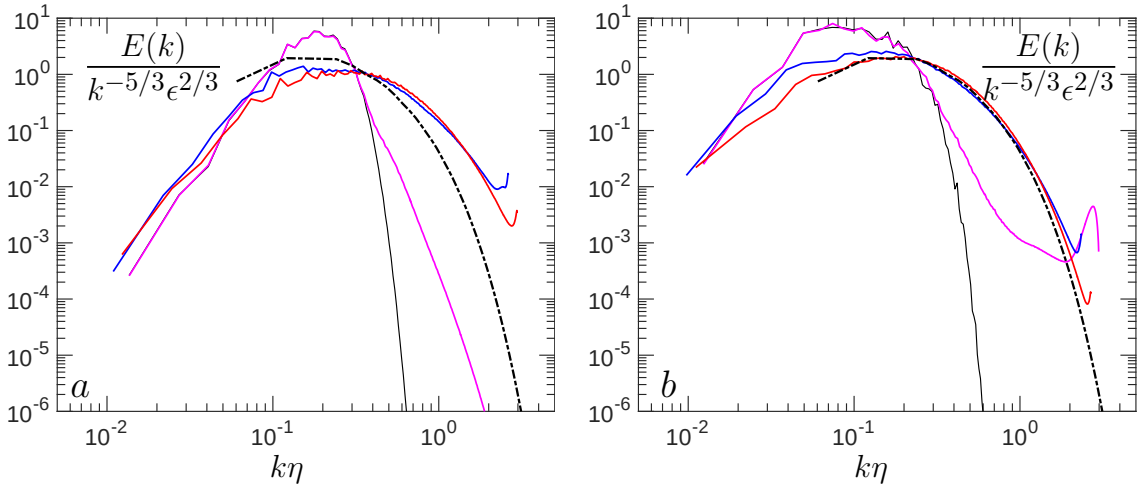

Figure III.3. Spectra for case 11 (left) with $R_I \sim 50$ and case 12 (right) with $R_I \sim 573$ at four different times: Initial conditions $t = 0$ (black), $0.1\,\tau^*$ (magenta), τ^* (blue), $2\,\tau^*$ (red). The dissipation and Taylor's microscale is the instantaneous for each case. For comparison to forced steady state simulations, the dashed curve is a $R_\lambda \sim 38$ with 128^3 resolution.

dent of the mechanism of energy injection or initial conditions in the case of decaying turbulence, it is commonly accepted that turbulence should evolve towards a state of statistical isotropy (Monin & Yaglom, 1975). Since scales comparable to the characteristic scales of the forcing mechanism may always have a signature of some of the geometrical features of this forcing, isotropy is generally only expected at small scales. Thus, different indicators of anisotropy have been used in the literature to determine how (an)isotropic different scales are at a given time. For example the different components of the one-dimensional energy spectra can be related to each other and to the three-dimensional energy spectra by isotropic relations (Monin & Yaglom, 1975). For fully isotropic turbulence, the longitudinal energy spectrum $E_{11}(k_1)$ can be related to its transverse counterpart $E_{22}(k_1)$ according to (79):

$$E_{22}(k_1) = \frac{1}{2}\left(E_{11}(k_1) - k_1 \frac{\mathrm{d}E_{11}(k_1)}{\mathrm{d}k_1}\right) \tag{3.1}$$

All longitudinal components $E_{11}(k_1)$, $E_{22}(k_2)$, $E_{33}(k_3)$ should be equivalent for isotropic turbulence. From Fig. III.4, we observe that $E_{22}(k_1)$ from DNS becomes close to Eq. (3.1) computed using $E_{11}(k_1)$ also from DNS, at τ^* and even closer at $2\tau^*$. It is also seen that all longitudinal components of the energy spectra are similar at τ^*. All the components collapse in the dissipative range. However, as expected, there are some disparities at large scales even for latter times.

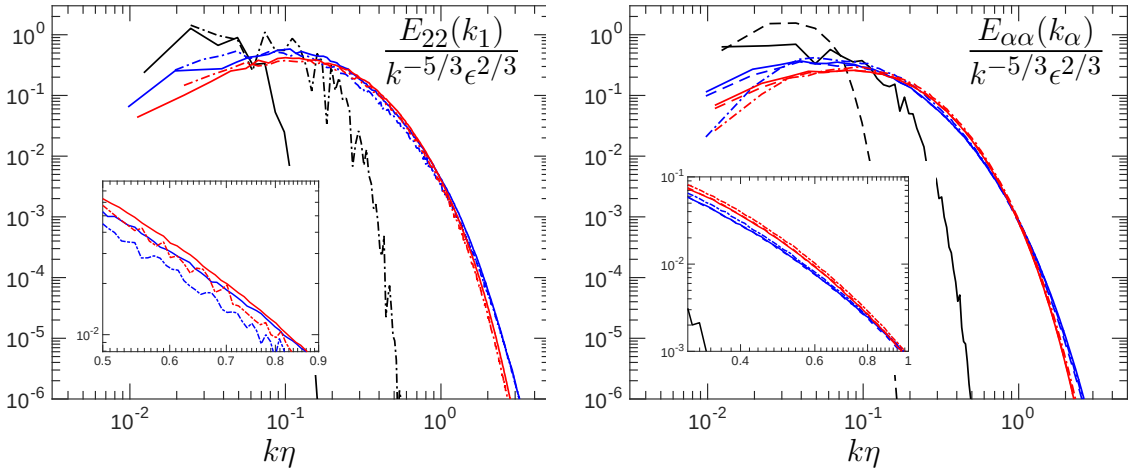

Figure III.4. Left: one dimensional transverse energy spectra from DNS in solid, and from isotropic relation Eq. (3.1) using longitudinal counterpart in dash. Right: longitudinal energy spectra $E_{11}(k_1)$ (solid), $E_{22}(k_2)$ (dash-dot), $E_{33}(k_3)$ (dash). Different colors correspond to different times $t = 0$ (black), τ^* (blue), and $2\,\tau^*$ (red). Dissipation and Taylor's microscale is the instantaneous for each case. Both plots correspond to case 12 with $R_I \sim 573$. Inset on both figures is a close-up view of the same quantity.

The anisotropy at large scales, is widely quantified by the departures of the Reynolds stress tensor $\langle u_i u_j \rangle$ from an isotropic tensor. In the absence of a production term, the evolution of the Reynolds stresses is given by:

$$\frac{\mathrm{d}}{\mathrm{dt}}\langle u_i u_j \rangle = R_{ij} - \epsilon_{ij} \tag{3.2}$$

where d/dt is the substantial derivative and the pressure-strain and dissipation rate tensors are:

$$R_{ij} = p\left\langle \frac{\partial u_i}{\partial u_j} + \frac{\partial u_j}{\partial u_i} \right\rangle, \quad \epsilon_{ij} = 2\nu \left\langle \frac{\partial u_i \partial u_j}{\partial x_k \partial x_k} \right\rangle \tag{3.3}$$

Since the pressure-strain tensor is traceless, it does not affect the kinetic energy and its effect is solely the re-distribution of energy between the different components of the Reynolds stress tensor, playing an important role in the return to isotropy. Anisotropy is often studied through the normalized Reynolds anisotropy tensor (**?**) b_{ij}:

$$b_{ij} = \frac{\langle u_i u_j \rangle}{2K} - \frac{1}{3}\delta_{ij} \tag{3.4}$$

where K is the averaged turbulent kinetic energy $K = \frac{1}{2}\langle u_k u_k \rangle$. Clearly, for a perfectly isotropic Reynolds stress tensor, all components of the anisotropy tensor vanish identically. One can similarly define an anisotropy tensor for the dissipation rate (Antonia *et al.*, 1994):

$$d_{ij} = \frac{\langle \epsilon_{ij} \rangle}{\langle 2\epsilon \rangle} - \frac{1}{3}\delta_{ij} \tag{3.5}$$

where $\langle \epsilon \rangle = \frac{1}{2}\langle \epsilon_{kk} \rangle$ is the averaged dissipation rate. We point out that these quantities provide a quantitative measure of departures from isotropy and that the main contributions to each come from different range of scales. While b_{ij} represents large scales, d_{ij} is associated with small dissipative scales. Since the sum of the eigenvalues of both the Reynolds and the dissipation rate tensor are zero, the state of the anisotropy tensors can be defined by just two invariants, namely:

$$\mathrm{II}_b = -\frac{1}{2} b_{ij} b_{ji} \quad \mathrm{III}_b = \frac{1}{3} b_{ij} b_{jk} b_{ki} \tag{3.6}$$

$$\mathrm{II}_d = -\frac{1}{2} d_{ij} d_{ji} \quad \mathrm{III}_d = \frac{1}{3} d_{ij} d_{jk} d_{ki} \tag{3.7}$$

the first invariant, which is the trace of the anisotropic tensor, is zero. The state of turbulence can then be defined by the position occupied in a phase diagram with the second and third invariants in the vertical and horizontal axes respectively (Lumley, 1978). It can also be shown that for incompressible turbulence, not every combination of parameters is physically realizable. Only points inside the so-called Lumley triangle are realizable (Lumley & Newman, 1977). The different states (**?**) of the anisotropy tensor can be observed in Fig. III.5.

In terms of the Reynolds stress anisotropy tensor, the three vertices of the triangle represent the extreme cases where two components of the turbulent kinetic energy are zero (1C), where one component is zero and the other two are equivalent ($2C^a$), and all three components are exactly alike (isotropic turbulence). Along the top of the triangle there is two component turbulence (2C), that transitions from equal kinetic energy among the components to one much larger than the other and finally just one component. On the right side of the triangle there is rod-like turbulence, or cigar-shaped turbulence as described by Choi and Lumley (10). Finally, on the left side of the triangle (negative III), disk-like structures are observed.

The trajectories of the Reynolds stress anisotropy tensor b_{ij} and the rate of dissipation anisotropy tensor d_{ij} have been studied by several author for boundary layers and channel flows (Liu & Pletcher, 2008; Antonia *et al.*, 1994; Mansour *et al.*, 1988). Over a significant portion of the outer layer, a linear relation can be estab-

lished between the two anisotropy tensors such that $d_{ij} = f b_{ij}$, where f is a function of the turbulent Reynolds number (Antonia *et al.*, 1994). Mansour *et al.* have seen better agreement with $f = 1$ for their channel data (Mansour *et al.*, 1988). This however is not the case for turbulence generated with LIKES. As seen in Fig. III.5, a linear relationship between d_{ij} and b_{ij} is not observed. b_{ij} approaches isotropy from the two component axisymmetric state ($2C^a$) while d_{ij} does it from the one dimensional state (1C). These observations for b_{ij} and d_{ij} can be explained from the initial conditions. Since we impose one component of velocity, and satisfy continuity with a second (w and u with $v = 0$), it is expected that the flow will be initially described as two component axisymmetric at the large scales. In wavenumber space, consider a Gaussian for $\hat{w}$ located at some low wavenumber, k_0. Since continuity requires $\hat{u} = k_z/k_x \hat{w} = 0$, it is clear that when k_x and k_z are comparable and close to k_0, both components $\hat{u}$ and $\hat{w}$ will be commensurate. That is, a 2C state. For wavenumbers much lower or higher than k_0, the magnitude of $\hat{w}$ will be negligible, and only $\hat{u}$ components may be non-zero. That is, a 1C state. This can be easily visualized in Fig. III.6 where we have 1C at the smallest wave number, 2C for $0.03 < k\eta < 0.2$ and again 1C for $k\eta \geq 0.2$. Since dissipation is a small-scale quantity, typically found for (Donzis & Sreenivasan, 2010*b*) $k\eta \gtrsim 0.1$, it is expected that d_{ij} will start from the one-dimensional region of the Lumley triangle at $t = 0$. The differences in the trajectories between the LIKES and boundary layers could also be the result of the 2-dimensionality of the boundary layer. An experimental setup that would resemble our initial conditions more closely is grid generated turbulence passed through a contraction. The change in area will amplify the transverse velocity

fluctuations(Comte-Bellot & Corrsin, 1966), forcing two principal components (2C).

The return to isotropy for grid generated turbulence has been studied by several authors (54; 103; 10). Of particular interest are the experiments with axis symmetric contraction, or negative third invariant ($III < 0$), which as mentioned previously corresponds more closely to the conditions generated by LIKES. The third invariant is negative when two principal components are large, consistent with our simulations as $v = 0$. We see very close agreement with the data of Le Penven *et al.*(54) and Tucker & Reynolds (103) for their configuration with negative third invariant ($III < 0$). Similarly, the experiments by Choi & Lumley (10) show very good agreement for their sets with axis symmetric contraction for pancake-shaped turbulence. On the other hand, the data from these references for turbulence through an expansion is more consistent with boundary layers, where only one principal components dominates, as can be appreciated in Fig. III.5.

As we mentioned above, b_{ij} and d_{ij} are associated with large and small scales respectively, so it is expected that the rate of return to isotropy will be faster for d_{ij} when compared to b_{ij}. Results show that the starting location in the Lumley triangle for both tensors is on the 2C line, with b_{ij} being very close to axisymmetric for the two cases presented in the figure, as well as all the others in our database, which is expected since there is no initial v component of velocity. From the previous discussion, it is also expected that d_{ij} will be less axisymmetric than b_{ij} and as predicted, d_{ij} returns to isotropy at a faster rate than b_{ij}. This is also consistent with results from the core region of a channel flow, where d_{ij} is closer to the axis symmetric state than the Reynolds anisotropy tensor (Mansour *et al.*, 1988). The Reynolds

anisotropy tensor at $2\tau^*$ was also compared to our database of forced homogeneous-isotropic turbulence with similar Reynolds number (Donzis & Sreenivasan, 2010*a*) and result are well within the same order of magnitude for both invariants.

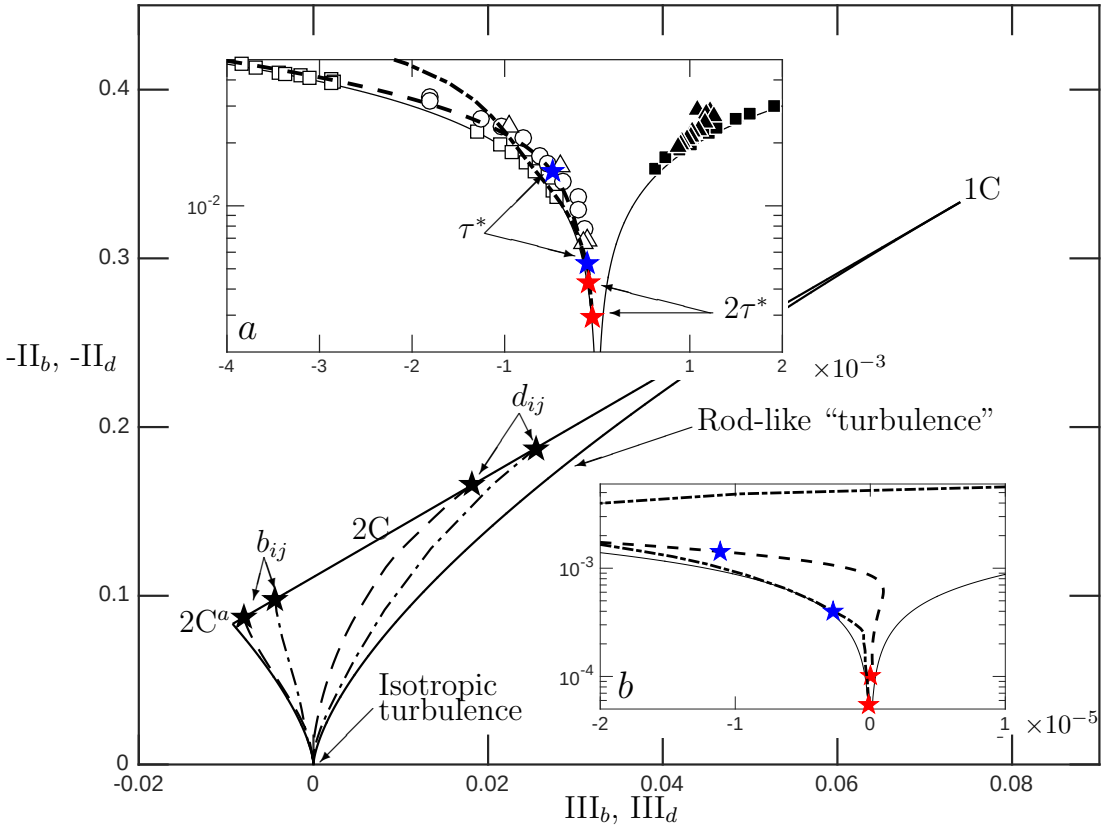

Figure III.5. Lumley triangle for the Reynolds stress (b_{ij}) anisotropy tensor and for the rate of dissipation (d_{ij}) anisotropy tensor. Trajectories for two simulations with $R_I \sim 430$ (dash) and $R_I \sim 573$ (dash-dot) are shown. Time evolution is represented by stars, color labeled as $t = 0$ (black), τ^* (blue) and $2\tau^*$ (red). Inset a) shows the trajectories for the Reynolds stress anisotropy tensors close to the isotropic conditions. Included are the data of Choi & Lumley (2001) (squares, open symbols: asymmetric contraction, closed: asymmetric expansion), Le Penven *et al.* (1985) (triangles, open symbols: $III < 0$ and closed: $III > 0$), and Tucker & Reynolds (1968) (circles). Inset b) shows the trajectories for the dissipation anisotropy tensor. 1C: one component "turbulence", 2C: two component "turbulence", 2C^a: two component axis symmetric "turbulence".

A more detailed analysis of return to isotropy that reflects the behavior of the range of scales present in the flow can be done if anisotropic metrics are defined in wavenumber space. Anisotropy can then be evaluated for individual wavenumbers representative of different scales of motion. While in the most general case the velocity spectrum tensor E_{ij} will depend on the wavenumber vector $\mathbf{k}$, one can also integrate the spectrum over spherical shells of radius k. The energy spectra has 9 components for each wave number, which can be reduced to 6 due to symmetry. The energy spectra anisotropy tensor is then defined as (Yeung *et al.*, 1995):

$$e_{ij}(k) = \frac{E_{ij}(k)}{2E(k)} - \frac{1}{3}\delta_{ij} \tag{3.8}$$

where $E_{ij}(k_1) = 2\int_{-\infty}^{\infty}\int_{-\infty}^{\infty}\langle u_i(\mathbf{k})^* u_j(\mathbf{k})\rangle \mathrm{d}k_2\mathrm{d}k_3$ and $E(k) = \frac{1}{2}E_{ii}(k)$. Similarly to b_{ij} and d_{ij}, the invariants of e_{ij} $\mathrm{II}(k)_e$ and $\mathrm{III}(k)_e$ measure anisotropy, in this case, in spectral space.

Fig. III.6 shows the second and third invariants for two cases as a function of $k\eta$. At $t = 0$ we see 1C behavior at low and high wavenumbers and a $2C^a$ behavior at intermediate wavenumbers, which as discussed above, can be explained from the particular form of the initial conditions. For $t > 0$ it becomes evident that the smallest scales of motion approach isotropy at a faster rate than the largest scales of motion. Both the second and third invariant decrease in the inertial and beginning of dissipation range. There seems to be an increase in anisotropy in the far dissipation range, but data show this to be due to a transient state towards turbulence, as larger times show a decrease in anisotropy at small scales. If one assumes a power-law scaling in the inertial range for these invariants, then one finds that anisotropy

decays as $k^{-3.5}$ and k^{-5} for the second and third invariants, respectively, in the range $4 \times 10^{-2} \lesssim k\eta \lesssim 4 \times 10^{-1}$.

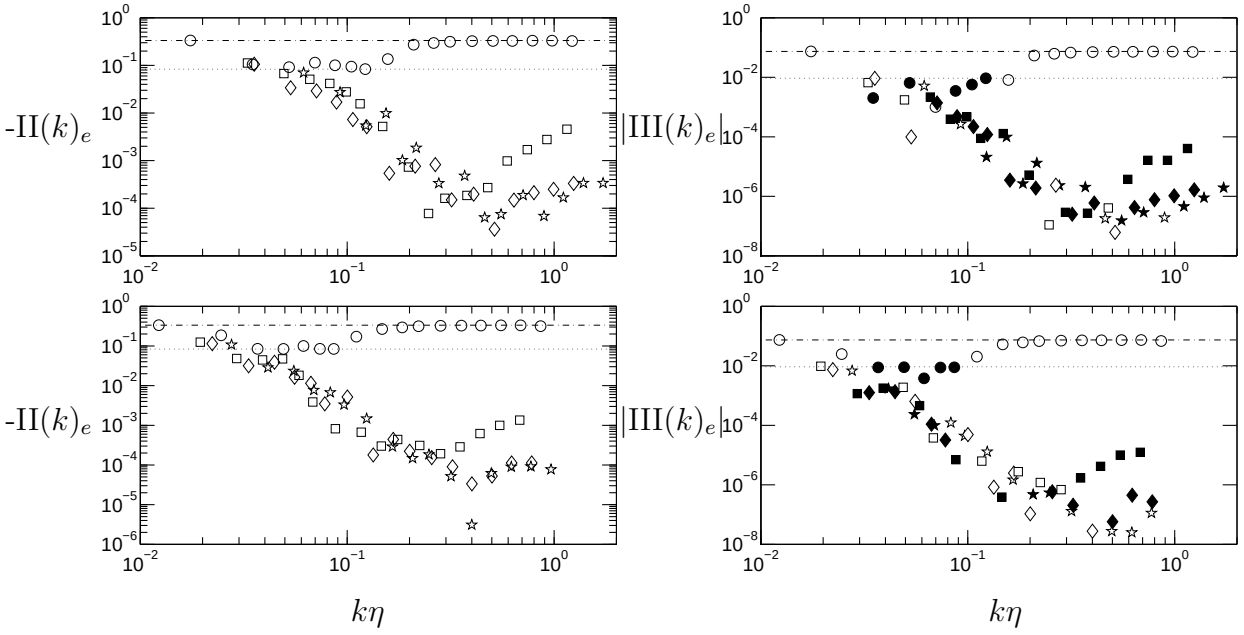

Figure III.6. Second and third invariants for the energy anisotropy tensor as a function of $k\eta$. Circles correspond to $t = 0$, squares are at τ^*, stars $2\tau^*$, and diamonds $3\tau^*$. Open symbols are for positive values of III$_e$, while closed are for negative. Dashed-dot line represents the 1C (one component "turbulence" limit), while dotted line represents 2C^a (two component axis symmetric "turbulence"). Top and bottom rows correspond to cases with $R_I \sim 430$ and 573, respectively.

III.A.1.c. Dependence on initial conditions

As mentioned in the previous sections, the characteristic time scale at the peak of the mean dissipation appears to be related to the onset of turbulence. The question that arises is whether this characteristic time scale can be predicted, and if it can provide the correct information as to when the flow becomes turbulent. The first objective now is to determine whether there is fully developed turbulence by τ^* and

how it depends on initial conditions.

Some initial conditions have a larger degree of (a)symmetry than others due to narrower Gaussians $c_{x,y,z}$ or stronger perturbations κ. Naturally, the time to reach isotropy at all scales will depend on these characteristics. In looking for a non-dimensional parameter that characterizes the initial conditions, it can be argued that important dimensional parameters to be considered are the energy introduced at the lines, the distance between lines, and viscosity. These can easily be used to form a Reynolds number. The amount of energy introduced can be approximated by multiplying the amplitude of the perturbation, κ, by the solidity $\sigma \approx N_l L \pi r_l^2 / L^3$. The solidity is the ratio of volume affected by the LIKES to the total volume in the domain, where $r_l = 2\pi(c_{yz}\log(2))^{1/2}$ is the approximate radius of a line defined using full width at half maximum, $L = 2\pi$ is the length of a line and L^3 is the volume of the domain. Taking the distance between LIKES $d_l = L/N_l^{1/2}$ as the length scale and the fluid viscosity ν, the Reynolds number based on the initial conditions becomes:

$$R_I = \frac{\kappa \sigma d_l}{\nu} = \alpha \frac{\kappa c_{yz} N_l^{1/2}}{\nu} \tag{3.9}$$

where $\alpha = \log(4)\pi^2$. From plots for the skewness of the velocity gradient and the ratio of mean squared velocities with respect to R_I in Fig. III.7, it is evident that the onset of turbulence is related to both τ^* and R_I. Longer times and higher R_I will both make the flow more isotropic. Intuitively one may argue that the initial perturbations must be strong enough to generate a turbulent flow. Indeed the data show that there is a minimum R_I under which turbulence will not be generated regardless of how long the flow is allowed to evolve. As R_I is increased, the flow properties tend to those of fully developed isotropic turbulence, with skewness of

-0.5 and ratio of rms velocities close to 1. However, only after a certain time it can be said that for sufficiently high R_I the flow becomes turbulent. As discussed in previous sections, even though τ^* is typically sufficient time for most quantities to show the properties of a turbulent flow, some variables such as S_{u_x} approaches its fully turbulent value (≈ -0.5) at a slightly slower rate than the other two velocity gradients (Fig. III.8b) and τ^* may not be considered sufficiently long. Therefore, for practical purposes $2\tau^*$ will be considered as the time scale required for the quantities studied here to reach the values of fully developed turbulence, given a minimum R_I is satisfied. In other words there will be a minimum R_I required for $2\tau^*$ to be a good indicator of when the flow becomes turbulent. Indeed, three regimes can be identified based on R_I:

1 $R_I > 400$: turbulence established at $t \approx 2\tau^*$

2 $R_I < 100$: turbulence is not established

3 $100 \lesssim R_I \lesssim 400$: transition where $2\tau^*$ is too short to attain realistic turbulence

Lets consider high R_I cases. As seen in Fig. III.7, the ratio of w'/u' becomes 1 at approximately τ^*, while v'/w' and v'/u' asymptote at a lower value of approximately 0.85. Even though the ratio of longitudinal to transverse velocities does not go to one, this is expected for this type of initial conditions. This could be compared to using active rods or jets to generate turbulence. As reported by Gad-el Hak & Corrsin (1974) for their experiments with parallel rods, u' and w' were of comparable order (within 5%) and approximately 15% larger than v'. This inhomogeneity has long been known (Corrsin, 1963; Comte-Bellot & Corrsin, 1966) and seems unavoidable,

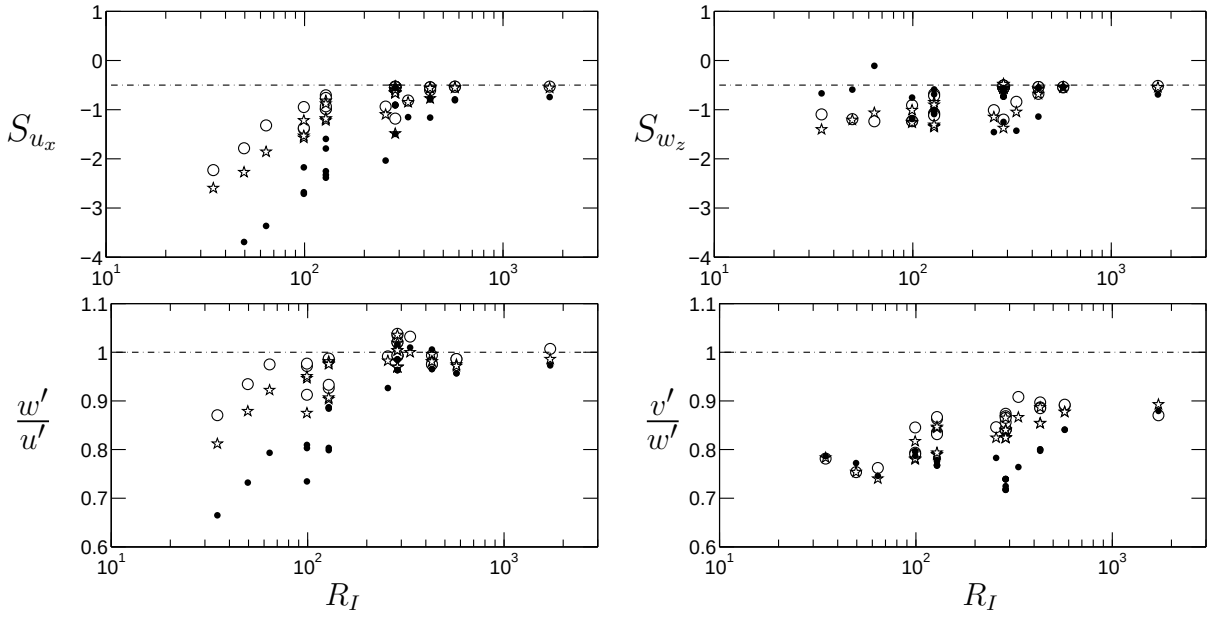

Figure III.7. Skewness of the velocity gradients (top), and ratio of root mean squared velocities (bottom) as a function of R_I. The different markers correspond to: $t = \tau^*$ (dots), $t = 2\tau^*$ (stars), and $t = 3\tau^*$ (open circles). Dashed-dot lines at -0.5 for top plots and 1 for bottom plots.

especially close to the grid. The skewness of the velocity gradient asymptotes at approximately -0.5 for all three components. The first component to reach -0.5 is S_{v_y}. This is the velocity component that, because of zero initial condition, evolves according to Navier-Stokes dynamics acquiring energy from the other components of velocity.

The degree of isotropy at small scales, while expected to be attained earlier than at large scales, would also depend on the characteristics of the initial conditions. A common way to assess small-scale isotropy is by comparing statistics of velocity gradients in different directions. For example, for isotropic turbulence the ratio of the variances of transverse and longitudinal gradients can be shown to be (Hinze, 1959) 2.0. Fig. III.8 shows two simulations that meet the criterion for reaching

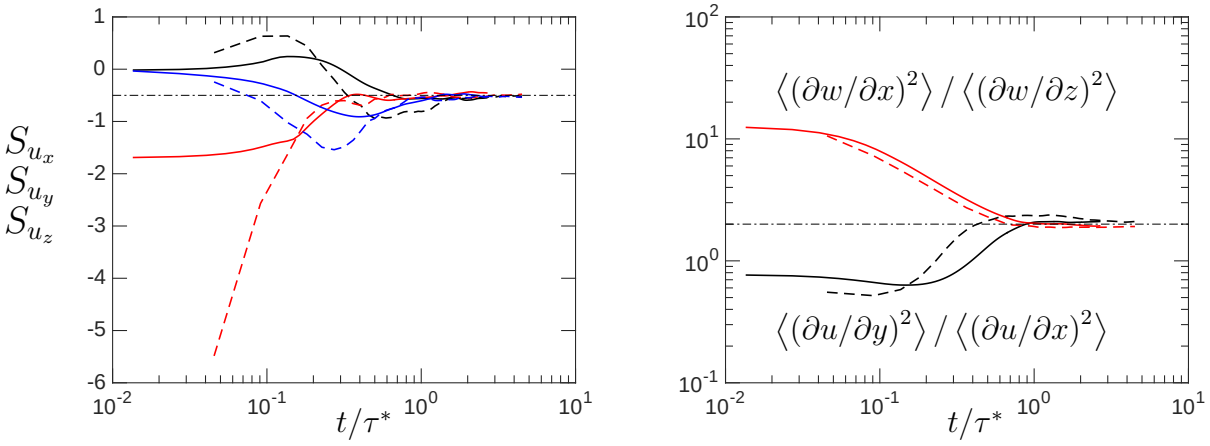

Figure III.8. Skewness of velocity gradients (left) and ratio of transverse to longitudinal second order moments of velocity (right) for two simulations with with $R_I \sim 430$ (solid) and $R_I \sim 573$ (dashed). Colors for left figure correspond to S_{u_x} (black), S_{v_y} (red), and S_{w_z} (blue). Colors for right figure correspond to $\langle(\partial w/\partial x)^2\rangle / \langle(\partial w/\partial z)^2\rangle$ (red) and $\langle(\partial u/\partial y)^2\rangle / \langle(\partial u/\partial x)^2\rangle$ (black).

turbulence at $2\tau^*$ with R_I of ~ 430 and 573. The ratio of transverse to longitudinal velocity gradients approach the corresponding isotropic value of 2.0 at or before τ^*. The figure also shows that the skewness of all three components of longitudinal velocity gradients asymptote around -0.5 at approximately τ^*. In summary, we found that, provided $R_I \gtrsim 400$, the variance of velocity gradients as well as their skewness already approach values found in fully developed turbulence at $t \lesssim 2\tau^*$.

III.A.1.d. Scaling of Characteristic Time Scales

We just saw that a sufficiently high R_I leads to the successful establishment of fully developed turbulence at $t \lesssim 2\tau^*$. Of obvious interest then is to understand the scaling of τ^* to quantitatively estimate, based on all the information from the initial conditions when the flow becomes turbulent. A number of non-dimensional

parameters can be constructed based on initial conditions. Introducing energy in the form of LIKES implies very localized source of energy concentrated along narrow filaments. Therefore, it is expected that the initial evolution of the flow will depend strongly on the energy and local characteristics of the LIKES. In particular one can argue that a set of relevant parameters determining the scaling of τ^*, would include the energy deposited in the LIKES ($K_I = \kappa^2\sigma$), the distance between the LIKES, d_l and the viscosity. Dimensional analysis would then suggest:

$$\tau^* = \frac{\nu}{K_I} f(R_I) \tag{3.10}$$

where f is an unknown function. In Fig. III.9 we show all our database normalized according to Eq. (3.10). It can be seen that this relationship collapses all simulations with different N_l, $c_{yz,x}$, viscosity, and initial perturbation. It is also observed that the function f can be well represented by a power law close to 3/2 obtained as a best fit.

It is also of practical interest to be able to predict, for a given initial condition, the Reynolds number achievable when the flow becomes fully turbulent, that is, at $t \sim \tau^*$. In Fig. III.10a, we show precisely the Taylor Reynolds number at τ^* as a function of R_I. As expected the achievable Reynolds number increases with the initial Reynolds number, though as a weak power law. Also of interest is the relation between τ^* and R_I^* which is shown in Fig. III.10b. This relation, which may follow approximately a power law, implies that achieving high Reynolds numbers may require longer times. This could present some challenges in experiments, especially at high speeds, where the finite length of a wind tunnel may preclude the flow from becoming fully turbulent in the test section at high Reynolds numbers.

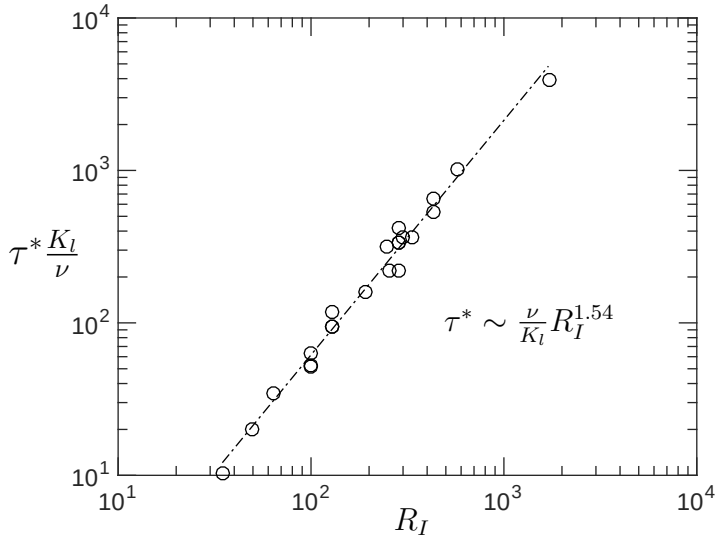

Figure III.9. Scaling of R_I vs. normalized τ^*. All cases from Table II.1 included with dash-dot line for least squares fit of data. Power of R_I based on least squares fit.

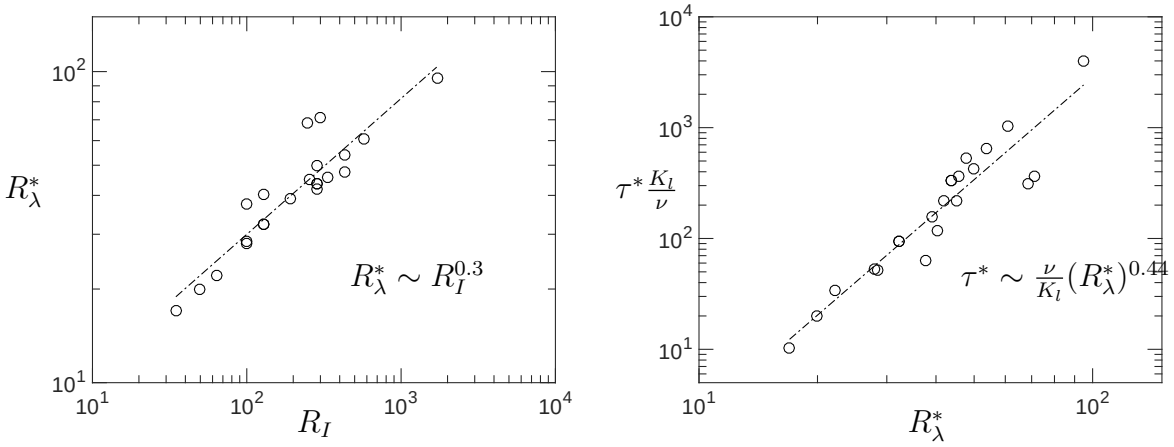

Figure III.10. Normalized time scale $\tau^* K_l/\nu$ versus R_λ on the left, and R_I versus R_λ on the right. Both plots include all simulations in from Table II.1 with dash-dot lines for least squares fit of data. Power of R_I and R_λ^* for left and right plots respectively based on least squares fit.

III.A.2. Acceleration statistics

In previous sections we have shown that turbulence can be established from LIKES as long as the initial Reynolds number is sufficiently high, and sufficient time

has passed as measured by τ^*. In this and the next few sections we focus on the physical mechanisms leading to turbulence.

The main objective of this section is to assess what components play a major role in dispersing the energy introduced in the LIKES. For this we write the Navier-Stokes equations as:

$$\frac{\partial u_i}{\partial t} + a_C = a_P + a_V \tag{3.11}$$

where a_C, a_P, and a_V correspond to the convective, pressure, and viscous components of acceleration respectively. For fully developed turbulence, the variance of the pressure term should be of comparable magnitude or smaller than that of the convective term (Lin, 1987), while the viscous term will be smaller than both by an order of magnitude or more (Vedula & Yeung, 1999).

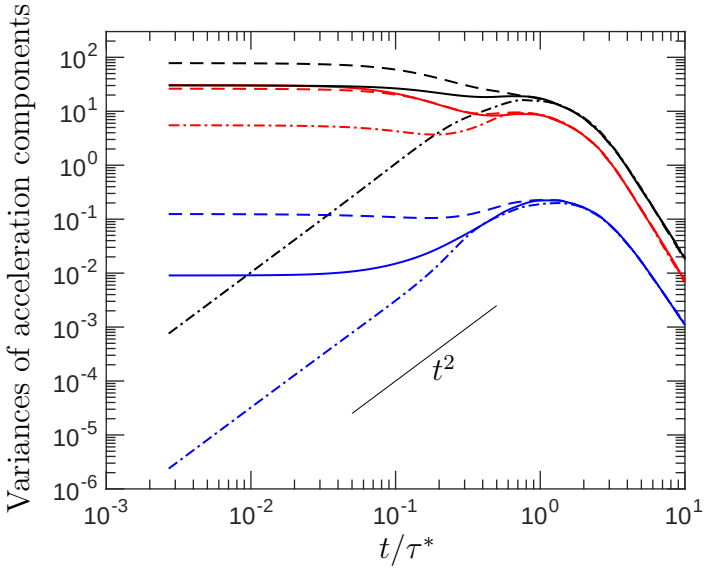

Figure III.11. Variance for the three components of acceleration for case 12 from Table II.1 with $R_I \sim 573$. Convective acceleration (black), pressure acceleration (red) and viscous acceleration (blue). The different lines styles correspond to the x (solid), y (dash-dot), and z (dashed) components.

The time evolution of these three terms is shown in Fig. III.11. At τ^* we see the variance of a_P and a_C are of comparable magnitude, while the viscous term is about an order of magnitude smaller. The ratio of variance of pressure to viscous acceleration scales with (Vedula & Yeung, 1999) R_λ and takes a value of approximately 40 at τ^* and 22 at $2\tau^*$, with corresponding R_λ of 50 and 37 respectively. At τ^* the ratio is slightly large compared to the values reported in Vedula & Yeung (1999), but matches very well at $2\tau^*$. For any time smaller than τ^*, there is a strong disparity between the axial and transverse components of acceleration. Since there is no initial velocity in the y-component, the only non-zero term in the v component of Eq. (2.1) is $-(1/\rho)\partial p/\partial y$, and is therefore responsible for initializing the spread of momentum in the y direction. If this term is assumed to be relatively constant for short times, the second order moment of velocity and velocity gradients would evolve initially as $\langle v^2 \rangle \sim t^2$, and $\langle (\partial^n v/\partial x_i^n)^2 \rangle \sim t^2$. This helps explain the t^2 behavior seen in Fig. III.11 for the variance of the y-component of the viscous as well as the convective acceleration. The latter can be explained by the fact to be discussed later, that the y-component of the convective terms is dominated by the transverse terms $v\partial u/\partial y$ and $v\partial w/\partial z$. With this rapid increase in the y-component, we see that convection dominates in the three directions by approximately $0.5\tau^*$.

Each component of the convective acceleration comprises three terms, each composed of the product of a velocity and a velocity gradient. The evolution of these terms is shown in Fig. III.12. In an isotropic flow, the variance of the three components of velocity will be similar while the ratio between transverse to longitudinal velocity gradients will tend to 2. Thus, the terms $u\partial u/\partial x$, $v\partial v/\partial y$, and $w\partial w/\partial z$

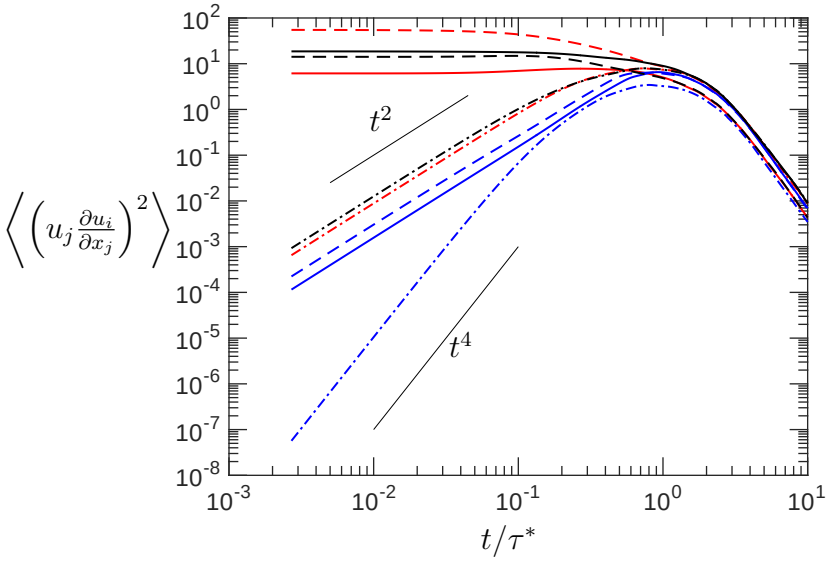

Figure III.12. Components of convective acceleration for case 12 from Table II.1 with $R_I \sim 573$. $u_j \partial u_i / \partial x_j$, j=1 (solid), 2 (dash-dot) and 3 (dash). i=1 (red), 2 (blue) and 3 (black). i.e $w\frac{\partial u}{\partial z}$ (dashed-red), $u\frac{\partial w}{\partial x}$ (solid-black).

will be expected to be approximately half of the other 6 components at sufficiently large time.

The largest term of the convective acceleration is found to be $u\partial w/\partial x$. The initial perturbation, distributed along the LIKES (aligned with the x-axis), is in the w velocity component with random magnitude and direction, providing large gradients in x. The two other terms that dominate initially are $w\partial u/\partial z$ and $w\partial w/\partial z$, again explainable in terms of the form of the initial conditions. All the terms involving the second component of velocity v start from zero. Since, as DNS data show, initially u and w as well as their gradients are approximately constant with respect to time, the variance of the four transverse terms involving v will scale with t^2, while the longitudinal ones will scale as t^4 for short times. This is indeed observed from DNS data in Fig. III.12. The return to isotropy can also be confirmed from this figure as

the six terms with transverse gradients and the three longitudinal gradients collapse for $t \gtrsim 2\,\tau^*$.

In summary, global averages suggest that initially pressure gradients redistribute energy to the velocity component with smallest energy content which grows algebraically until about $t \approx 0.5\tau^*$. After this time convection becomes the dominant mechanism for spreading momentum away from LIKES. For $t \gtrsim 2\,\tau^*$, accelerations in different directions become equal in magnitude.

III.A.3. Local analysis

While global averages provide some information about the dominant forces, they can provide little information about the local behavior of the flow as momentum spreads from LIKES. To understand the mechanisms for turbulence spreading, one can consider radial statistics at different distances from the line. Because of the asymmetry in the perturbation in the plane perpendicular to LIKES, it is convenient to define radial statistics in the y and z directions separately. Thus a radial average of a function f in z, for example, will be denoted by $\langle f \rangle_z$, and is computed by averaging the value of f at all points a distance r_z apart in the z direction from any LIKE in the domain. When the two directions (y and z) are also averaged, we will use simply $\langle f \rangle_r$.

A typical evolution for the radial variance of the w component of velocity in different radial directions is shown in Fig. III.13 for different times. Here, we can see how kinetic energy, which is concentrated at the LIKES spreads to the center as time progresses. One can also see a different response for averages in y and z

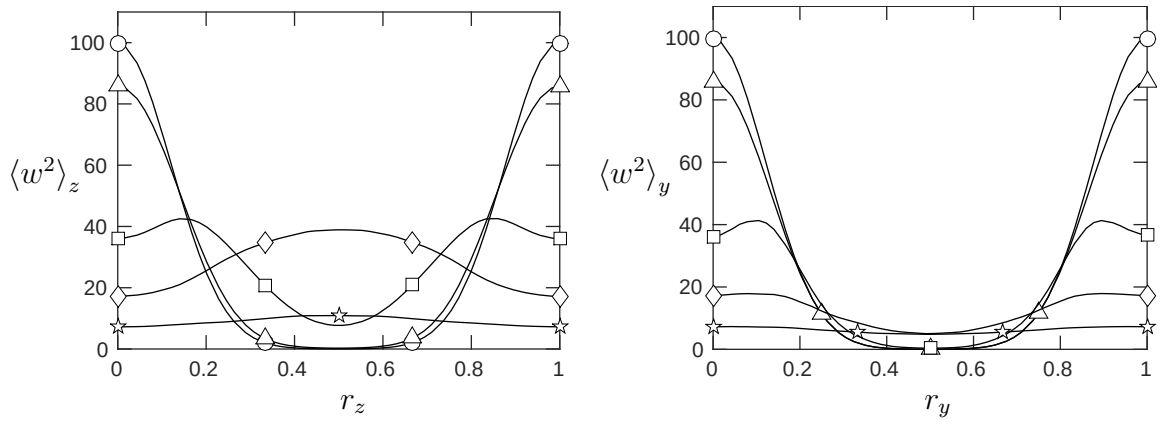

Figure III.13. Initial conditions with $N_l = 4$. Circles correspond to properties calculated at r radial distances away from the line. On the right is the variance w as a function of radial distance along z, and left is the variance of w for radial distances along y. Different symbols correspond to different times $t/\tau^* = 0$ (circle), 0.06 (triangle), 0.29 (square), 1.0 (diamond) and 2.0 (stars).

direction. Since the perturbation is initially preferentially aligned with z direction, and as we showed in the previous section convection is the dominant process in spreading momentum, one would expect, a more rapid spread in the z direction than in the y direction, where the initial velocity is zero.

Two aspects of the flow can be assessed from this type of radial statistics. First, to have isotropic turbulence, one would expect the three components of velocity to be of comparable magnitude at $t \approx 2\tau^*$. Furthermore, for it to be homogeneous, the radial dependence of velocity must also vanish at that time. These expectations can be assessed from Fig. III.13 and Fig. III.14, where we show radial statistics for the three components of velocity for different times.

From Fig. III.14, it becomes clear that both homogeneity and isotropy become progressively better realized with time. Given that the second component of velocity starts from zero, only the pressure gradient term remains in the right-hand-side of the

Navier-Stokes equations in the y direction. As mentioned previously, if the pressure gradient term is assumed to be approximately constant the second order moment of velocity in that direction should evolve as $\langle v^2 \rangle \sim t^2$ for short times. Indeed, this behavior is observed for all radial distances in Fig. III.14b up until $t \approx 0.5\tau^*$.

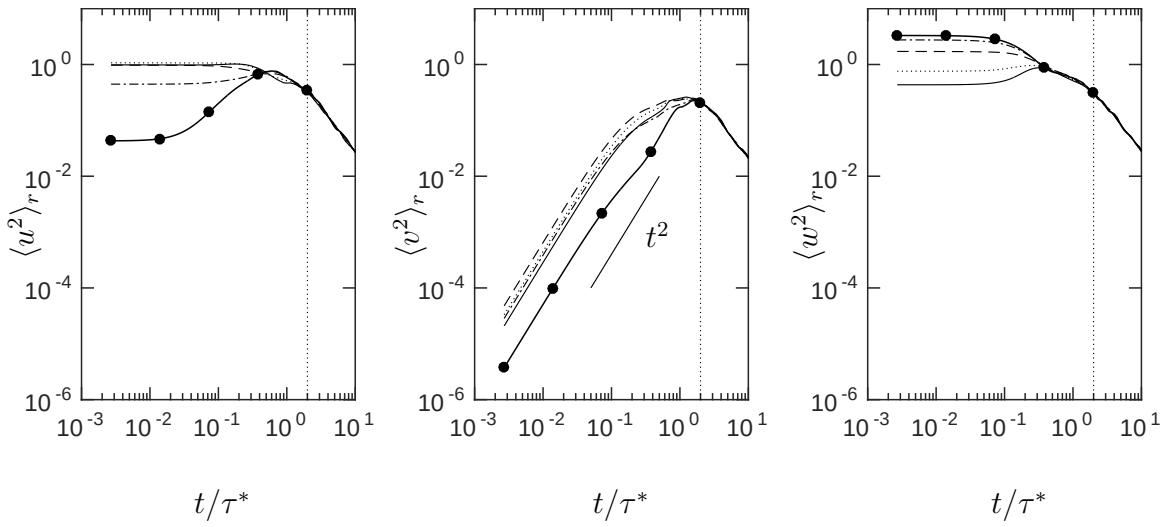

Figure III.14. Evolution of second order moment of velocity as a function of radial distance r. First to third components of velocity from left to right respectively. Different line styles correspond to radial distances with $r \sim 0$ (•), $r \sim 0.12$ (dash-dot), $r \sim 0.24$ (dots), $r \sim 0.36$ (dashed), and $r \sim 0.5$ (solid). Vertical dotted line at $t/\tau^* = 2$ for reference.

Given the importance of the convective acceleration term in the spatial transport of energy away from LIKES, we wish also to investigate radial statistics of velocity gradients. Since the perturbations are Gaussians, it is expected that the gradients of velocity with respect to y and z will be small for $r = 0$. On the other hand, the velocity will change with a random distribution along x, and since the maximum is at $r = 0$, the gradient along this direction is expected to be large. Fig. III.15 shows the variance of the nine components of velocity gradients. By comparing all the

gradients at short times, it is seen that the largest contributions come from $\partial w/\partial x$ and $\partial u/\partial z$. The former is large for the reason previously described. The latter comes from satisfying continuity, as the first component of velocity is generated from $\partial w/\partial z$. The derivative of u with respect to x and y at $r = 0$ is small, as the velocity itself should be small at this location. All gradients involving the y component of velocity start from zero but they reach the magnitude of the other six terms by $t \lesssim 2\tau^*$, as can be seen in Fig. III.15. Also by $2\tau^*$ there is no more radial dependence and all terms decay at the same rate. Here again, the data supports $t/\tau^* \sim 2$ as the nominal time at which the flow becomes fully turbulent.

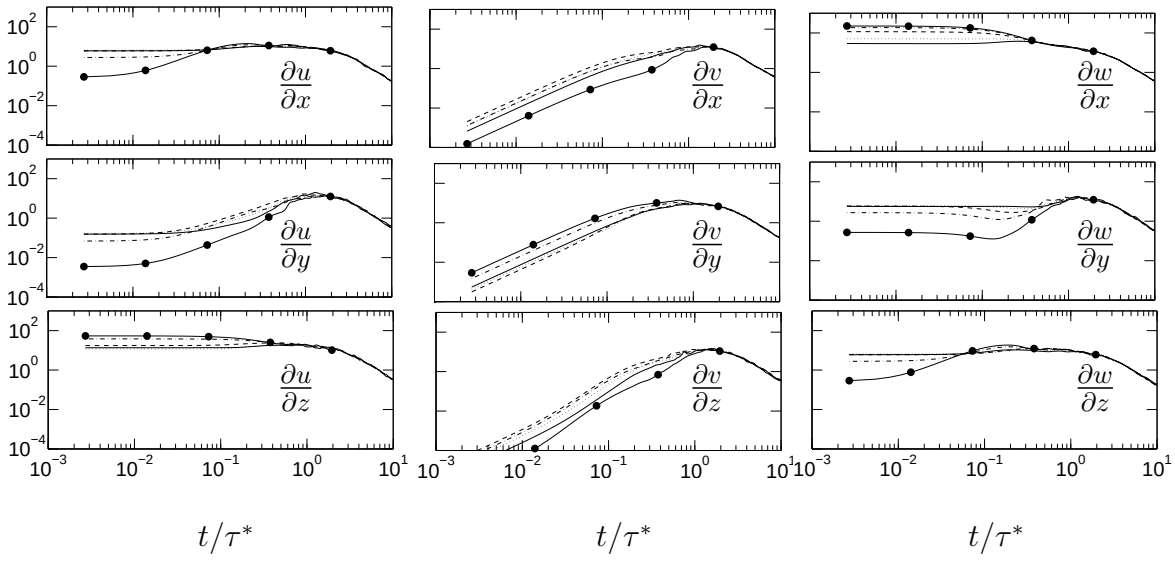

Figure III.15. Variance of velocity gradient as a function of radial distance r. Different linestyles correspond to radial distances with $r \sim 0$ (•), $r \sim 0.12$ (dash-dot), $r \sim 0.24$ (dots), $r \sim 0.36$ (dashed), and $r \sim 0.5$ (solid).

We now focus on how both the velocity and derivatives interact and contribute to the radial moments of convective acceleration. Fig. III.16 shows the evolution for the

sum of all $u_j \partial u_i / \partial x_j$ terms at five different radial distances. Here we find that most components have a larger variance at short distances away from the LIKES, rather than at the center of the LIKES themselves. This can be explained by the trade off between the gradients and the velocity components. We have seen that $\partial w / \partial x$ is the largest term at $r = 0$, but since u is very small (Fig. III.14) $u \partial w / \partial x$ becomes small. The product of velocity and its gradients is also expected to be small at $r = 0.5$ where the imposed symmetry implies very small gradients at a point equidistant to two LIKES. It is thus expected that the largest convective contributions would be observed at an intermediate point between $r = 0$ and $r = 0.5$. Indeed, we see that the largest contribution from convective acceleration is found at $r \sim 1/4$ in Fig. III.16. For $t > 0$, the convective acceleration at $r = 0$ increases fastest while it is relatively constant for other distances, leading it to dominate the spread of momentum at very short times ($t \approx 0.1\tau^*$). For $t \gtrsim 2\tau^*$ we see radial independence and the same rate of decay for all distances, consistent with results for the velocity and velocity gradient profiles.

III.A.4. Enstrophy generation

The equation for the evolution of enstrophy $\omega_i \omega_i$ can provide great insight into the physical processes of turbulent flows. The different terms are related to tilting, folding, stretching as well as dissipation and transport of vorticity which are responsible for the non-linear generation of small scales, the cascade of energy and its dissipation at the smallest scales (Tennekes & Lumley, 1972). The evolution equation for the vorticity can be readily found by taking the curl of the Navier-Stokes

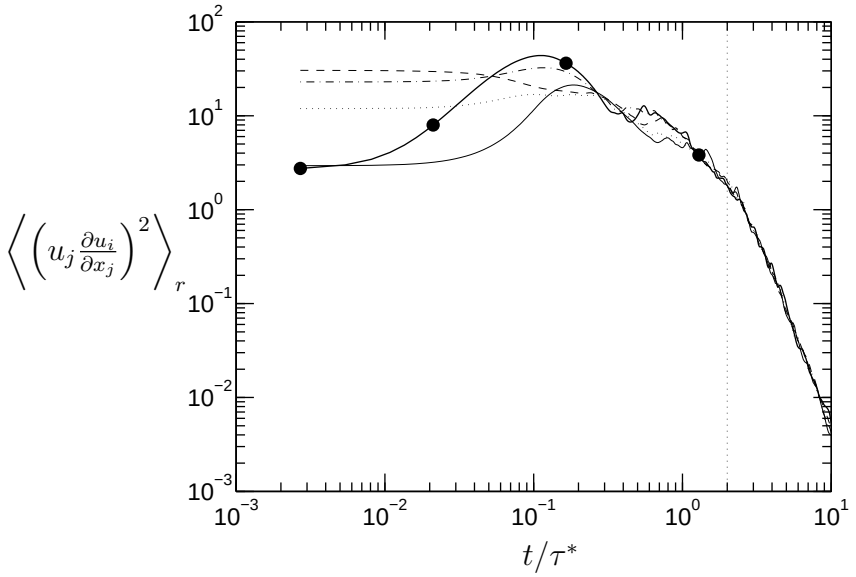

Figure III.16. Convective acceleration (sum of all components) in term of radial averages. $r = 0$ **(•), 0.13 (dash-dot), 0.25 (dash), 0.375 (dotted) and 0.5 (solid).**

equation, Eq. (2.1). Multiplying the result by the vorticity vector, taking spatial averages, and assuming homogeneous and isotropic turbulence, yields the evolution equation of enstrophy (Taylor, 1938):

$$\frac{\partial \langle \omega_i \omega_i \rangle}{\partial t} = 2 \langle \omega_i \omega_j s_{ij} \rangle - 2\nu \left\langle \frac{\partial \omega_i}{\partial x_j} \frac{\partial \omega_i}{\partial x_j} \right\rangle \tag{3.12}$$

where $s_{ij} = 1/2(\partial u_i/\partial x_j + \partial u_j/\partial x_i)$ is the strain rate tensor. The first term on the right hand side represents the production of enstrophy by vortex stretching and the second is the viscous dissipation (101). From Fig. III.17 we see that the two terms reach their minimum and maximum around τ^*. For homogeneous flows, one can show that(101) $\langle \epsilon \rangle = \nu \langle \omega_i \omega_i \rangle$. Thus the peak of the dissipation is also the time of maximum vorticity as can be appreciated from Fig. III.17. For steady state turbulence, it is expected that the two terms on the right hand side of Eq. (3.12) be equal in magnitude but opposite in sign thus canceling each other (Taylor, 1938;

Gorski *et al.*, 1994). However, we are interested in the transient between the LIKES at $t = 0$ and the time where fully developed turbulence is established. At $t = 0$ we can use the fact that $v = 0$ by construction and that, because of continuity, $\partial u/\partial x = -\partial w/\partial z$ to write $w_i w_j s_{ij}$ as:

$$\omega_i \omega_j s_{ij} = \frac{\partial w}{\partial z}\frac{\partial u}{\partial y}\frac{\partial u}{\partial z} + \frac{\partial w}{\partial z}\frac{\partial u}{\partial y}\frac{\partial w}{\partial x} - \left(\frac{\partial w}{\partial z}\right)^2 \frac{\partial w}{\partial y} \tag{3.13}$$

We can observe that $\langle w_i w_j s_{ij} \rangle$ starts from zero but increases as the flow evolves. Due to the random nature of the initial conditions, the gradients of velocity in Eq. (3.13) are uncorrelated with each other. We would then expect the average of the product of velocity gradients to be small, if the average of each independent gradient is small. This can indeed be verified from our DNS data. On the other hand, the viscous dissipation term is not negligible at the initial conditions.

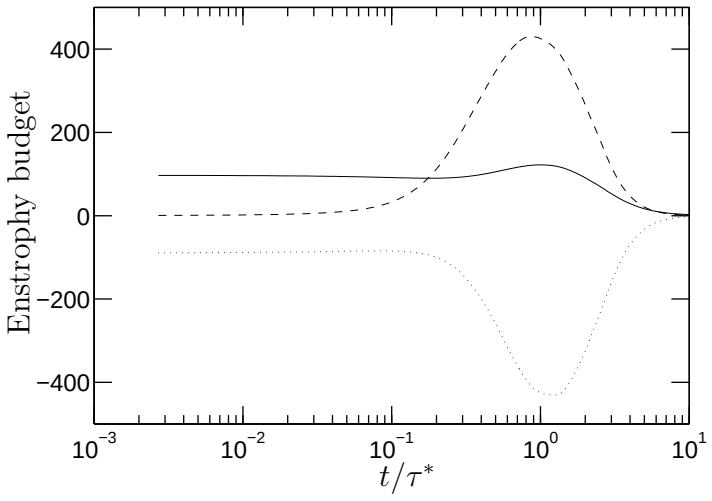

Figure III.17. Enstrophy budget with terms averaged over the domain. Solid line is for evolution of $\langle \omega_i \omega_i \rangle$, dashed for vortex stretching and dotted for viscous dissipation.

As argued above, a local analysis of the flow can be effectively done with radial averages around the LIKES. If we apply radial averages on the enstrophy equation we find:

$$\begin{aligned}\frac{\partial\langle\omega_i\omega_i\rangle_r}{\partial t} &= -\frac{\partial}{\partial x_j}\left(U_j\langle\omega_i\omega_i\rangle_r\right) - \frac{\partial}{\partial x_j}\left(\langle u_j\omega_i\omega_i\rangle_r\right) - 2\langle u_j\omega_i\rangle_r\frac{\partial\Omega_i}{\partial x_j} + 2\langle\omega_i\omega_j\rangle_r S_{ij} \\ &\quad +2\langle\omega_i\omega_j s_{ij}\rangle_r + 2\Omega_j\langle\omega_i s_{ij}\rangle_r + \nu\nabla^2\langle\omega_i\omega_i\rangle_r - 2\nu\left\langle\frac{\partial\omega_i}{\partial x_j}\frac{\partial\omega_i}{\partial x_j}\right\rangle_r \qquad (3.14)\end{aligned}$$

Where upper case (U_i, Ω_i, S_{ij}) denotes radial means at a particular radial distance. While for fully developed homogeneous and isotropic turbulence all mean components as well as gradients of means are expected to be zero, this is not the case at short times in the present configuration. From DNS we find that the terms $\frac{\partial}{\partial x_j}\left(U_j\langle\omega_i\omega_i\rangle_r\right)$, $2\langle u_j\omega_i\rangle_r\frac{\partial\Omega_i}{\partial x_j}$, and $2\Omega_j\langle\omega_i s_{ij}\rangle$ as well as the spatial derivatives of Ω_i and U_i are very small. We also find that the first and third components of Ω are very small compared to the second component for all radial distances. The latter is maximum at $r = 0$ and decreases as r increases. While $\langle\omega_i s_{ij}\rangle$ starts from zero and increases with time, the decrease of Ω_2 makes the sixth term in Eq. (3.14) also small compared to the other terms. Thus, keeping only the dominant terms we may reduce Eq. (3.14) to:

$$\begin{aligned}\frac{\partial\langle\omega_i\omega_i\rangle_r}{\partial t} = -\frac{\partial}{\partial x_j}\left(\langle u_j\omega_i\omega_i\rangle_r\right) + 2\langle\omega_i\omega_j\rangle_r S_{ij} &+ 2\langle\omega_i\omega_j s_{ij}\rangle_r + \nu\nabla^2\langle\omega_i\omega_i\rangle_r \\ &- 2\nu\left\langle\frac{\partial\omega_i}{\partial x_j}\frac{\partial\omega_i}{\partial x_j}\right\rangle_r \qquad (3.15)\end{aligned}$$

The second and third terms correspond to the production of turbulent vorticity from the stretching or squeezing (according to the sign) of the fluctuating and mean strain rates respectively. The first correspond to transport of vorticity from fluctu-

ations of velocity while the last two are the viscous transport and dissipation (101).

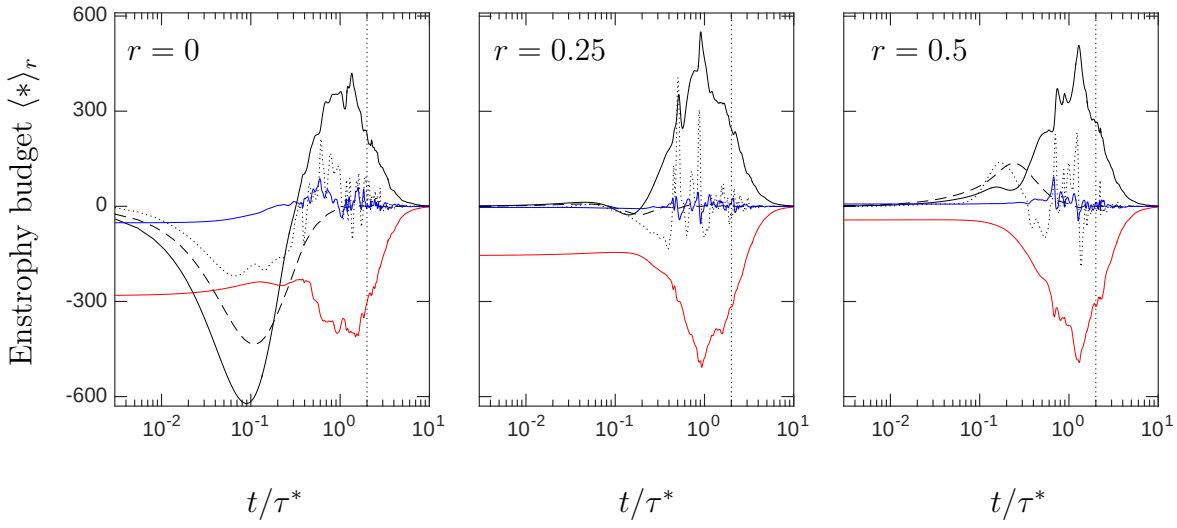

Figure III.18. Enstrophy budget with radial averages for $r = 0$ (left), 0.25 (center), and 0.5 (right). Different line styles correspond to $\frac{\partial}{\partial x_j}(\langle u_j \omega_i \omega_i \rangle_r)$ (dotted), $2\langle \omega_i \omega_j \rangle_r S_{ij}$ (dash), $2\langle \omega_i \omega_j s_{ij} \rangle_r$ (black), $\nu \nabla^2 \langle \omega_i \omega_i \rangle_r$ (blue), and $-2\nu \left\langle \frac{\partial \omega_i}{\partial x_j} \frac{\partial \omega_i}{\partial x_j} \right\rangle_r$ (red). Vertical dotted line for $t = 2\tau^*$.

The evolution of the five terms in Eq. (3.15) is shown in Fig. III.18 at three radial distances, $r = 0$, 0.25 and 0.5. The viscous transport term $\nu \nabla^2 \langle \omega_i \omega_i \rangle_r$ is only present for $r = 0$ and becomes negligible after a short time. The dominating term at $t = 0$ is the viscous dissipation, with strongest influence at $r = 0$. This term peaks at approximately $t \approx \tau^*$, where it also reaches radial homogeneity. The second two largest terms are the (negative) production of turbulent vorticity from the mean and fluctuating strain rates.

To understand why there is negative production (or vortex squeezing) from the mean strain rate, one needs to consider the mean of velocity gradients in terms of

radial distances. The mean of the nine components of velocity gradients at different radial distances are shown in Fig. III.19. Only four components are non zero between the initial conditions and $t \approx 0.5\tau^*$. These are the longitudinal $\partial v/\partial y$, $\partial w/\partial z$ and the transverse gradients $\partial u/\partial z$, $\partial w/\partial x$. The longitudinal components are the dominating terms, yet the change in sign at different radial distances provide a significant amount of cancellation. On the other hand, there is a net negative contribution from the transverse components. We can then conclude that the large vortex squeezing at $t = 0$ comes mainly from $\partial w/\partial x$ and $\partial u/\partial z$. The former corresponds to non-uniformities in the w component along the LIKES (in x) and the latter to the changes in the perturbations in the direction of the LIKES as one moves away from them.

There is also vortex squeezing from the fluctuating strain rate. Not surprisingly this term is dominant at the location of the LIKES for short times. At approximately $t \approx 0.5\tau^*$, there is a qualitative change in behavior from vortex squeezing to stretching. The term $\langle \omega_i \omega_j s_{ij} \rangle$ sees a maximum at approximately τ^*, where radial dependence begins to vanish. By $t \approx 2\tau^*$ the vortex stretching due to the fluctuating strain rate is roughly equal and opposite to the dissipation of vorticity. After the flow reorganizes itself to a turbulent state, these are the principal mechanism for the creation and destruction of vorticity, respectively.

Another interesting observation is that $-\frac{\partial}{\partial x_j}\left(\langle u_j \omega_i \omega_i \rangle\right)$ has large negative values at $r = 0$, up until approximately τ^*. Since this is a transport term and it is negative, it implies that enstrophy is being transported outwards as time evolves. As the flow starts mixing this term has large fluctuations but becomes small beyond

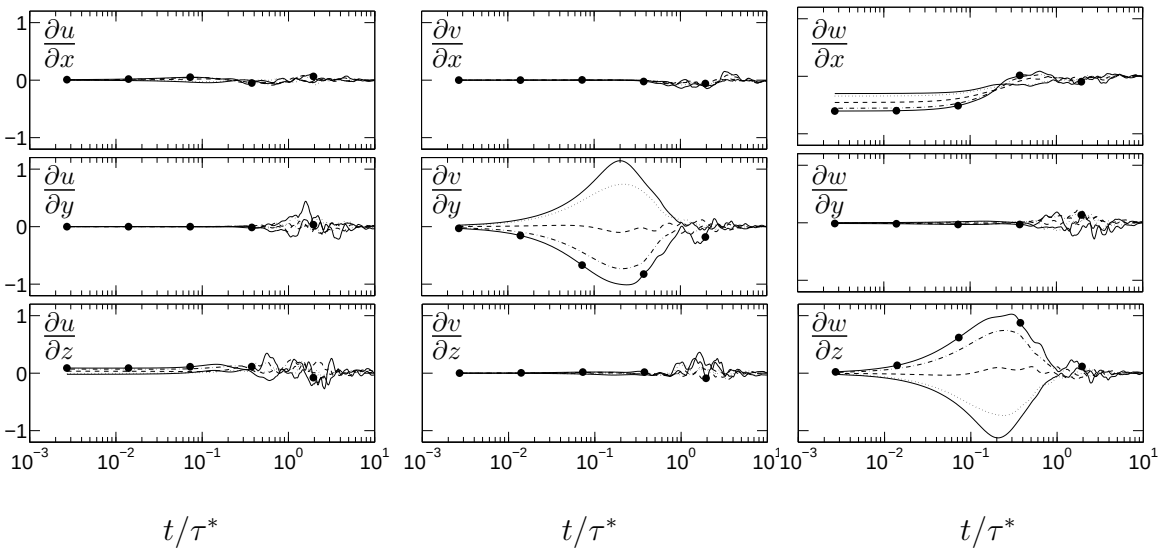

Figure III.19. Mean of velocity gradient as a function time for different radial distances r. Different line styles correspond to radial distances with $r \sim 0$ (•), $r \sim 0.12$ (dash-dot), $r \sim 0.24$ (dots), $r \sim 0.36$ (dashed), and $r \sim 0.5$ (solid).

$2\tau^*$. Then, consistent with all the previous observations, all the terms show radial independence by $2\tau^*$ and the two terms that dominate are the vortex stretching and viscous dissipation.

III.B. Conclusions

We have investigated the generation of turbulence using localized intense kinetic energy sources, or LIKES. We have found that LIKES are a feasible mechanism for generating turbulence given two conditions are met: a Reynolds number based on initial conditions is sufficiently high ($R_I > 400$) and that enough time has elapsed for the flow to reorganized into a fully turbulent state ($t > 2\tau^*$). The characteristic time scale τ^* is a well defined time scale of the problem easily identified as the time when the mean dissipation (or enstrophy) is maximum. This characteristic time scale,

as well as other characteristics of the flow, were shown to be expressible in terms of a single non-dimensional parameter (a Reynolds number) based on the initial conditions, in particular the magnitude of velocity perturbation, the grid solidity, the fluid viscosity, and the distance between the LIKES as the length scale.

The LIKES are implemented as a sum of Gaussians with random amplitude and phases with a preferential direction, justified from experimental observations of the photo-dissociation process (North & Hall, 1997; North *et al.*, 1997; Houston, 1987). From detailed convergence studies we found that two conditions, one kinematic and one dynamic, must be met to obtain grid converged solutions. This led to two non-dimensional parameters (G and R_k) that can be determined a priori from initial conditions. The final resolution criteria were found to be given by $G > G_{\min} \approx 5$ and $R_k < R_k^{\max} \approx 10$. Several statistics were used to understand the flow transition to fully developed turbulence in terms of time and R_I. For $R_I > 400$ and $t > 2\tau^*$, it is shown that the skewness of velocity gradient becomes -0.5 while the ratio of rms velocities approaches unity, consistent with homogeneous isotropic turbulence (Tavoularis *et al.*, 1978; Sreenivasan & Antonia, 1997). At these conditions, the spectra collapses under K41 normalization and isotropic relations based on longitudinal to transverse components of the energy spectra are satisfied. The anisotropy tensors for turbulent kinetic energy and dissipation are also shown to be consistent with DNS of isotropic turbulence.

In general, the second and third invariants of b_{ij} and d_{ij} approach zero as R_I and time are increased. For $R_I > 400$ and $t \approx 2\tau^*$, these are comparable to grid generated turbulence at similar Reynolds number (Choi & Lumley, 2001; Le Penven *et al.*, 1985;

Tucker & Reynolds, 1968). For shorter times, as the flow evolves we do not observe a linear relation as in e.g. Refs. (1; 67). However, this is not surprising given the significant differences in the initial conditions. The flow generated from LIKES is found to present similarities with grid turbulence passed through a contraction where, as several authors have shown (Choi & Lumley, 2001; Le Penven *et al.*, 1985; Tucker & Reynolds, 1968), there is no linear relationship between the b_{ij} and d_{ij} tensors. An anisotropy tensor in wavenumber space was used to show that small scales approach isotropy at a faster rate than the large scales.

An important result from the analysis above is the relation found for both τ^* and R_λ with the initial conditions Reynolds number R_I. In particular, these have been shown to scale as $\tau^* \sim R_I^{1.54}$ and $R_\lambda \sim R_I^{0.3}$. It is worth noting that increasing R_λ requires longer times to observe fully developed turbulence. This result is crucial for the design of wind tunnels that will use the proposed method to generate turbulence. Since the time scale can be converted to distance using a suitably defined convective velocity, this can also provide estimates for the highest R_λ that can be attained when faced with spatial restrictions.

To understand the main mechanisms governing the spread of concentrated kinetic energy of the LIKES, we studied accelerations statistics. The convective acceleration $u_j \partial u_i / \partial u_j$ dominates the spread of energy and pressure redistributes energy from the x and z components to the y component through $\partial p / \partial y$ which dominates initially. At $t/\tau^* \approx 2$, all directional information is lost and acceleration statistics become isotropic.

Local statistics of the flow were studied to further understand the mechanisms

for redistribution of energy. Radial averages demonstrated that convection dominates initially in the proximity of the LIKES. Vortex squeezing due to the fluctuating and mean strain rates at the LIKES ($r = 0$) was found to be strong for short times. $\langle \omega_i \omega_j S_{ij} \rangle_{r=0}$ vanishes at $t \approx \tau^*$, while $\langle \omega_i \omega_j s_{ij} \rangle_{r=0}$ sees a qualitative change from squeezing to stretching at $\tau^*/2$. Viscous dissipation is seen at most radial distances but primarily dominates at $r = 0$. Consistent with a homogeneous flow, the peak of the dissipation is also the time of maximum vorticity and vortex stretching and viscous dissipation become equal in magnitude and opposite in sign at $t \approx 2\tau^*$.

In summary, we have shown that it is possible to create turbulence based on localized intense kinetic energy sources provided a well-defined Reynolds number based on initial conditions is high enough. We have also shown that it is possible to predict the achievable R_λ as well as when the transition to turbulence occurs, using a single non-dimensional parameter based on initial conditions.

CHAPTER IV

TURBULENCE GENERATION IN COMPRESSIBLE FLOWS

In the previous chapter we have shown results from incompressible lines to study the hydrodynamics of the general problem: generating turbulence with localized sources or energy. While it provided insight into the main mechanisms leading to the generation of turbulence at a relatively low computational cost, we are now interested in understanding the more general and realistic problem. We now replicate the physical wind tunnel experiment more faithfully by including compressibility and temperature effects. Compressible simulations capture both hydrodynamics and thermodynamics of the practical problem and DNS parameters can be adjusted to simulate the test conditions. The next step in complexity would be to incorporate the effects of TNE in the evolution of the flow.

IV.A. Spreading of perturbations from single LICES

Understanding the evolution of the flow behind LICES is a very complex problem which depends on a large number of parameters. A variable of obvious interest if turbulence is sought is the rate at which perturbations spread. It is expected that if perturbations spread at a large rate, turbulent mixing will be favored. However, having strong interactions between thermodynamic and hydrodynamic variables it is hard to predict how the perturbations will spread. The following section is devoted to characterizing the leading mechanisms in the rate of spread.

IV.A.1. Numerical computation of perturbation spread

To understand how the perturbations of velocity spread downstream, the problem is simplified to a single LICES on the $x - z$ plane aligned with x, as shown in Fig. IV.1. A flow with convective Mach number $M_c = 5$ ($u_2 = 720.7$, $T_0 = 50$) displaces the perturbations from the LICES downstream along the second component. To measure how the velocity perturbations spread downstream, we define a width δ. This width is defined as the distance along z, starting from the center of the LICES, at which the kinetic energy decays to 1% of the introduced kinetic energy at the LICES. A graphical representation of δ can be seen inFig. IV.1 (right).

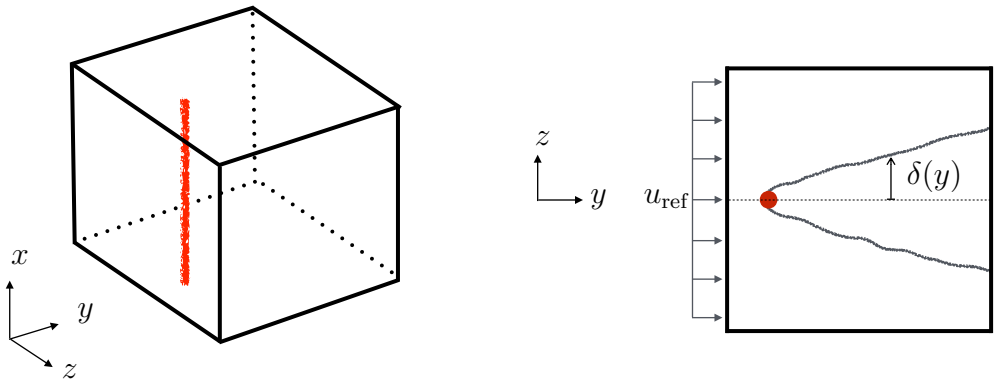

Figure IV.1. Schematic of configuration used for measuring spread of perturbations. Domain is $(2\pi)^3$ with LICES located at $z = 0, y = \pi/4$. a) three dimensional perspective, b) top view.

Given the flow is supersonic, the perturbations introduced create Mach waves at an angle of $\sin^{-1}(1/M_c)$ behind the LICES. This introduces non turbulent velocity perturbations that affect the spread measurements and must be removed prior to computing δ. The velocity perturbations from the Mach waves are stationary in time, so we may easily remove these by subtracting the time averaged velocity field.

For statistical convergence, a total of 50 different times are averaged for each set of conditions. Throughout the chapter angular brackets are used for spatial averages while an overbar is used for time averages. From this point, all quantities shown are time averages, so for simplicity of the notation the overbar will be dropped.

We then define δ as:

$$\delta(x,y,t) = \sum_{z=N_z/2}^{N_z} \begin{cases} \Delta z, & \text{if } \dfrac{\frac{1}{2}\left((u_1-\overline{u_1})^2+(u_2-\overline{u_2})^2+(u_3-\overline{u_3})^2\right)}{\langle \Delta K \rangle_l} > 1\% \\ 0, & \text{otherwise} \end{cases} \tag{4.1}$$

where Δz is the grid spacing along z, u_i and $\overline{u_i}$ are both functions of x, y, z and $\langle \Delta K \rangle_l = \left\langle \frac{1}{2}\left((u_1-u_{\mathrm{ref}_1})^2+(u_2-u_{\mathrm{ref}_2})^2+(u_3-u_{\mathrm{ref}_3})^2\right)\right\rangle_l$ is the averaged additional kinetic energy introduced by the LICES. In this configuration the center of the LICES is at half of the domain along z and consequently the sum starts from $N_z/2$. With Eq. (4.1) we compute δ for every $y-z$ plane at time t. We then average all planes and times such that δ becomes a function of only y.

To understand the effect of fluid and thermodynamic variables on the spreading rate, we created a large database with different velocities, temperatures, and $\kappa_{\max}$. All the simulations have been tabulated in Table IV.1.

IV.A.2. Spreading rate

In Fig. IV.2 we can see $\delta(y)$ for different velocity and temperature perturbations. The clear peaks we see for small y correspond to each LICES. For $u_{\mathrm{ref}} = 720.7$ and $H_f = 2000$, a LICES is convected a distance of $y_c \sim 0.36$ before the next is implemented. For small velocity perturbations, there seems to be a strong effect

Case	N_l	u_m	T_m	$\kappa_{\max}$	u_l	T_l	$\langle\nu_l\rangle$	H_f	N	R_l
1 - 6	1	1	1 - 20	2 - 12	0.35	0.40 - 8.05	0.40 - 0.43	2000	128^3	0.31
7 - 12	1	5	1 - 20	2 - 12	1.76	0.40 - 8.05	0.40 - 0.43	2000	128^3	1.55
13 - 18	1	10	1 - 20	2 - 12	3.52	0.40 - 8.05	0.40 - 0.43	2000	128^3	3.09
19 - 24	1	20	1 - 20	2 - 12	7.05	0.40 - 8.05	0.40 - 0.43	2000	128^3	6.18
25 - 30	1	50	1 - 20	2 - 12	17.61	0.40 - 8.05	0.40 - 0.43	2000	128^3	15.45
31 - 36	1	100	1 - 20	2 - 12	35.23	0.40 - 8.05	0.40 - 0.43	2000	128^3	30.90

Table IV.1. All simulations used to measure the rate of spread δ as a function of streamwise distance y. The cases grouped together contain two $\kappa_{\max}$ with three temperatures each. They are ordered as case 1-3: $T_m = 1, 10, 20$ with $\kappa_{\max} = 2$, and 4-6 with same temperature and $\kappa_{\max} = 12$. Similarly for rest of cases grouped.

of temperature on the spreading of perturbations, with low temperature having the largest δ. As the velocity perturbations are increased, the effect of temperature weakens. This is evident for $u_m = 10$ where it becomes difficult to distinguish between the different temperatures. Increasing the amplitude of velocity perturbations even further we see a reversed trend, where high temperature has the largest δ. The amount of kinetic and internal energy we introduce seems to play a critical role in the spreading rate. If we wish to define a non-dimensional parameter to quantify the amount of energy we introduced as a function of the energy in the flow, we may do so as:

$$Q = \frac{\Delta K_\rho + \Delta E}{K_\rho + E} \tag{4.2}$$

where $K_\rho = \rho K$, $E = \rho e$, and Δ corresponds to the difference between the evaluated quantity and the reference value.

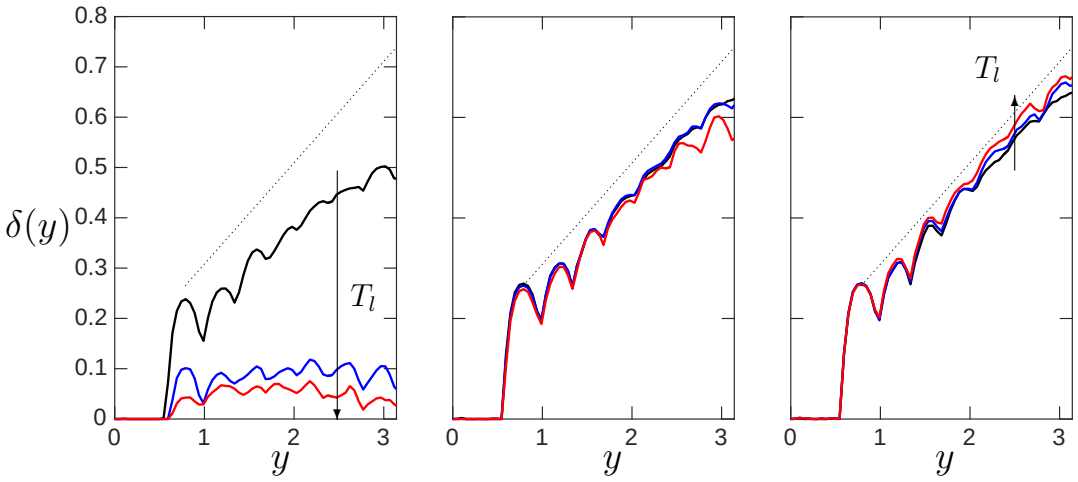

Figure IV.2. Spreading of perturbations δ as a function of y for different velocity and temperature. From left to right is increasing velocity $u_m = 1$ (left), 10 (center), 100 (right). Different colors correspond to $T_m = 1$ (black), 10 (blue), and 20 (red). These correspond to Case 4,5,6 (left), 13,14,15 (center) and 31,32,33 (right) of Table IV.1. Dotted line corresponds to a Mach wave with $M_c = 5$.

We may also quantify the energy we introduce to the system in terms of velocity and internal energy in the form of a Reynolds number. Based on the velocity and temperature perturbations introduced at the LICES, we can define a Reynolds number as:

$$R_l = \frac{\langle (\Delta K)^{1/2} \rangle_l \, \sigma \, d_l}{\langle \nu \rangle_l} \tag{4.3}$$

where σ represents the solidity of the grid defined as $\sigma = N_l L \pi r_l^2 / (L^2 L_y)$. L is the transverse length of the domain (x or z), L_y the axial length, and r_l is the radius of a LICES. The radius r_l is defined as the width where the velocity or temperature is 10% of the maxium, u_m or T_m, which may be numerically obtained solving for x in Eq. (2.14) with $\alpha = \alpha_m \times 10^{-1}$. Finally, the length scale is the distance between LICES: $d_l = L/N_l$ (if we have LICES in more than one component then $d_l = L/n_x$,

with $n_x = n_z$). For computing the spreading rate, the transverse length of the domain is used for d_l, as there is only one LICES.

As seen in Fig. IV.2, the width δ undergoes approximately a linear growth in space consistent with self-similar solution from jets (Tennekes & Lumley, 1972). Thus one can quantify the rate with $d\delta/dy$. In Fig. IV.3 we show the time averaged rate of spread with respect to R_l and Q for all the simulations in Table IV.1. The first observation we can make is that R_l collapses the data for spreading rate while Q does not. It will also be shown in future sections that R_l is a suitable parameter to describe the evolution of the flow. With this in mind, we continue our analysis in terms of R_l. At low R_l there is a strong dependence on T_l, where the increased local viscosity from the additional temperature mitigates the spread of perturbations. The effect of temperature decreases with increasing R_l and appears to be independent at approximately $R_l = 3 \times 10^{-1}$. After this point, although weaker, the effect of temperature returns with a reverse trend where large temperature increases $d\delta/dy$. As R_l is increased, the rate of spread asymptotes at the convective Mach angle, represented by the horizontal dotted line in Fig. IV.3. The velocity perturbations appear to be confined within the Mach waves generated by the LICES. With the exception of the case with largest velocity and temperature, $d\delta/dy \leq \sin^{-1}(1/M_c)$, which can also be observed in Fig. IV.2. Nonetheless, for large temperature and velocity perturbations we can expect the local temperature to increase behind the LICES. If this is the case, the local speed of sound will increase (proportional to $T_l^{1/2}$) and the slope of the Mach line will also increase accordingly. From Fig. IV.4, where we show $x - z$ and $x - y$ plane averages of temperature, we can see that the

increase of temperature is significant and that it increases with both T_l and u_l. It is then anticipated that the rate of spread will be confined to the local Mach angle behind the LICES rather than M_c. For the highest temperature, the Mach angle can drop down to $M \sim 4.5$, which would increase the angle from ~ 0.2 to ~ 0.225.

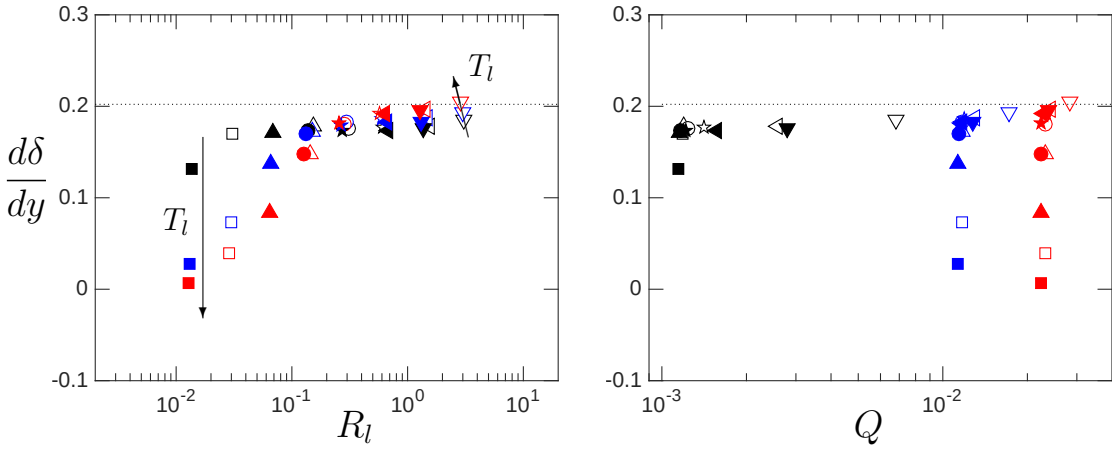

Figure IV.3. Rate of spread $\frac{d\delta}{dy}$ as a function of LICES Reynold number R_l (left) and Q (right) for all Cases in Table IV.1. Colors correspond to $T_m = 1$ (black), 10 (blue), 20 (red). Different symbols correspond to $u_m = 1$ (squares), 5 (up-triangle), 10 (circle), 20 (star), 50 (left-triangle), 100 (down-triangle). Open and closed symbols are for two different $\kappa_{\max}$ of 2 (open), 12 (closed). Horizontal dotted line corresponds to $\sin^{-1}(1/M_c)$.

To understand how the kinetic energy and dissipation have an effect on the rate of spread, we can take an $x - y$ plane average at half of the domain along $z = 1/2\, L_z$. This plane cuts through half of the LICES, making the average of this plane independent of $d\delta/dy$, which is not the case for any plane average along y or x. To quantify the effect of both dissipation and K with one parameter, we may normalize dissipation using the width of the LICES ($2\, r_l$), and the turbulent kinetic

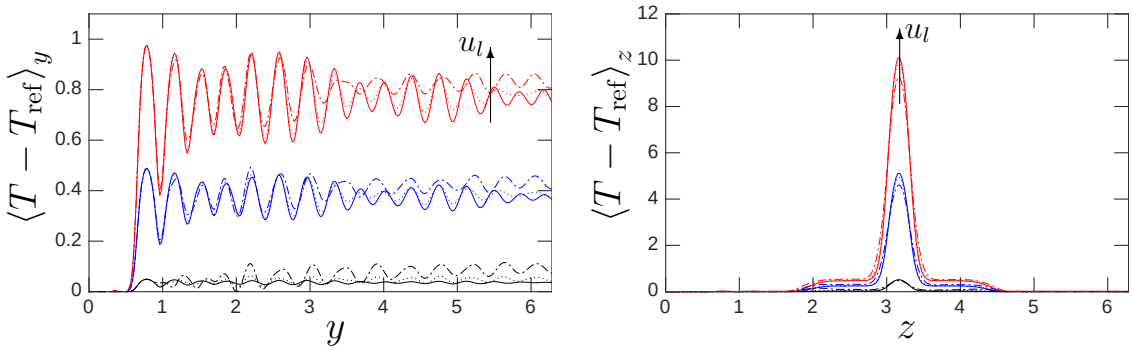

Figure IV.4. Temperature $x-z$ plane averages as function of axial distance (left) and $x-y$ averages as a function of transverse distance (right) for $T_m = 1$ (black), 10 (blue), and 20 (red). Different line styles correspond to velocity, $u_m = 1$ (solid) $u_m = 50$ (dotted), and $u_m = 100$ (red).

energy:

$$\psi = \frac{\epsilon \, 2 \, r_l}{K^{3/2}} \tag{4.4}$$

In Fig. IV.5 we show the plane average of ψ evaluated at $z = 1/2 \, L_z$. This parameter has been extensively used in compressible turbulence to asses the so-called dissipative anomaly (Sreenivasan, 1984, 1998; Donzis *et al.*, 2005). For low R_l, we see that the normalized dissipation ψ is much larger than unity, which is typical of low Reynolds number (Sreenivasan, 1998). However, we can see that for the large R_l cases ($R_l \gtrsim 0.5$) ψ becomes of order one, also consistent with the literature. It is also around this R_l that $d\delta/dy$ asymptotes with the Mach angle. An interesting observation is that for the smallest R_l, ψ is larger when T_l is small. This trend then reverses quickly by $R_l \gtrsim 0.1$. When R_l is small, the velocity perturbations are also very small, so having large temperature dampens out the perturbation rapidly, decreasing K and thus increasing ψ.

In summary, both T_l and u_l have a strong effect on the rate of spread, which can be quantified by the LICES Reynolds number R_l. We find that for sufficiently

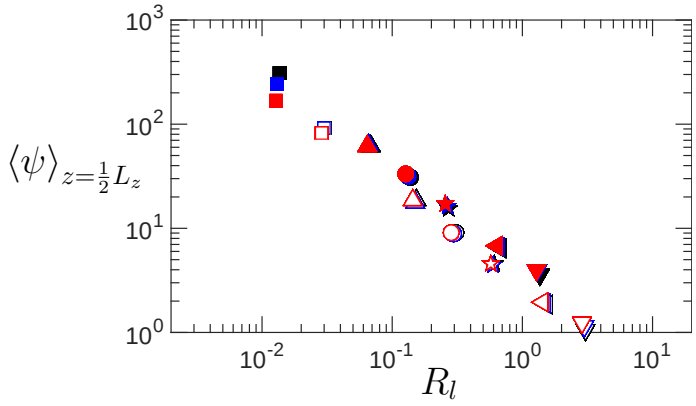

Figure IV.5. Plane average $(x-y)$ of ψ as a function of R_l for all simulations. Plane chosen is at half of the domain $\frac{1}{2}L_z$, which cuts through the center of the LICES. Same colors and symbols as Fig. IV.3.

large R_l, the dissipation qualitatively scales as in incompressible turbulence with large-scale length scale and turbulent kinetic energy, and that the spreading rate asymptotes with the local Mach angle. From careful examination of the database, we found this asymptote (i.e. $d\delta/dy \sim \sin^{-1}(1/M)$) is achieved when $R_l > 0.5$.

IV.B. Flow evolution: interaction between LICES

An objective of this chapter is to determine if LICES can help improve the poor fuel and oxidizer mixing efficiency in air breathing hypersonic vehicles, or hypersonic flows in general. As noted in the introduction, there is a rapid decay in mixing efficiency of supersonic compared to subsonic flows (Gutmark *et al.*, 1995; Birch & Eggers, 1972; Morris *et al.*, 1990; Goebel & Dutton, 1991; Lele, 1989). Although the solution to this problem is well known, small scale turbulence (Dimotakis, 2005), creating homogeneous isotropic turbulence in hypersonic flows is not trivial. While LICES may be a possible solution, their ability to generate turbulence from very

confined concentrated sources of energy is not known. Furthermore, if it is possible, we must then quantify the effectiveness of generating turbulence from LICES and understand when and why the flow transitions to fully developed turbulence.

In the previous section we quantified the spreading rate of perturbations and identified the main mechanism that control $d\delta/dy$, with the LICES Reynolds number R_l being a suitable parameter to characterize it. In this section we will study the interaction of several intersecting LICES, as shown in the schematic of Fig. II.5. Two simulations with this setup are shown in Fig. IV.6 and Fig. IV.7. One has high T_l and low u_l, while the other has low T_l and high u_l. It is clear that both temperature and velocity have a qualitative effect on the evolution of the flow, where the latter conditions seem to favor turbulent mixing. To quantify the degree of turbulence in the flow we will look at widely used quantities that measure such condition, including skewness of the velocity gradient, root mean square velocity ratios, and energy spectra. The large database of simulations, described in Table IV.2, will be used to study all these quantities.

It is also noted from Fig. IV.6 that when T_l is high the flow behind the LICES appears to be reasonably statistically stationary. However, when the flow is turbulent, most quantities experience fluctuations over a wide range of scales. It is then useful to split a variable f into mean and fluctuations, such that $f = \overline{f} + f^{\dagger}$ where as defined above and overbar is a time average. We can then compute fluctuation in time by $f^{\dagger} = f - \overline{f}$. As we will see below, studying the statistics of both f and $f^{\dagger}$ provide complimentary insight into the large scales features of the flow as well as the small scale turbulence structure that emerges respectively.

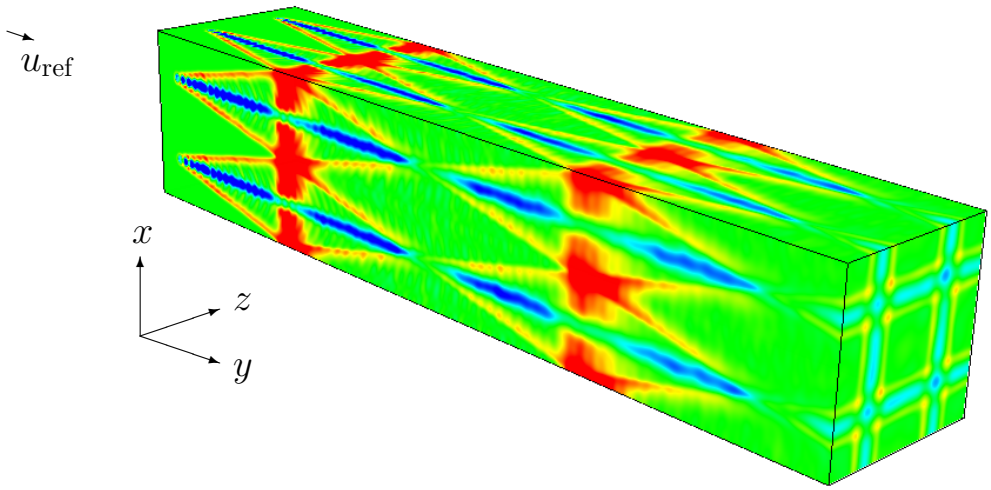

Figure IV.6. Visualization of $1/2(u_1^2+u_2^2+u_3^2)$ for low R_l with high T_l (Case 1 from Table IV.2). Color scheme increases from blue to red with green being intermediate values.

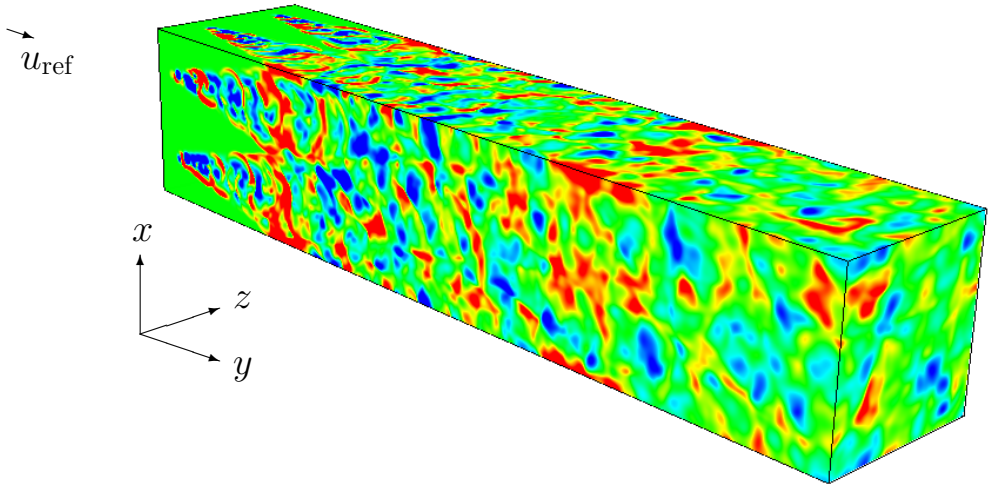

Figure IV.7. Visualization of $1/2(u_1^2+u_2^2+u_3^2)$ for high R_l with low T_l (Case 14 from Table IV.2). Color scheme increases from blue to red with green being intermediate values.

Case	N_l	u_m	T_m	$\kappa_{\max}$	u_l	T_l	ν_l	H_f	$N_{x,z} \times N_y$	$L_{x,z} \times L_y$	R_l	R_λ
1	4	10	20	2	3.67	10.20	4.36	2000	256×1280	$2\pi\times10\pi$	1.18	1.96
2	4	30	20	2	11.00	10.20	4.36	2000	256×1280	$2\pi\times10\pi$	3.54	2.48
3	4	50	20	2	18.33	10.20	4.36	2000	256×1280	$2\pi\times10\pi$	5.90	3.35
4	4	70	20	2	25.66	10.20	4.36	2000	256×1280	$2\pi\times10\pi$	8.26	4.37
5	4	160	20	2	58.65	2.04	4.05	2000	256×1280	$2\pi\times10\pi$	20.30	7.78
6	4	10	1	2	3.67	0.51	3.99	2000	256×1280	$2\pi\times10\pi$	1.29	0.73
7	4	30	1	2	11.00	0.51	3.99	2000	256×1280	$2\pi\times10\pi$	3.86	2.16
8	4	50	1	2	18.33	0.51	3.99	2000	256×1280	$2\pi\times10\pi$	6.44	3.40
9	4	70	1	2	25.66	0.51	3.99	2000	256×1280	$2\pi\times10\pi$	9.01	4.38
10	4	90	1	2	32.99	0.51	3.99	2000	256×1280	$2\pi\times10\pi$	11.59	5.22
11	4	110	1	2	40.32	0.51	3.99	2000	256×1280	$2\pi\times10\pi$	14.17	6.48
12	4	135	1	2	49.49	0.51	3.98	2000	256×1280	$2\pi\times10\pi$	17.46	7.22
13	4	150	1	2	54.99	0.51	3.99	2000	256×1280	$2\pi\times10\pi$	19.32	7.85
14	4	160	1	2	58.65	0.51	3.99	2000	256×1280	$2\pi\times10\pi$	20.60	8.41

Table IV.2. All converged simulations run. R_λ is averaged from $y = 0.8\,L_y$ to L_y.

IV.B.1. Velocity and velocity gradients

To measure large scale anisotropy we can use the ratio of root mean squared (rms) velocities (denoted by a prime). The rms is defined as:

$$u_i'(y) = \sqrt{\left\langle \left(u_i - \langle u_i \rangle_y \right)^2 \right\rangle_y} \tag{4.5}$$

where the subscript y represents the plane average at the particular y location. In Fig. IV.8 we have the ratio of time-averaged rms velocities for two cases with low and high T_l. The perturbations we introduce are equivalent for the three components of velocity, so it is expected that the ratio should be close to one, even close to the grid.

For low T_l, although we have some oscillations for the axial to transverse rms close to the grid due to the pulsating nature of the LICES, these tend to equipartition at short distances. On the other hand, when we have large T_l, the transverse rms is larger than the axial, with no clear proclivity towards equipartition in terms of axial distance. In fact, it appears as the ratio of axial to transverse rms decreases with increasing distance from the grid. This is due to the effect of the Mach waves, which are found to affect the velocity fluctuations differently in different directions. Here we can also see the strong effect of acoustics where we have large peaks in the rms at factors of y_{M_c}, which correspond to the location of the Mach waves evident from the low R_l case in Fig. IV.8. If we removed the time averaged velocity field, we would expect these strong peaks to disappear. This is indeed what we observe from Fig. IV.9, supporting the claim that the lower axial-to-transverse rms is due primarily to the effect of the Mach waves at high T_l.

In Fig. IV.10 we can see the value of rms ratios averaged at three different locations downstream. At the location of the LICES, we see equipartition independent of R_l and T_l which is expected since by construction velocity perturbation are similar in all directions. Then, consistent with the observations in Fig. IV.8, the axial rms is significantly lower than the transverse rms, primarily for low R_l. An interesting observation is that for low T_l and away from the grid, the axial rms appears to be slightly larger than the transverse. Larger axial to transverse rms velocities have been reported for grid generate turbulence experiments (Comte-Bellot & Corrsin, 1966; Gad-el Hak & Corrsin, 1974; Mydlarski & Warhaft, 1996) due to the inhomogeneity of the generator (grid). Axial contractions have shown to decrease the anisotropy

by amplifying the transverse velocity fluctuations (Comte-Bellot & Corrsin, 1966), yet some experiments suggest that anisotropy returns (Uberoi & Mahinder, 1957). It is worth noting that although we still have some degree of anisotropy, the axial rms is only approximately 2-4% larger than the transverse, while most reported experiments show between 10-20% larger axial rms.

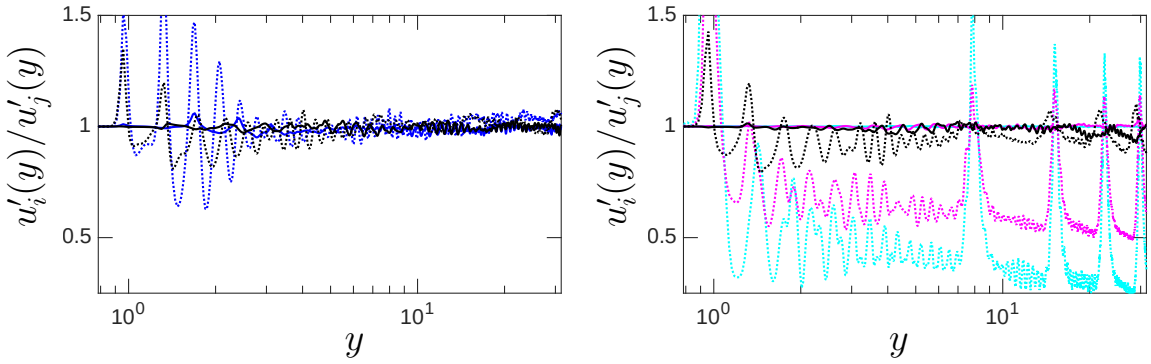

Figure IV.8. Ratio of root mean squared velocities for $T_m = 1$ (left) and $T_m = 20$ (right). Different line styles for ratio of transverse velocities (u_1'/u_3') (solid) and axial to transverse (u_2'/u_3') (dotted). Different colors correspond to to $u_m = 10$ (cyan), 30 (magenta), 70 (blue), and 160 (black).

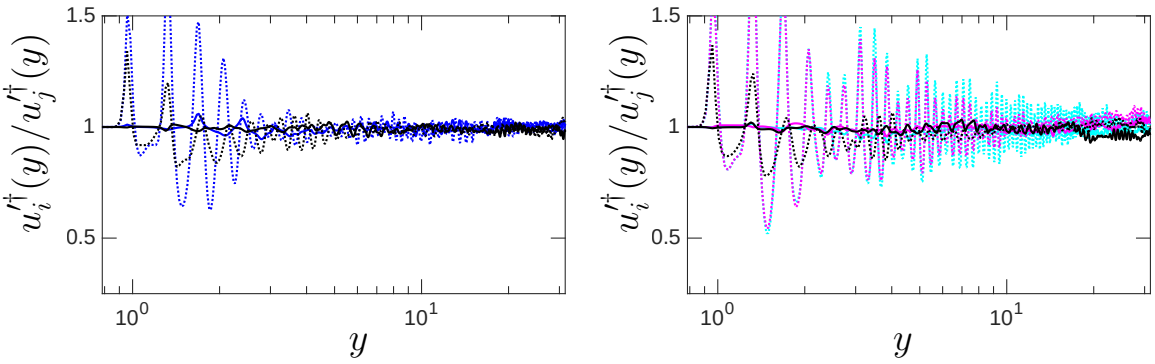

Figure IV.9. Ratio of root mean squared velocities using the fluctuating velocity in time. Same colors and line style as Fig. IV.8.

Another widely accepted measure to test the establishment of turbulence is the

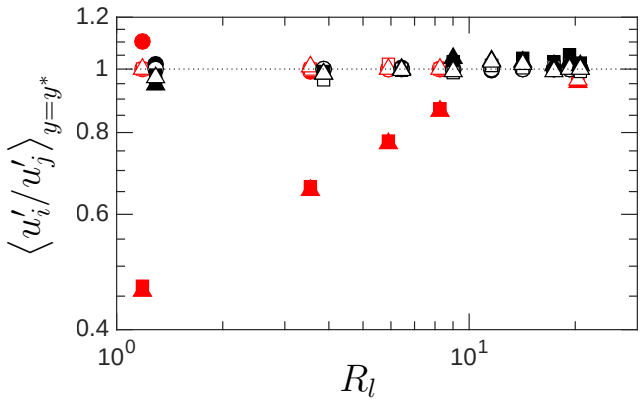

Figure IV.10. Ratio of root mean squared velocities at different y locations, where the asterisk corresponds to $y =$ LICES (circles), $0.4\,L_y - 0.6\,L_y$ (squares), and $0.8\,L_y - L_y$ (triangles). Different colors correspond to $T_m = 1$ (black) and 20 (red). Filled symbols for ratio of transverse velocities (u_1'/u_3') and empty symbols for axial to transverse (u_2'/u_3').

skewness of velocity gradients, which measures the transfer of energy from large to small scales (Sreenivasan & Antonia, 1997). The skewness of longitudinal velocity gradients can be defined as:

$$\langle S_{u_i} \rangle_* = \frac{\left\langle \left(\frac{\partial u_i}{\partial x_i} - \left\langle \frac{\partial u_i}{\partial x_i} \right\rangle_* \right)^3 \right\rangle_*}{\left\langle \left(\frac{\partial u_i}{\partial x_i} - \left\langle \frac{\partial u_i}{\partial x_i} \right\rangle_* \right)^2 \right\rangle_*^{3/2}} \tag{4.6}$$

where the asterisks will be used to indicate whether the average is taken over the entire domain, planes, or lines. For fully developed turbulence, it is well known that the value of S_{u_i} approaches -0.5 (Tavoularis *et al.*, 1978; Sreenivasan & Antonia, 1997). The evolution for S_{u_i} as a function of axial distance can be seen in Fig. IV.11 for two different T_l and several velocities u_l. The start of LICES is at $\frac{\pi}{4} - r_l$, which is approximately $y \sim 0.5$. Before this point the skewness of velocity gradient is not well defined, as the variance is zero. At the LICES the skewness is close to zero, which is expected given the symmetry of the imposed distribution. Downstream of the LICES

we can see a very different evolution between the low and high T_l simulations. For very low u_l or large T_l we see a strong effect of acoustics on the transverse velocity gradients S_{u_1} and S_{u_2}, where the skewness changes drastically at the location where the Mach waves intersect. This location, computed based on the convective Mach angle is approximately $y_{M_c} = 7.75$. Since the boundary conditions along x and z are periodic, the Mach waves will intersect at y_{M_c}, $2\,y_{M_c}, 3\,y_{M_c}$ and $4\,y_{M_c}$ before exiting the domain. If we remove the time averaged velocity filed, the effect of the Mach waves disappears, as evident from Fig. IV.12.

For all the cases, except 6 and 7 from Table IV.2, the transverse skewness of longitudinal velocity gradients goes negative after the LICES and then tends towards -0.5 as distance increases downstream. When the temperature is high, the evolution of S_{u_1} and S_{u_2} towards fully developed turbulence appears to be very slow from Fig. IV.11. However, if we consider $S^{\dagger}_{u_i}$ the evolution is significantly faster, yet still slow compared to low-T_l case. This results again supports the idea that fluctuations appear to approach a realistic turbulent state superimposed on a flow with strong large-scale acoustic components which are essentially steady. This result also suggests that care has to be exercised when studying flows with this characteristics but that the removal of time-averaged quantities could help disentangle the different effects.

The streamwise velocity gradient S_{u_2} is more sensitive to the forcing frequency H_f, where we see strong oscillations at factors of y_c. The oscillations decrease downstream with y and also with increasing R_l. For the cases with low T_l, increasing u_l tends the three longitudinal velocity gradients towards the value for isotropic turbulence at large y. If we focus on the case with $u_m = 70$, it appears that the transverse

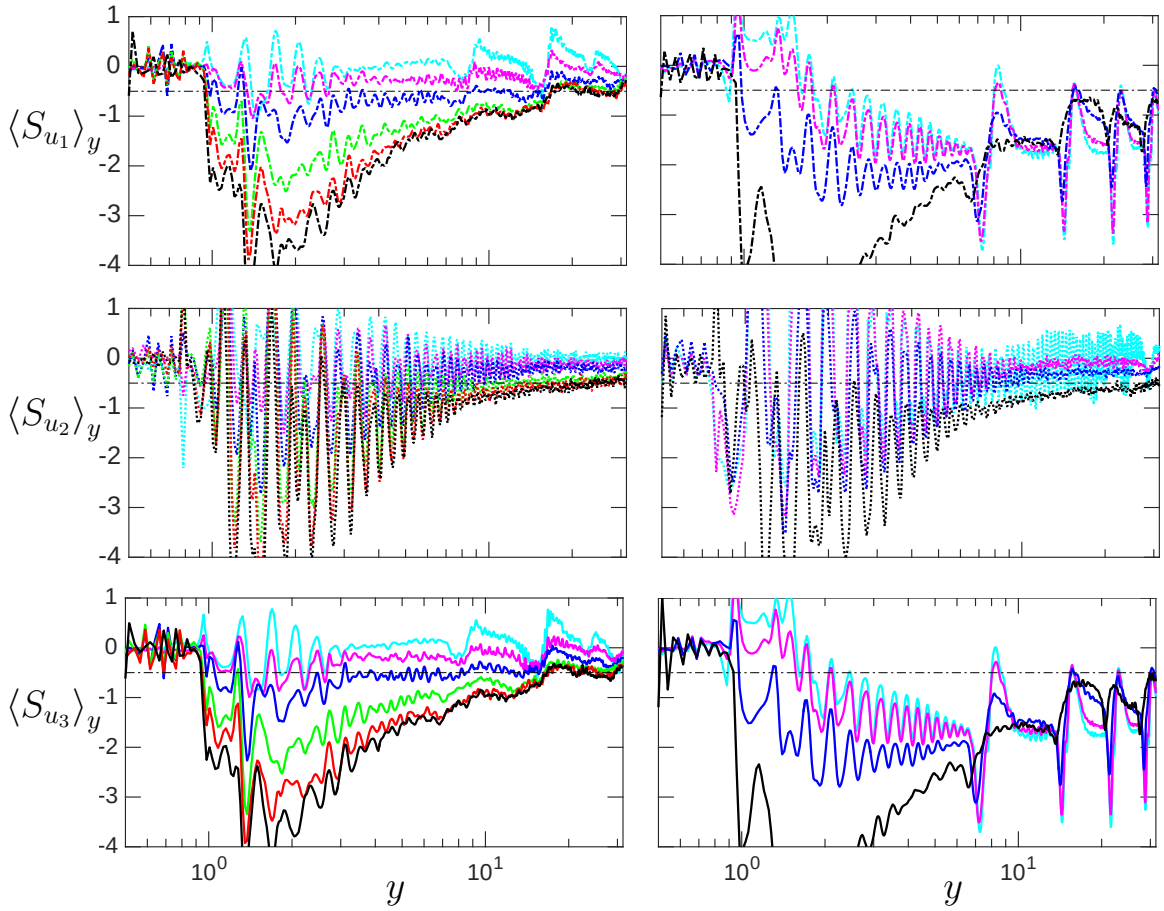

Figure IV.11. Skewness of longitudinal velocity gradients as a function of axial distance for $T_m = 1$ (left) and $T_m = 20$ (right). Different colors correspond to $u_m = 10$ (cyan), 30 (magenta), 70 (blue), 110 (green), 150 (red), and 160 (black).

skewness reaches -0.5 very close to the grid. However, as y is increased the value departs from that of developed turbulence. It is then not clear if this is a transition stage, or if realistic turbulence is effectively established at those conditions. This will be re-visited when we study one-dimensional energy spectra. The behavior for the three cases shown with low T_l and largest u_l is similar, with the three skewness of velocity gradients reaching that of isotropic turbulence.

In Fig. IV.13 we show the mean of the three skewness of velocity gradients using

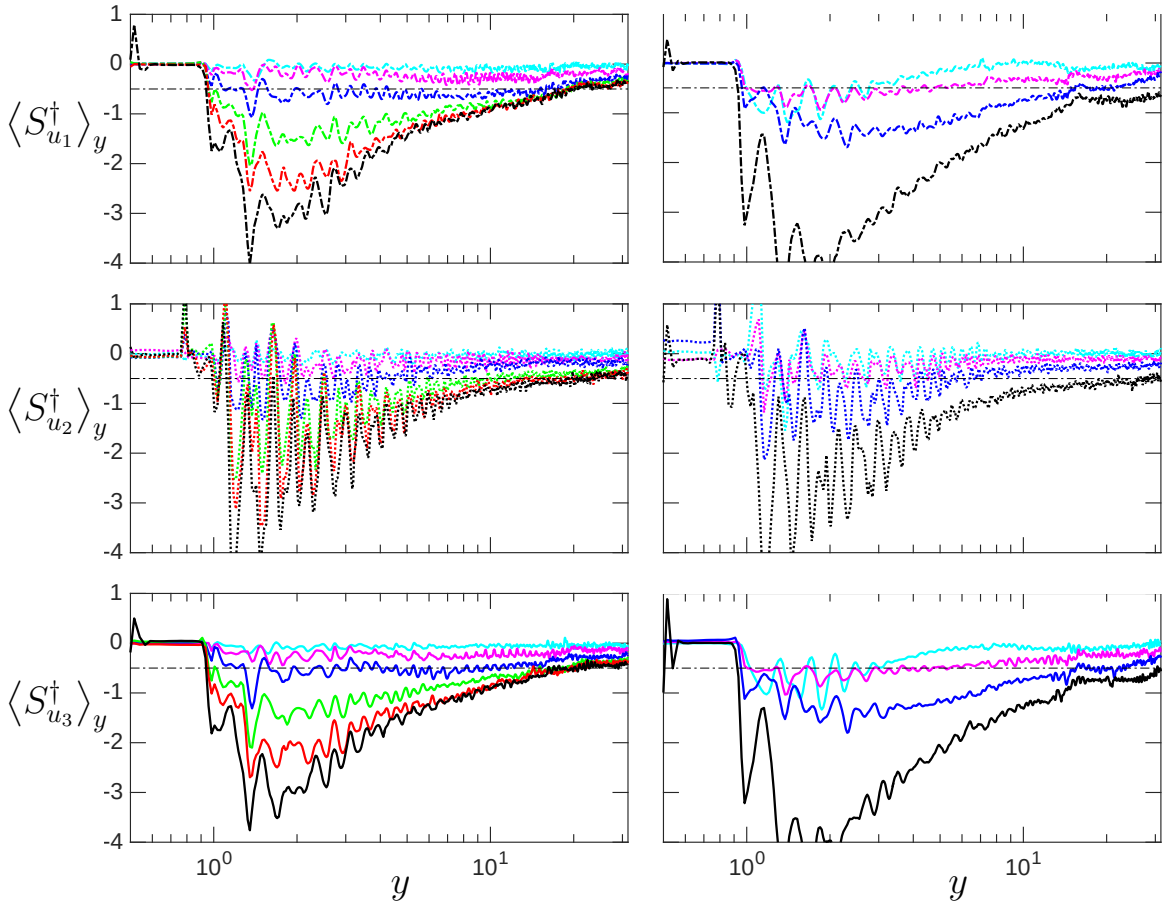

Figure IV.12. Skewness of longitudinal velocity gradients as a function of axial distance using fluctuating velocity in time.

total and fluctuating quantities averaged at three locations of y: at the LICES, from 0.4 to 0.6 L_y and from 0.8 to L_y. At the LICES the skewness is nearly zero for all cases, as expected. For the skewness computed using the total velocity we see a contrasting behavior between low and high temperature cases. For those with high T_l, the skewness has negative values larger than -0.5 and becomes less negative with increasing R_l. There is no clear distinction between the averages taken at half of the domain and close to the exit. This indicates that if T_l is large, extremely long distances are required to reach turbulence. In contrast to the high T_l cases,

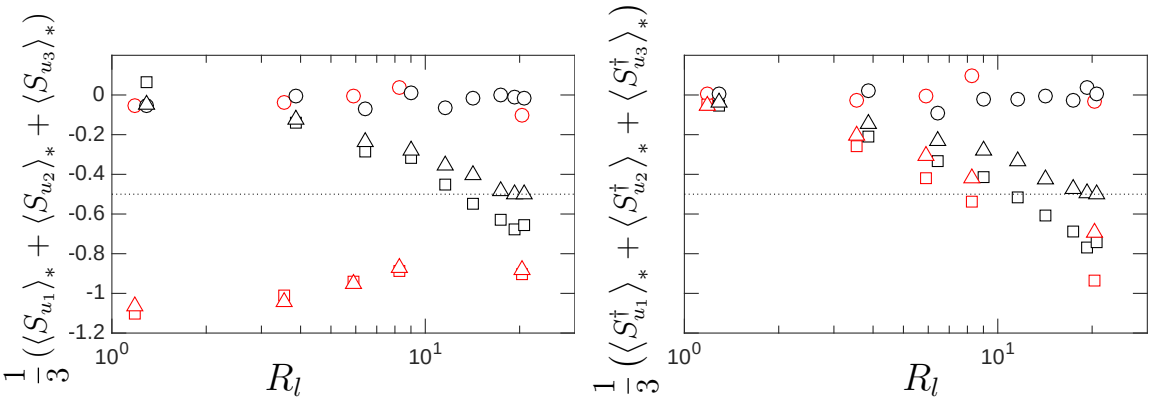

Figure IV.13. Skewness of averaged longitudinal velocity gradients as a function of R_l, space averaged at different locations downstream. Computed using total velocity (left) and fluctuating velocity (right). Same colors and symbols as Fig. IV.10. Dotted line at -0.5 representing homogeneous isotropic turbulence (Tavoularis *et al.*, 1978; Sreenivasan & Antonia, 1997).

for low T_l the skewness is close to zero at low R_l and becomes more negative as we increase R_l. Now we see a clear distinction between averages at half of the domain and at the exit. At half of the domain the skewness overshoots -0.5, while at the exit it asymptotes at -0.5. For the skewness computed using the fluctuating velocity, the same trend is observed between low and high T_l. Although higher temperature appears to slow down the transition to turbulence, we can now see a difference between quantities evaluated at half of the domain and the exit, with a clear trend towards turbulence values as the axial distance is increased. It is important to note that for low temperature and high R_l the skewness of velocity gradients tends to the value found in isotropic turbulence independent of how we evaluate the quantity.

We close this section by summarizing the main conclusion from observations of ratios of rms velocities and normalized moments of velocity gradients. This conclusion is that three conditions must be met to generate realistic turbulence: T_l must be small, y must be sufficiently large, and $R_l \gtrsim 15$. A quantitative assessment of this

conditions is given in the next section where we investigate the scaling of the energy spectrum.

IV.B.2. One-dimensional energy spectra

If turbulence is established for the set of conditions previously described, we would also expect the flow to acquire the structural signature of fully developed turbulence. Universality of the small scales is one of the signatures. Thus, we can expect the energy spectrum to approach that of isotropic turbulence at the same Reynolds number under K41 (**?**) scaling. Due to the non-periodic boundary condition along the axial component, we may not directly compute the three-dimensional energy spectra. Nonetheless, we can still compute the one-dimensional energy spectra in the first and third components where periodicity is enforced. The one dimensional energy spectra is defined (Pope, 2000) as $E_{ij}(k_1) = \frac{1}{\pi}\int_{-\infty}^{\infty} e^{-\iota\, k_1\, r_1} R_{ij}(\mathbf{e_1} r_1)\mathrm{d}r_1$, where $R_{ij} = \langle u_i(x)^* u_j(x + \mathbf{e_1}\, r_1)\rangle$ is the velocity autocorrelation function, k_1 is the wave number, and $\mathbf{e_1}$ the basis vector.

In Fig. IV.14 we show the timed averaged one-dimensional energy spectra normalized using the dissipation ϵ, wave number k, and Kolmogorov microscale $\eta = (\nu^3/\epsilon)^{1/4}$ Tennekes & Lumley (1972) for low T_l cases at three different axial distances. For the cases with low T_l, the only difference between E_{ij} and $E_{ij}^{\dagger}$ is seen at the large scales which do not change conclusions from the results. Consequently, only results for total velocity field are shown. The first axial distance shown is for the location of the LICES. At this point the spectra is defined strictly by the introduced perturbations and is not expected to collapse with isotropic turbulence under K41

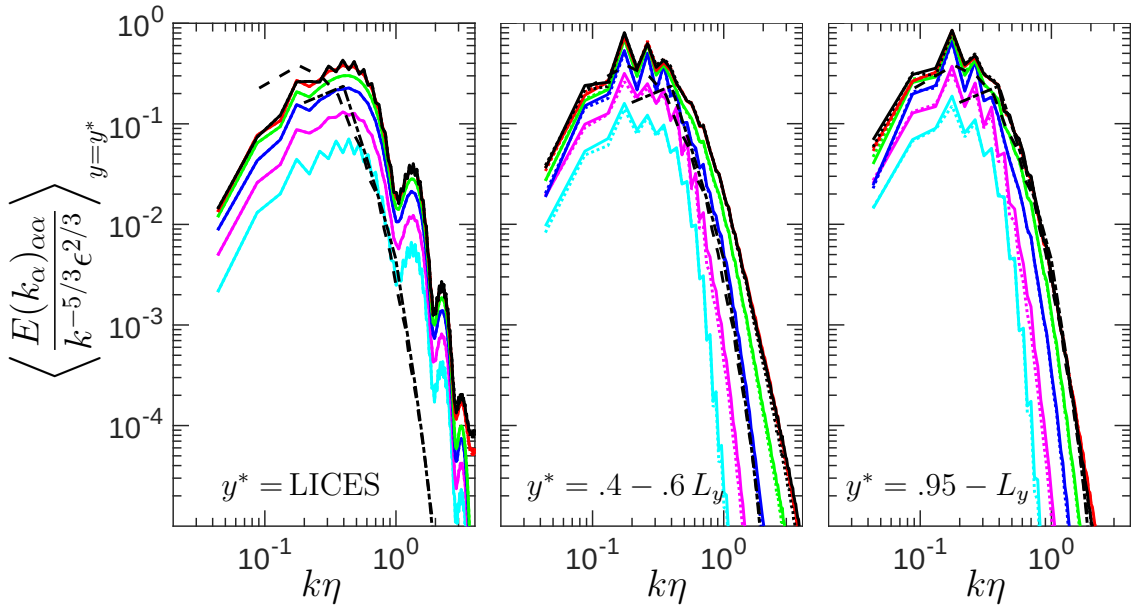

Figure IV.14. Normalized one dimensional energy spectra for $T_m = 1$, with same colors Fig. IV.11. Solid lines for $\alpha = 1$ and dotted for $\alpha = 3$. Dashed lines for homogeneous isotropic turbulence with $R_\lambda \sim 10$ and dash-dot for $R_\lambda \sim 17$.

scaling. At the second location, which is the average of half of the domain $\pm 10\%\, L_y$, we see that only one case collapses with isotropic turbulence. This case has low temperature and intermediate velocity $u_m = 70$. For this particular case, the transverse components of the skewness goes to -0.5 at this specific y location. Therefore, it is not surprising that transverse one-dimensional spectra collapses well with isotropic turbulence. However, for this case S_{u_2} does not go to -0.5, so the the flow is only isotropic in the transverse plane and it is likely and that neither the stream-wise one-dimensional energy spectra, nor the three-dimensional energy spectra will collapse with isotropic turbulence. Consequently, although we see close agreement in the one-dimensional spectra, we cannot claim fully developed turbulence under those specific conditions. The third location where we evaluate the spectra is at the exit,

from 95% of the domain to the end. Here we see close agreement with the case with $u_m = 110$ and excellent collapse with the two large R_l cases. For the three cases with the largest $R_l \sim 17 - 20$, we find agreement with isotropic turbulence in the three components of S_{u_i}, in the ratio of rms velocities, and finally in the two components of the energy spectra available.

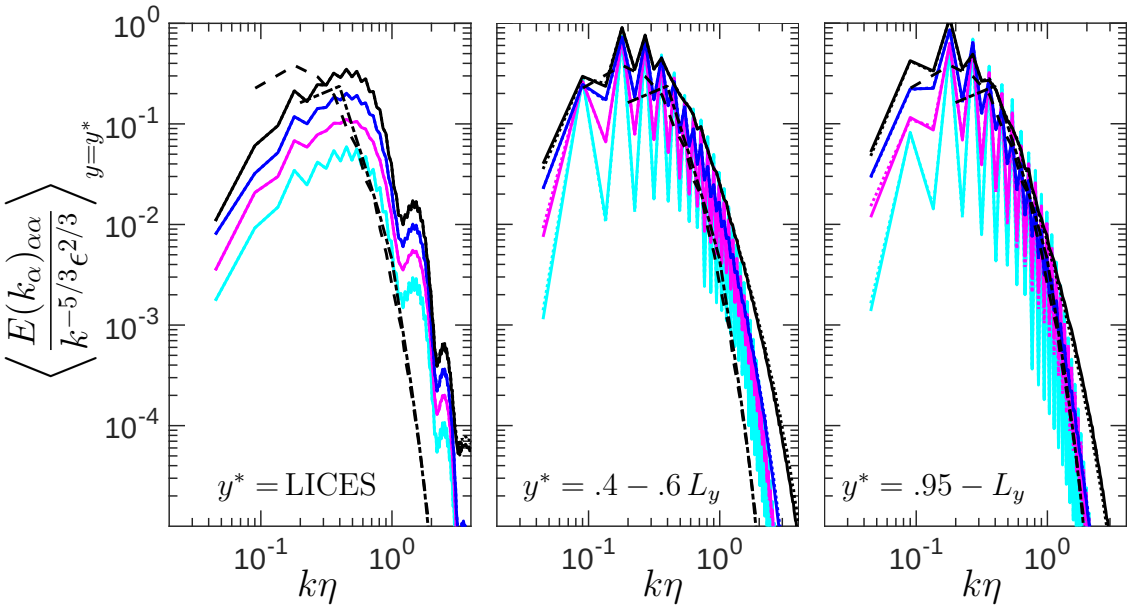

Figure IV.15. Normalized one dimensional energy spectra for $T_m = 20$, with same colors Fig. IV.11. Solid lines for $\alpha = 1$ and dotted for $\alpha = 3$. Dashed lines for homogeneous isotropic turbulence with $R_\lambda \sim 10$ and dash-dot for $R_\lambda \sim 17$.

In Fig. IV.15 we have the timed averaged one-dimensional energy spectra computed using the total velocity for the cases with high T_l at the same three axial distances shown for low T_l. At the location of the LICES there is no distinguishable difference between low and high T_l. As we move downstream we see very strong oscillations for the cases with lower velocity u_l. These oscillations decrease with increasing R_l and can be attributed to the Mach waves. For the cases with very low

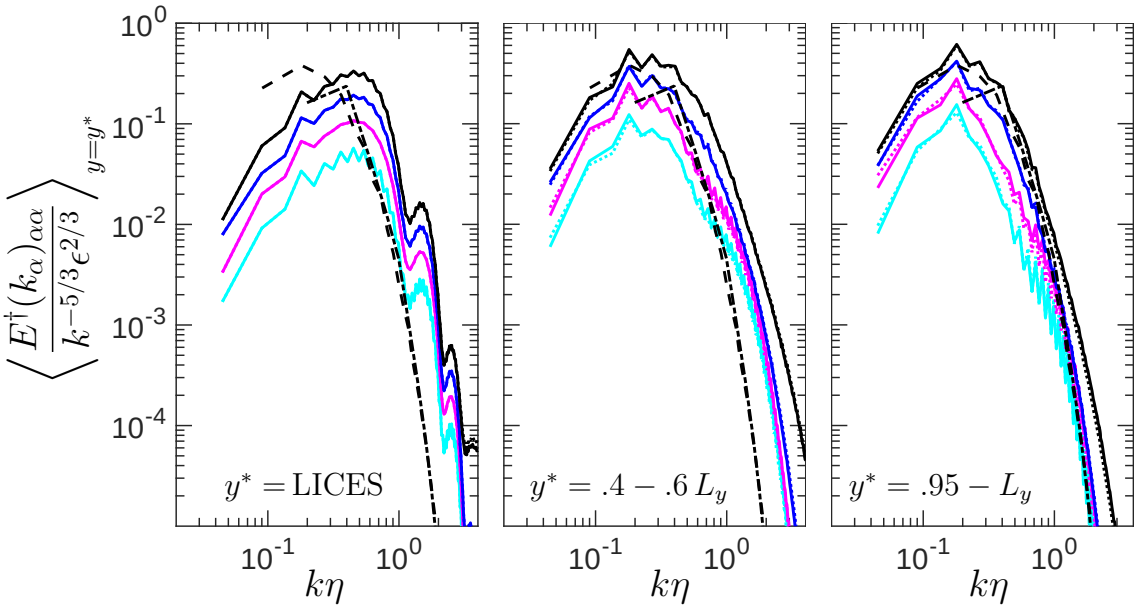

Figure IV.16. Normalized one dimensional energy spectra for $T_m = 20$ computed using the fluctuating velocity field, with same colors and line styles as Fig. IV.15.

u_l and high T_l, the primary perturbations arise from the Mach waves, as turbulent fluctuations are negligible. The velocity of a single component in an transverse plane will be similar to a square wave oscillating between positive and negative velocity, as may be seen visually in Fig. IV.6 (left). A simple model for an alternating signal like that is a square wave which in spectral space contains only odd Fourier modes (for example, $1 = \frac{4}{\pi}(\sin(x) + \frac{\sin(3\,x)}{3} + \frac{\sin(5\,x)}{5} \ldots$ (Tolstov, 2012)). This helps explain, in a qualitative way, the fluctuating nature of the spectra in Fourier space. As R_l is increased, more perturbations are generated and the oscillations tend to disappear. For the case with largest R_l, the strong oscillations vanish but we still do not see a collapse with isotropic turbulence. This is expected given the results from velocity and velocity gradients. In Fig. IV.16, we show the spectra for the same cases as Fig. IV.15 computed using the fluctuating velocity field. As we expect, the strong

oscillations at low u_l have decreased drastically. Although the effect of Mach waves is virtually removed when using only fluctuating quantities, there is still no collapse with isotropic turbulence. This demonstrates that if the conditions are satisfied for the establishment of fully developed turbulence, Mach waves will no longer have an effect on the flow properties and in general the statistics of f will be similar to $f^{\dagger}$.

The excellent agreement of the energy spectrum for low T_l and high R_l supports the results from velocity and velocity gradients, indicating three conditions for fully developed turbulence:

1. $y/d_l \gtrsim 5$
2. $T_l/T_0 \lesssim 1\%$
3. $R_l \gtrsim 15$

Note that this does not preclude the generation of turbulence at higher T_l. In such a case, however, we expect a higher R_l will be needed as well as a larger distance downstream of the LICES. Though, confirmation of these claims would require further numerical experiments.

IV.B.3. Reynolds number

In the previous section we showed that, when a set of conditions is met, turbulence can be generated from LICES. It is now of practical importance to quantify in some sense the strength of the turbulence generated. A measure of this strength is the Reynolds number, which is the ratio of inertial to viscous forces. A widely used

definition of the Reynolds number is the Taylor Reynolds number:

$$R_\lambda = \frac{u'\,\lambda}{\nu} \tag{4.7}$$

where the u' is the rms velocity and $\lambda = \left\langle (u'^2/(\partial u'/\partial x)^2)^{1/2} \right\rangle$ the Taylor microscale. The smallest relevant scale in the flow is the Kolmogorov microscale $\eta = (\nu^3/\epsilon)^{1/4}$ (Tennekes & Lumley, 1972) which is related to the integral scale through $L/\eta = R_\lambda^{3/4}$ (**?**). This implies that separation between the largest and smallest scales increases with Reynolds number. Furthermore, if our largest scale is confined, increasing the Reynolds number will generate smaller scales which ultimately facilitate mixing, one of the main practical objectives of this work.

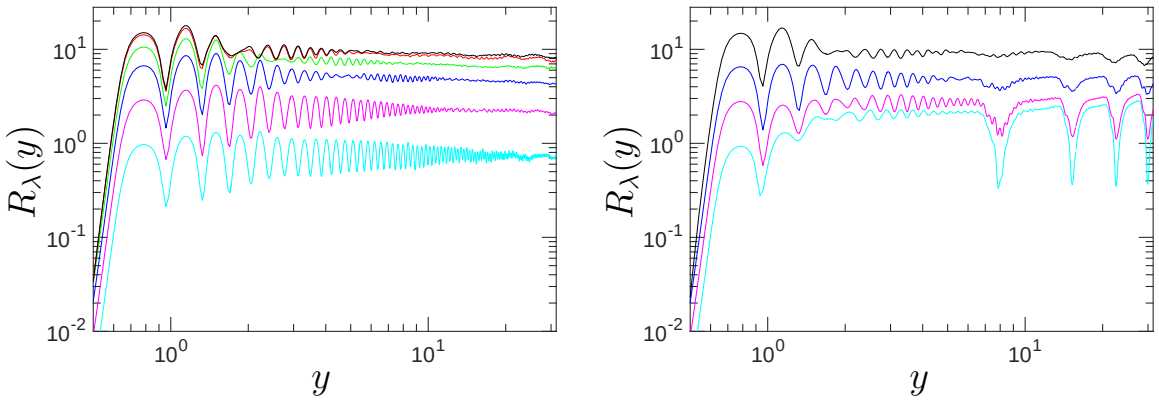

Figure IV.17. Taylor Reynolds number as a function of axial distance for $T_m = 1$ (left) and $T_m = 20$ (right). Colors are same as Fig. IV.11.

In Fig. IV.17 we show the Taylor Reynolds number as a function of axial distance. Upstream of y_{M_c} we can see the effect of H_f where the different peaks of R_λ correspond to individual LICES convected downstream. If $y > y_{M_c}$ and R_l is large, the distinctive peaks from the LICES disappear and R_λ becomes nearly insensitive to y, given T_l is also low. For large temperature we can clearly see the interacting Mach

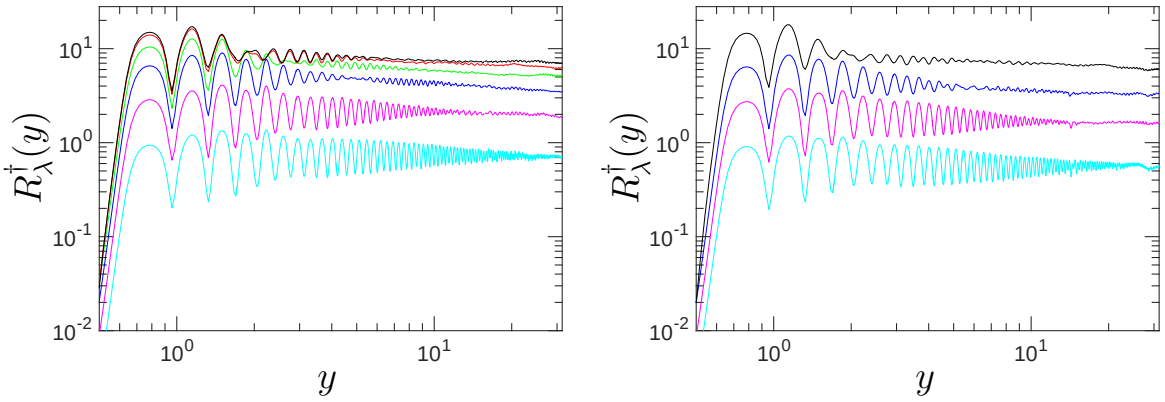

Figure IV.18. Taylor Reynolds number as a function of axial distance for $T_m = 1$ (left) and $T_m = 20$ (right). Colors are same as Fig. IV.11.

waves at factors of y_{M_c}, although the effect is reduced for increased R_l. Consistent with the previous quantities, the peaks at y_{M_c} disappear for $R_\lambda^\dagger(y)$ and a dependence of temperature is no longer visible if one compares Fig. IV.18 left and right.

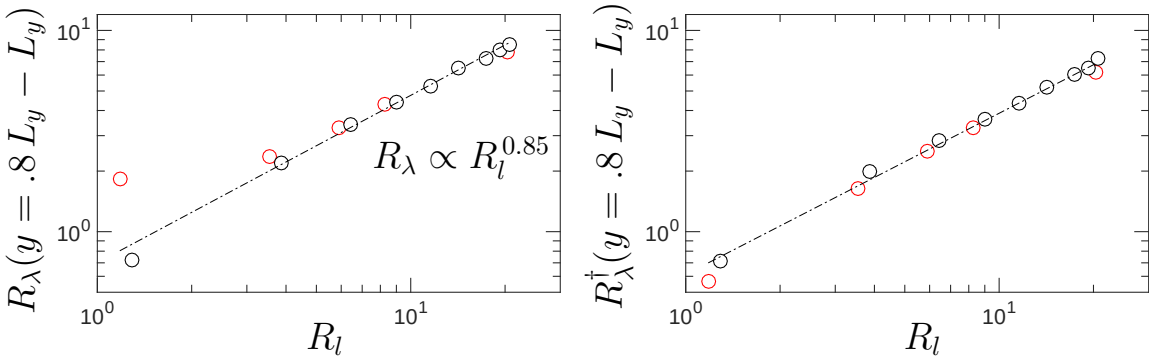

Figure IV.19. Taylor Reynolds number as a function of LICES Reynolds number computed using total velocity (left) and fluctuating velocity (right). Colors are same as Fig. IV.11. Dash-dot line for fit of data with $R_l > 2$.

From Fig. IV.17 and Fig. IV.18 we find that R_λ decays very slowly with respect to axial distance. For this reason, we only show results of R_λ as a function of R_l for the average of the last 10% of the domain in Fig. IV.19. We find that, with

the exception of low u_l, R_l collapses all simulations with different perturbations of velocity and temperature. The collapse is even better when we use the fluctuating velocity, as there are no departures at low R_l for high T_l. The relation between R_λ and R_l can be well represented by a power law of ~ 0.85 from a best fit based on the total velocity. The power found when using the fluctuating velocity is smaller, but within 5%. The weak power could present some limitations in the practical applicability of LICES, as reaching higher Reynolds number would require stronger perturbations while maintaining local low temperature along the LICES.

IV.B.4. Dilatational motions

Dilatational motions can act, in principle, at any scale. To study the effect of compressibility at the small scales, we may use the dilatational dissipation (Sagaut & Cambon, 2008):

$$\epsilon^d = \frac{4}{3}\nu \left(\frac{\partial u_i}{\partial x_i}\right)^2 \tag{4.8}$$

and we may also define $\chi_\epsilon = \langle \epsilon^d \rangle_* / \langle \epsilon \rangle_*$, where the asterisk indicates that different spatial averages may be taken. We wish to understand the emergence of dilatation motions downstream of the LICES. We may compute χ_ϵ for all y as it is computed using compact schemes. On the other hand, for χ we must extract 2π cubes at different y locations, apply windowing and then obtain the averaged dilatation through the Helmholtz decomposition. For statistical convergence this is then repeated for different times instances and then time averaged, making it a computationally expensive quantity.

In Fig. IV.20 we show χ for different y locations, where each point on the figure

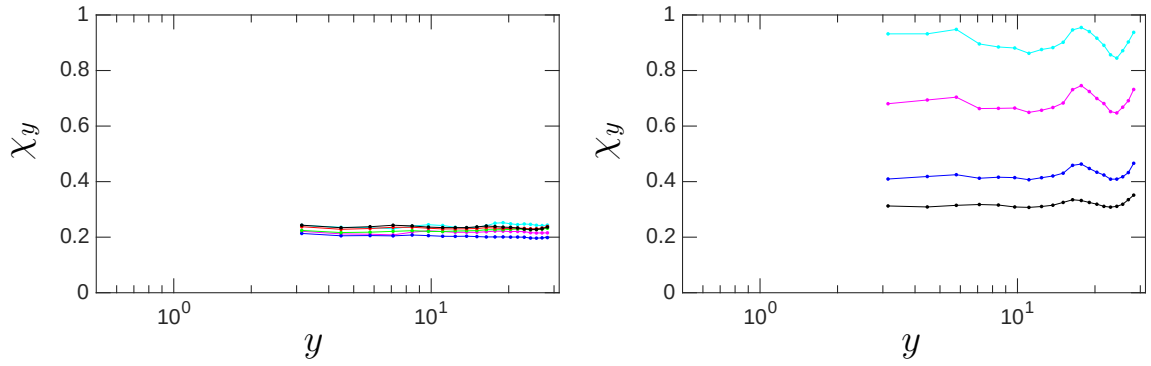

Figure IV.20. Ratio of dilatational to total velocity variance χ for $T_m = 1$ (left) and $T_m = 20$ (right). Colors are same as Fig. IV.11. y corresponds to the center of the $(2\pi)^3$ where χ is evaluated.

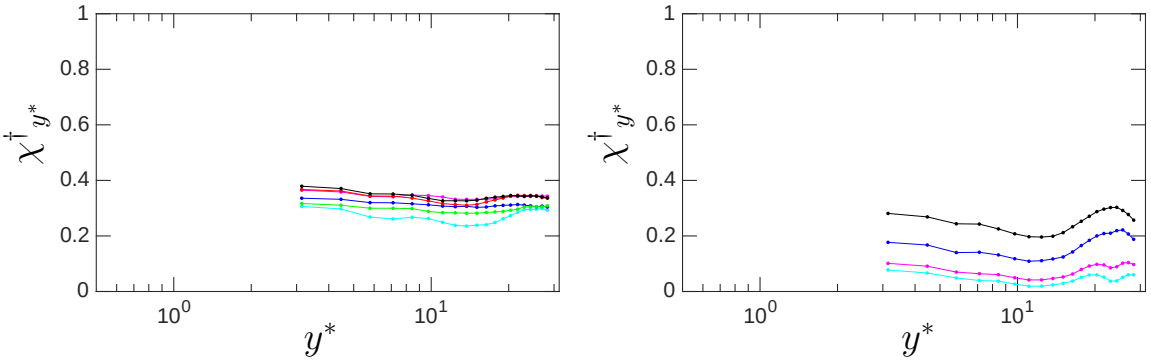

Figure IV.21. Ratio of dilatational to total velocity variance χ computed using the fluctuating velocity for $T_m = 1$ (left) and $T_m = 20$ (right). Same colors as Fig. IV.20.

corresponds to the center of the cubic domain where χ is computed, namely y^*. For this reason the first point is at π and the last at 9π. From the figure we can see that χ shows no clear dependence on y for small T_l, but there is a weak dependence on y for high T_l, with a few distinctive peaks that are associated to the Mach waves. Each point corresponds to a 2π average, so variations with y will be hard to capture if oscillations are around the mean of the quantity evaluated. There is also a monotonic trend with R_l for high T_l, where dilatation decreases with increasing R_l. On the other

hand, when T_l is low, χ decreases and then increases again.

Overall, the dilatational kinetic energy is larger when T_l is large. Lee & Girimaji (2013) have also observed that dilatational kinetic energy increases with heat release in the presence of temperature fluctuations. This is attributed to an increase in pressure dilatation from the heat release. When we introduce the additional temperature on the LICES, we will have temperature fluctuations between the mean and the LICES, and also on the distribution of the LICES themselves, proportional to 15% of T_m. Therefore, adding larger T_m increases both the heat release and temperature fluctuations.

If χ is computed using the fluctuating velocity, we find that there is a qualitative change in dilatational motions for high T_l. Now there is a monotonic trend where dilatation increases with R_l. This is not unexpected as we can attribute the strong dilatation to the stationary Mach waves generated behind the LICES. Upon removing the time averaged velocity, the Mach waves disappear and the dilatation can be expected to scale with the velocity introduced. We also find $\chi^\dagger$ to be smaller when T_l is large. As shown in Fig. IV.4, the temperature increases substantially behind the LICES when T_l is large, which will simultaneously increase the speed of sound. As the speed of sound increases, the turbulent Mach number M_t decreases and we can expect the dilatational contributions to weaken as χ scales with M_t (Jagannathan & Donzis, 2015).

As mentioned previously, we can compute χ_ϵ in physical space and we can therefore compute plane averages for each y location. In Fig. IV.22 we have the ratio of dilatational to total dissipation. It is clear that the ratio of dilatational to total

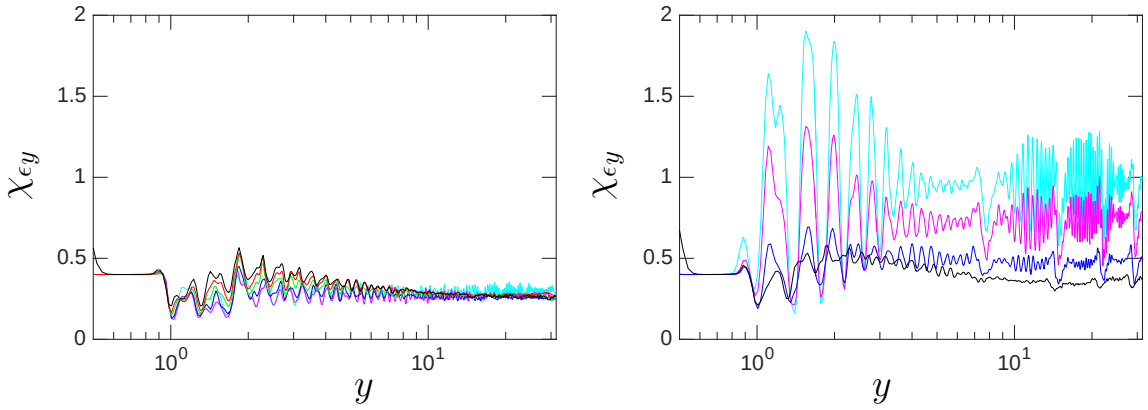

Figure IV.22. Ratio of dilatational to total dissipation χ_ϵ as a function of axial distance for $T_m = 1$ (left) and $T_m = 20$ (right). Colors are same as Fig. IV.11.

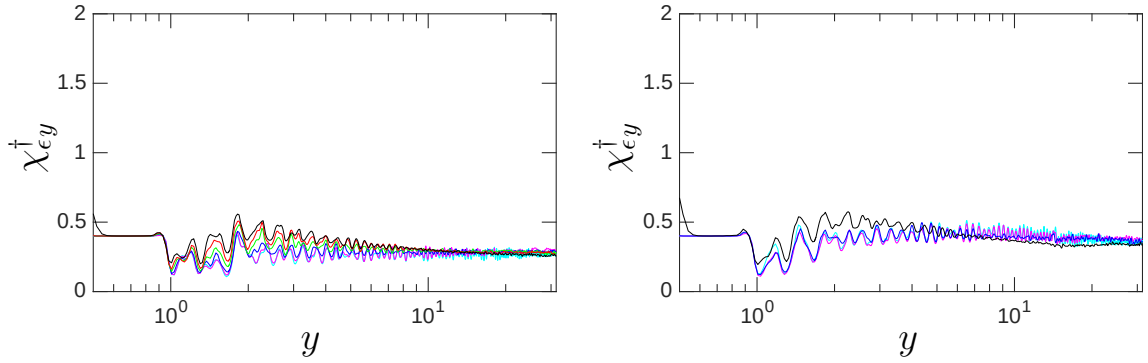

Figure IV.23. Ratio of dilatational to total dissipation computed using fluctuating velocity $\chi^\dagger_\epsilon$ as a function of axial distance for $T_m = 1$ (left) and $T_m = 20$ (right). Colors are same as Fig. IV.11.

dissipation we introduce at the LICES is constant and independent of temperature. However, similarly to χ, we see a difference in the evolution of χ_ϵ for different T_l. At high T_l we can see the interacting Mach waves at factors of y_{M_c}, whose effect decreases with increasing u_l. When u_l is low, we see strong fluctuations with respect to y which decrease at the region where the Mach waves interact. This is expected, as the flow has not evolved to a turbulent state and is very sensitive to H_f. Where the

planes interact, and we can expect the flow to be more homogeneous in this region. These oscillations are seen to go over unity, which implies the solenoidal dilatation becomes negative in this regions. This is only seen for the cases where T_l is large and can attributed to the inhomogeneous term of dissipation, which has a strong contribution given the inhomogeneity of flow as seen from Fig. IV.6.

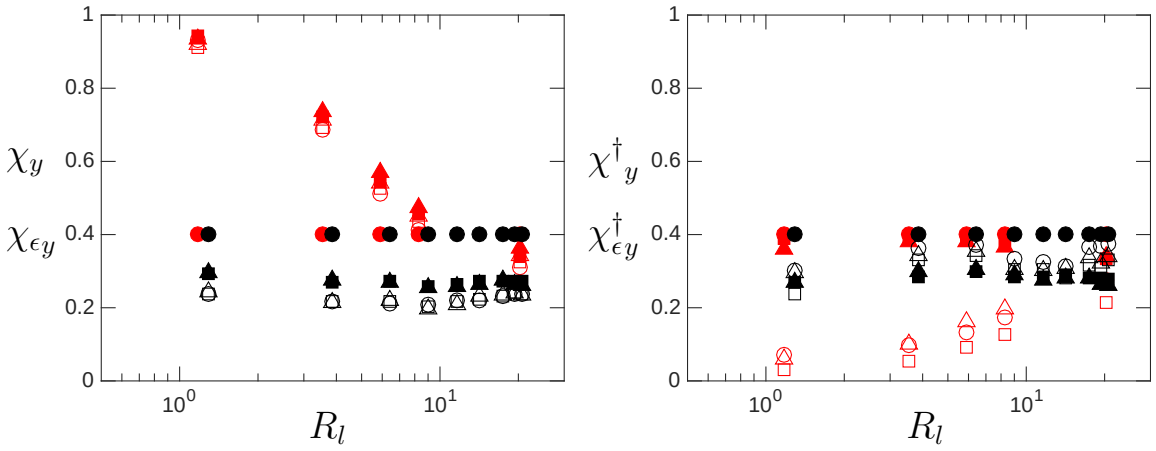

Figure IV.24. Ratio of dilatational to total velocity variance χ (open symbols) and ratio of dilatational dissipation to total dissipation χ_ϵ (closed symbols) for the total velocity field (left), and fluctuating velocity field (right). Different markers correspond to y locations, with $y = \pi$ (circles), 5π (squares), and 9π (triangles) for χ and $y =$ LICES (circles), $0.4\,L_y - 0.6\,L_y$ (squares), and $0.8\,L_y - L_y$ (triangles) for χ_ϵ . Colors correspond to $T_m = 1$ (black) and 20 (red).

When we compute the χ_ϵ using the fluctuating velocity, we find there is virtually no change compared to the total velocity if the temperature is low. This can be appreciated in Fig. IV.24 where it is hard to distinguish the difference between χ and $\chi^\dagger$. However, at large T_l we find that the large values of dilatational dissipation disappear and results are similar between low and high LICES temperature. Similar to χ, when we remove the time averaged velocity the effects of acoustics disappear

and we no longer have the large gradients caused by the Mach waves.

From Fig. IV.24, it is clear that at the location of the LICES the dilation introduced is independent of u_l and T_l. If we consider χ_ϵ computed using the total velocity, we can then see a similar trend as that χ, where it decreases with increasing R_l for the cases with high T_l, while there also seems to be a dip at intermediate R_l for the low T_l cases, although less pronounced than χ. On the other hand, dilatational dissipation behaves similarly for both low and high T_l when computed using the fluctuating velocity.

In summary, the heat release at the LICES has a first order effect on the evolution of both the kinetic and dissipation dilatational fields. Introducing large temperature favors dilatational motions at both the large and small scales. Introducing large temperature increases the strength of the Mach waves, which are purely dilatational motions. These can be weakened by increasing the velocity fluctuations. Upon removing the time averaged velocity field we find a qualitative change at both the large and small scales, as seen in Fig. IV.24. This demonstrates the strong effect of the transition of the flow towards fully developed turbulence.

IV.C. Conclusions

In this chapter we have investigated the possibility of creating turbulence from laser induced concentrated energy sources (LICES), inspired in the experimental use of lasers to photo-dissociated molecules. This mechanisms is intended to increase mixing in hypersonic combustion, where the harsh environment of combustors makes any other active method unpractical. We have modeled the velocity and temperature

fluctuations based on experimental observations of vibrationally excited nitric oxide (Sánchez-González *et al.*, 2012*a*,*b*), although the analysis may be adapted to other molecules.

We have performed a convergence study to quantify the error of mean kinetic energy and dissipation rate, strictly based on the way energy was introduced. We have defined a non dimensional resolution Reynolds number R_k which provides a function for the error of both quantities. R_k can be known a priori from initial conditions, and the error can be bounded by assuming $R_k < R_k^{\max}$.

As a first step in understanding the evolution of the flow, we analyzed the spreading rate of perturbations from a single LICES. To measure the turbulent fluctuations downstream, the stationary flow is removed by subtracting the time averaged velocity field. The perturbations downstream are then measured using Eq. (4.1). From a large database of simulations, seen in Table IV.1, it was determined that the time averaged spreading rate $d\delta/dy$ is a function of R_l and T_l, with an upper bound fixed by the local Mach angle $d\delta/dy \lesssim \sin^{-1}(1/M)$, which increases with T_l. It was also determined that at low R_l the normalized dissipation ψ is much larger than unity, which is typical of low Reynolds number (Sreenivasan, 1998). However, for the large R_l ψ becomes of order one, also consistent with the literature, and the spreading rate collapses with the Mach angle $d\delta/dy \sim \sin^{-1}(1/M)$.

Several statistics were used to determine the transition of the flow to fully developed turbulence. It was shown that for low T_l, the axial rms is approximately 2-4% larger than the transverse. Although there is a small degree of anisotropy at the large scales, it is close to an order of magnitude smaller than classical grid turbulence

(Comte-Bellot & Corrsin, 1966; Gad-el Hak & Corrsin, 1974; Mydlarski & Warhaft, 1996). For high T_l cases we can seen strong anisotropies as the major velocity perturbations are generated by the Mach waves behind the LICES. This effect decreases with R_l as the Mach waves are weakened by the velocity perturbations. The strong effect of acoustics when LICES temperature is large was validated by computing the same quantities with the fluctuating velocity field. The effect of acoustics, which is statistically stationary in time, disappears and the large scale anisotropies are no longer seen. The skewness of longitudinal velocity gradients was shown to approach the value for fully developed isotropic turbulence (Tavoularis *et al.*, 1978; Sreenivasan & Antonia, 1997) given three conditions are met: axial distance $y/d_l \gtrsim 5$, LICES Reynolds number $R_l \gtrsim 15$, and LICES temperature perturbations are withing 1% of the reference temperature $T_l/T_{\text{ref}} \lesssim 1\%$. At these conditions the transverse one-dimensional energy spectra collapses with isotropic turbulence under K41 scaling and we can claim universality of the small scales. Other conditions for generating turbulence at higher temperature perturbations are likely possible, yet the distance behind the grid and R_l will have to increase.

An important result from the analysis is that the Taylor Reynolds number scales with R_l. It was found to scale as $R_\lambda \sim R_l^{0.85}$, implying a weak power law. Finally, it was shown that adding temperature at the LICES has a first order effect on the dilatational motions, both of velocity and dissipation. For high T_l dilatation decreases with increasing R_l, while for low T_l it is relatively constant with a dip at $R_l \sim 10$.

In summary, we have shown that it is possible to create turbulence based on LICES, provided a Reynolds number based on initial conditions is high enough and

the additional temperature at the LICES is below 1%. We have also shown that if the velocity introduced at the LICES is sufficiently high, the anisotropic effect of the Mach waves is reduced. Therefore, we expect that turbulence at higher T_l is possible but would require significantly higher R_l, which is a computational challenge. Finally, we have found that is possible to predict the achievable R_λ based on the energy we introduce.

CHAPTER V

ISOTROPIC TURBULENCE IN THERMAL EQUILIBRIUM AND NON-EQUILIBRIUM

In this chapter we investigate the statistically steady states of turbulent flows when the vibrational molecular degree of freedom is excited. Unlike laminar flows in thermal non-equilibrium which relax asymptotically towards thermal equilibrium, turbulent flows present persistent departures from equilibrium. This is due to fluctuations in thermodynamic variables which are known to increase with turbulent Mach number $M_t = \sqrt(3)u'/c$, where c is the mean speed of sound. In turbulent flows, hydrodynamics as well as thermodynamic variables experience fluctuations over a wide range of scales and it is useful to split a variable f into mean and fluctuations, that is $f = \overline{f} + f'$ where an overbar is a suitably defined average and clearly $\overline{f'} = 0$. For simplicity in notation we will denote normalized fluctuations as $f^\dagger \equiv f'/\overline{f}$.

The analytical results in this section are derived in terms of temperature variance and temperature-density correlations. Depending on the type of forcing, these can be related to other parameters. For example for SF we have (Donzis & Jagannathan, 2013):

$$\begin{aligned} \overline{T^{\dagger 2}} &\approx A^2(\gamma-1)^2 M_t^4/9 \\ \overline{\rho^{\dagger 2}} &\approx A^2 M_t^4/9 \\ \overline{\rho^\dagger T^\dagger} &\approx A^2(\gamma-1) M_t^4/9, \end{aligned} \tag{5.1}$$

where A is a flow-dependent constant and γ is the ratio of specific heats.

When DF is applied, however, these relations are not valid but still fluctuations are found to be accurately described as isentropic or more generally as polytropic. Then (Donzis & Jagannathan, 2013):

$$\overline{\rho^{\dagger 2}} = \overline{T^{\dagger 2}}/(\gamma-1)^2$$
$$\overline{\rho^{\dagger} T^{\dagger}} = \overline{T^{\dagger 2}}/(\gamma-1). \tag{5.2}$$

(In what follows γ is understood as a polytropic exponent, with the isentropic case being a particular instance). Finally, when the energy equation is forced (i.e. EF), temperature and density fluctuations become more uncorrelated and it is not possible to identify a single parameter to represent their fluctuations.

To assess scaling with different parameters, a large database of 204 simulations has been generated. A summary of the parameter space and conditions covered by the simulations is shown in Table V.1.

V.A. Turbulence in thermal equilibrium

If we have a turbulent flow where vibrational energy is in complete thermal equilibrium, $e_v = e_v^*$ everywhere and at all times with e_v^* given by Eq. (2.25). Due to temperature fluctuations, we clearly have $\overline{e_v^*} \neq e_v^*(\overline{T})$ where $e_v^*(\overline{T})$ is Eq. (2.25) evaluated at $T = \overline{T}$. If one considers fluctuations around $e_v^*(\overline{T})$, using a Taylor expansion with spatial averages, Eq. (2.25) may be re-written as:

$$\frac{\overline{e_v^*} - e_v^*(\overline{T})}{e_v^*(\overline{T})} = g_T \overline{T^{\dagger 2}} \tag{5.3}$$
$$\approx A^2 g_M M_t^4 \tag{5.4}$$

Cases	R_λ	M_t	Forcing	N	c_2/T	k_T	k_τ
1-48	38	0.1	SF ($s=1$)	64	100-200	1,2,5,10	1,2,5,10,15,25
49-96	38	0.3	SF ($s=1$)	64	100-200	1,2,5,10	1,2,5,10,15,25
97-120	38	0.6	SF ($s=1$)	64	100	1,2,5,10	1,2,5,10,15,25
121-140	38	0.8	SF ($s=1$)	64	100	1,2,5,10	1,2,5,10,15
141-152	38	0.6	SF ($s=1$) +1.2 EF	64	100	1,10	1,2,5,10,15,25
153-164	38	0.6	SF ($s=1$) +1.6 EF	64	100	1,10	1,2,5,10,15,25
165-176	38	0.3	SF ($s=0.4$) + DF	128	100	1,10	1,2,5,10,15,25
187-188	60	0.3	SF ($s=1$)	128	100	1,10	1,2,5,10,15,25
189-196	100	0.1	SF ($s=1$)	256	100	1,10	1,2,5,10,15
197-204	100	0.3	SF ($s=1$)	256	100	1,10	1,2,5,10,15

Table V.1. All simulation run for isotropic turbulence with TNE including the type of forcing used and parameter space for each M_t and R_λ.

Where g_T is a function of the non-dimensional parameter:

$$K_T \equiv \frac{\theta_v}{\overline{T}} \tag{5.5}$$

and $g_M = g_T(\gamma-1)^2/9$. Eq. (5.4) is only valid for SF. The complete expression for g_T may be found in (Donzis & Maqui, 2016).

In Fig. V.1(a-b) we compare Eq. (5.3) and Eq. (5.4) with DNS data where averages are taken over space as typically done in isotropic simulations (**?**). In part (a) we see very good agreement except for DF and EF cases, which is not unexpected since the relation used between temperature fluctuations and M_t is only valid for SF.

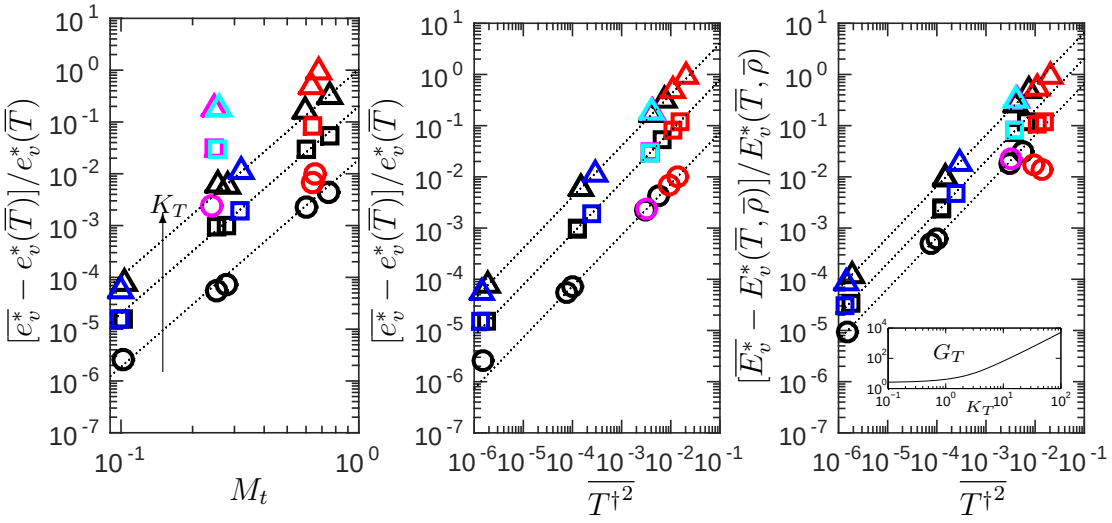

Figure V.1. Effect of temperature fluctuations on mean vibrational energy in thermal equilibrium per unit mass (a-b) and per unit volume (c). Circles, squares and triangles correspond to $K_T = 2$, 5 and 10 respectively. Black, magenta, red and cyan are for SF, DF, SF+EF and DF+EF, respectively. Blue symbols are for $R_\lambda \sim 100$. For present simulations $A = 1.2$, $\gamma = 1.4$.

All cases collapse when data are cast in terms of temperature fluctuations (part b). The general expression in terms of $\overline{T^{\dagger 2}}$ holds independently of the physical mechanism responsible for these temperature fluctuations. We also note that while the Mach number dependence is strong, Reynolds number effects are very weak. This is not unexpected since temperature fluctuations are known to be strongly affected by M_t but only weakly affected by R_λ (Donzis & Jagannathan, 2013).

A similar development can be done for the vibrational energy per unit volume $E_v^* \equiv \rho e_v^*$. The relevance of this quantity can be seen readily in the context of our simulations where the average is essentially an integration over the volume (divided by a constant), that is the total vibrational energy in the domain. When Eq. (2.25) is multiplied by ρ, the Taylor expansion now involves fluctuations in both temperature and density. Again, using Eq. (2.25) and averaging, we can rearrange the final

expression which, to leading order, is

$$\frac{\overline{E_v^*} - E_v^*(\overline{T}, \overline{\rho})}{E_v^*(\overline{T}, \overline{\rho})} = g_T \, \overline{T^{\dagger 2}} + g_{\rho T} \, \overline{\rho^\dagger T^\dagger} \tag{5.6}$$

$$\approx G_T \, \overline{T^{\dagger 2}} \tag{5.7}$$

where again $g_{\rho T}$ is just a function of K_T and $G_T = g_T + g_{\rho T}/(\gamma - 1)$. This expression may also be re-rewritten solely in terms of M_t for SF. Details on the expressions may be found in (Donzis & Maqui, 2016).

The good agreement between Eq. (5.7) and the DNS with SF and DF forcings is shown in Fig. V.1c. It is readily verified that at low and high values of K_T the dominant contribution comes from the $g_{\rho T}$ and g_T terms respectively. Thus, it is also seen that the EF cases, which are dominated by temperature fluctuations, also become a better approximation at high K_T as the magnitude of $g_{\rho T}$ becomes relatively small.

An interesting consequence of Eq. (5.7) is that since G_T is always positive, then $\overline{E_v^*} > E_v^*(\overline{T})$. This means that the total energy in the vibrational mode will always be larger when fluctuations of thermodynamic variables are present, even if the flow is in complete thermal equilibrium. Alternatively, this implies that in order to maintain the same mean temperature (translational-rotational energy) a turbulent flow will store more energy in the vibrational mode than its non-fluctuating (laminar) counterpart. This result is a consequence of the specific non-linear dependence of the equilibrium vibrational energy with temperature Eq. (2.25) when this mode is partially excited.

We now turn to the relative contribution of vibrational to translational-rotational

energy. For laminar flows in thermal equilibrium this is well known:

$$\frac{E_v^*(\overline{T},\overline{\rho})}{E(\overline{T},\overline{\rho})} = \frac{2K_T}{5(\beta-1)}. \tag{5.8}$$

Because of the different effect of fluctuations of thermodynamic variables on different energy modes, we expect the distribution of energy to depend on these fluctuations. For example, the ratio of the average vibrational to translational-rotational energy, both in thermodynamic equilibrium, can be written, using Eq. (5.6) and $\overline{E} = E(\overline{T},\overline{\rho})(1+\overline{\rho^\dagger T^\dagger})$ (which results from decomposing $E = \rho(5/2)RT$ into mean and fluctuations), as

$$\frac{\overline{E_v^*}}{\overline{E}} \approx \frac{E_v^*(\overline{T},\overline{\rho})}{E(\overline{T},\overline{\rho})} \frac{1+G_T\overline{T^{\dagger 2}}}{1+\overline{T^{\dagger 2}}/(\gamma-1)} \tag{5.9}$$

where as before the last expression corresponds to polytropic fluctuations. The good agreement between this expression and DNS is shown in Fig. V.2 as we compare open circles (DNS) with Eq. (5.9) as dashed lines. From the figure we can see a transition from low to high temperature fluctuations. In particular, from Eq. (5.9), we can define the turbulent-to-laminar ratio of the relative contribution of vibrational energy as

$$r_v^* \equiv \frac{\overline{E_v^*}/\overline{E}}{E_v^*(\overline{T},\overline{\rho})/E(\overline{T},\overline{\rho})} \tag{5.10}$$

which measures the effect of turbulence on the distribution of energy across vibrational and translational-rotational modes. It is readily shown from Eq. (5.9) that r_v^* tends to 1 and $(\gamma-1)G_T$ for low and high levels of temperature fluctuations $\overline{T^{\dagger 2}}$ (or M_t) respectively. However, the expansion in the numerator of Eq. (5.9) contains only the leading order term. Higher order terms will become important at, for example, higher M_t where thermodynamic fluctuations may follow a log-normal

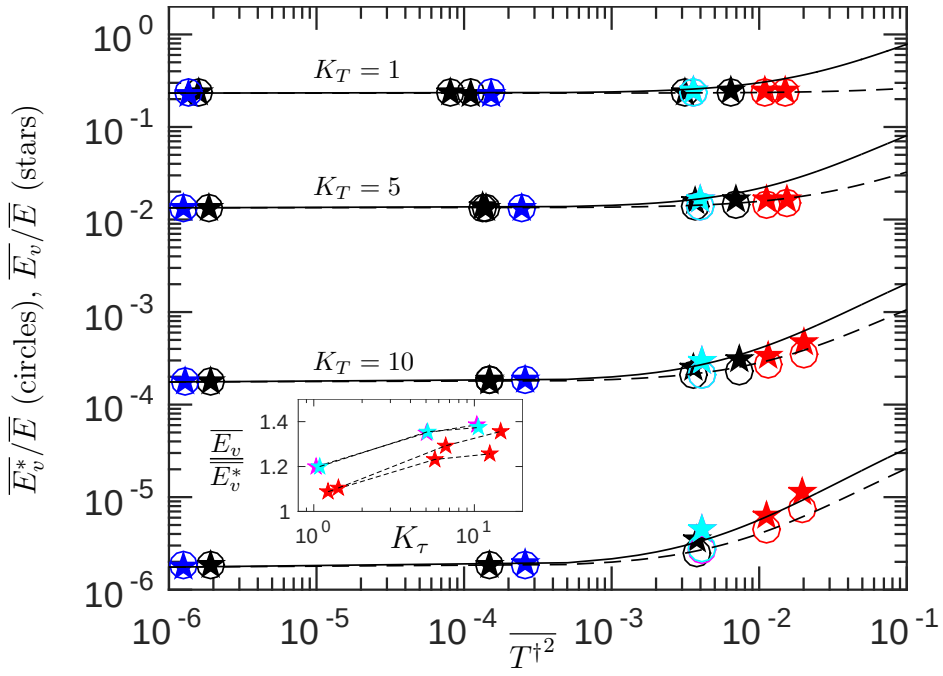

Figure V.2. Ratio of average equilibrium vibrational and translational-rotational energy. Dashed lines (Eq. (5.9)) and open circles (DNS) are for $\overline{E_v^*}/\overline{E}$. Solid lines (Eq. (5.16)) and closed stars (DNS with $K_\tau = 10$) are for $\overline{E_v}/\overline{E}$. From top to bottom, $K_T = 1$, 5, 10 and 15 respectively. Same colors as in Fig. V.1. Inset: variation of $\overline{E_v}/\overline{E_v^*}$ with K_τ for fixed $\overline{T^{\dagger 2}} \approx 10^{-2}$ and $K_T = 10$.

distribution (Blaisdell *et al.*, 1993; Donzis & Jagannathan, 2013). In any case, we can see that as M_t increases, a larger fraction of the available energy will be stored in vibrational modes when the mean temperature of the flow is kept constant. Even if higher order terms are included, r_v^* may still plateau at intermediate Mach numbers since the denominator is a second order polynomial without any approximation.

V.B. Turbulence in thermal non-equilibrium

We now turn to the situation where thermal equilibrium is not achieved instantaneously, that is TNE. This is known to be the case, for example, in the laminar

flow behind a strong shock where translational and rotational energy quickly reach equilibrium but vibration, associated with much larger time scales (Rich & Treanor, 1970), attains equilibrium only after a relatively long period of time. This relaxation process can also be studied in molecular simulations (Liao *et al.*, 2010; **?**) as well as experiments (Fuller *et al.*, 2014).

Turbulent flows possess a wide range of time scales. The most rapid fluctuations in a turbulent flow are associated with the so-called Kolmogorov time scale (**?**) $\tau_\eta \equiv (\nu/\langle\epsilon\rangle)^{1/2}$ where ν is the mean kinematic viscosity and $\langle\epsilon\rangle$ the mean energy dissipation rate. Since the Prandtl number in the simulations is of order one, the smallest scales for the temperature field are expected to operate at a time scale comparable to τ_η (Monin & Yaglom, 1975). Thus, an important non-dimensional parameter to characterize the relaxation process is the ratio

$$K_\tau \equiv \tau_v/\tau_\eta \tag{5.11}$$

To obtain a specific value K_τ in our simulations, we adjust the constant $c_1^{\tau_v}$. The value of $c_2^{\tau_v}$ is taken to be about two orders of magnitudes larger than $\overline{T}$ (that is $K_{c2} \equiv c_2^{\tau_v}/\overline{T} \sim O(10^2)$) which is not uncommon in real flows with TNE (e.g. air at temperatures of $O(10^3)$ degrees Kelvin). The conclusions below, though, do not depend strongly on the specific value of K_{c2}.

If Eq. (2.23) is averaged, then, for a stationary, homogeneous flow, the entire left-hand-side as well as transport terms on the right-hand-side vanish. The result is

$$\overline{E_v/\tau_v} = \overline{E_v^*/\tau_v}. \tag{5.12}$$

This expression represents a general statement on the nature of statistically stationary states for turbulence in TNE under the assumptions which make Eq. (2.23) valid.

We have verified Eq. (5.12) against DNS data within statistical error.

We can expand the right-hand-side of Eq. (5.12) in T and ρ as before. The result, to leading order, is

$$\overline{E_v/\tau_v} \approx \frac{E_v^*(\overline{T},\overline{\rho})}{\tau_v(\overline{T},\overline{p})}\left(1+H_T\overline{T^{\dagger 2}}\right), \tag{5.13}$$

where H_T is a function of K_T and K_{c2} for polytropic fluctuations. The generalized formula along with details on the expression may be found in (Donzis & Maqui, 2016).

However, while Eq. (5.12) and Eq. (5.13) describe the nature of steady states from the governing equations through the correlation $\overline{E_v/\tau_v}$, our interest is in the behavior of the vibrational energy itself. Based on the parameter K_τ we can distinguish two asymptotic regimes, namely, fast and slow relaxation.

*Fast TNE relaxation.*If $K_\tau \ll 1$, then vibrational relaxation is much faster than any other hydrodynamically relevant time scale. We would then expect fluid elements to attain thermal equilibrium almost instantaneously which implies $\overline{E_v} \approx \overline{E_v^*}$.

Slow TNE relaxation. If $K_\tau \gg 1$, then the last term in Eq. (2.23) will be small. The evolution towards equilibrium will be slow and fluctuations of translational temperature will not have an immediate effect on e_v. Unlike the case of very rapid equilibration ($K_\tau \ll 1$), E_v may be only weakly correlated to $T^\dagger$ and one may expect

$$\overline{E_v {\tau_v}^{-1}} \approx \overline{E_v}\ \overline{{\tau_v}^{-1}}. \tag{5.14}$$

Combining with Eq. (5.13) we find

$$\overline{E_v} \approx E_v^*(\overline{T},\overline{\rho})\frac{\tau_v(\overline{T},\pm)^{-1}}{\overline{{\tau_v}^{-1}}}\left(1+H_T\overline{T^{\dagger 2}}\right). \tag{5.15}$$

The ratio of vibrational relaxation times can also be expanded in Taylor series yielding $\overline{\tau_v^{-1}}/\tau_v(\overline{T},\pm)^{-1} \approx 1 + L_T\overline{T^{\dagger 2}}$ with $L_T = K_{c2}^{1/3}(K_{c2}^{1/3} - 4)/18$.

Combining results we obtain

$$\frac{\overline{E_v}}{\overline{E}} \approx \frac{E_v^*(\overline{T},\overline{\rho})}{E(\overline{T},\overline{\rho})} \frac{1 + H_T\overline{T^{\dagger 2}}}{\left(1 + L_T\overline{T^{\dagger 2}}\right)\left(1 + \overline{T^{\dagger 2}}/(\gamma - 1)\right)}. \tag{5.16}$$

In Fig. V.2 we compare DNS data (solid stars) with Eq. (5.16) (solid lines) where we also see very good agreement especially at high K_T. At low K_T, higher values of K_τ (i.e. longer relaxation times) lead to increasingly better agreement. We can also define a ratio $r_v = (\overline{E_v}/\overline{E})/(E_v^*(\overline{T},\overline{\rho})/E(\overline{T},\overline{\rho}))$ to quantify departures in energy distribution due to turbulence. Like r_v^*, the ratio r_v grows as temperature fluctuations become stronger (Fig. V.2). At much higher fluctuations, however, higher order terms are needed in Eq. (5.16).

Note that the dashed and solid lines represent the limits $K_\tau \to 0$ and $K_\tau \to \infty$ respectively. Intermediate conditions are expected to fall between these two lines. The inset of the figure illustrates this, where the ratio of $\overline{E_v}/\overline{E_v^*}$ approaches unity at low K_τ but increases at high K_τ. The conclusion here is again that turbulent flows will store more energy in vibrational modes (even more than in complete thermal equilibrium) than its laminar counterpart at the same mean temperature.

V.C. Conclusions

The strongly non-linear nature of partially excited vibrational energy with temperature, as described by quantum mechanics, results in steady states for turbulent flows which depart from its nonfluctuating counterparts. In particular, when the mean translational temperature is the same, turbulent flows store a larger fraction

of energy in vibration than flows without temperature fluctuations. This is the case in situations when there is complete thermal equilibrium as well as situations with TNE. However, the degree of the departure is stronger for the latter. This phenomenon may be used, for example, to control heat transfer to surfaces in supersonic vehicles by taking advantage of the increased energy stored in vibrational, instead of translational modes, as turbulent fluctuations increase. Quantifying the effect of turbulence on the mean vibrational energy can also be valuable in interpreting averaged experimental results of this energy mode.

CHAPTER VI

CONCLUSIONS AND FUTURE WORK

VI.A. Conclusions

Generating turbulence at supersonic speeds with thermal non-equilibrium (TNE) is an extremely difficult, yet desired problem. In the present work we examine a new idea to generate these conditions in a controlled experimental environment and assess whether such an approach is feasible. This new concept involves localized concentrated energy sources, which can be introduced by laser-induced photo-dissociation of molecules, and evolve to eventually trigger the establishment of turbulence. To understand the main mechanisms leading towards the development of turbulence, incompressible simulations with concentrated kinetic energy sources were used. These allowed us to investigate the fundamental hydrodynamic process shortly after photo-excitation, when thermodynamic variables have reached equilibrium and the flow can be considered isotropic.

Based on several statistics commonly used to describe turbulent flows we have found laser induced kinetic energy sources (LIKES) are a feasible mechanisms for generating turbulence given the Reynolds number based on initial conditions is sufficiently high, $R_I > 400$, and enough time has elapsed, $t > 2\tau^*$. At these conditions, the skewness of velocity gradients and ratio of rms velocities is consistent with grid turbulence at similar Reynolds number (Tavoularis *et al.*, 1978; Sreenivasan & Antonia, 1997), and the spectra collapses under K41 normalization. It has also been

shown that the second and third invariants agree well with grid generated turbulence passed through a contraction (Choi & Lumley, 2001; Le Penven *et al.*, 1985; Tucker & Reynolds, 1968), given the similarities of the initial conditions. From an analysis using radial statistics, we have shown that, in the proximity of the LIKES, convection dominates and that there is a qualitative change from vortex squeezing to stretching as the flow evolves in time. It is also found that both the characteristic time scale τ^* and the Taylor Reynolds number scale with R_I. This is an important result provided we can predict the highest achievable R_λ, as well as the transition to turbulence from the initial conditions.

Upon having understood the main mechanisms which generate turbulence from concentrated energy sources, the more complex compressible scenario, where we have fluctuations in thermodynamic and hydrodynamic variables, was studied. These are laser induced concentrated energy sources (LICES). Again, based on the skewness of velocity gradients, ratio of rms velocities, and energy spectra we have found LICES to be feasible mechanism for generating turbulence, given the right set of conditions are posed, which in this case is reduce to: high R_l, and low T_l. The Taylor Reynolds number is found to scale with R_l, providing a tool for predicting the R_λ based on the energy introduced. Results show a strong effect of heat release on the development of turbulence. Increasing temperature at the LICES increases dilatational motions which inhibit or delay the transition to turbulence.

Finally, the effects of TNE have been studied in isotropic turbulence. It has been showed that turbulent flows store a larger fraction of energy in vibration than laminar flows. This is the case for flows in thermal equilibrium as well as thermal

non-equilibrium, although the fraction can be larger for the latter.

In summary, we have shown that it is possible to generate turbulence from concentrated sources of energy, such as those of laser induced photo-dissociation molecules. The numerical study presented provides the parameters used to design turbulence experiments at hypersonic speeds. This will allow for the fundamental understanding of turbulence in hypersonic speeds, where more complex physics such as TNE may be present. These parameters can also be used for the development of new technologies for increased mixing in the combustion of hypersonic vehicles.

VI.B. Future research directions

In this section we discuss possible extensions to the current work.

- Although the fundamental aspects of LICES generated turbulence have been studied, there is still a large number of parameters that offer greater control on the characteristics of the generated turbulence. For example we would also like to explore the effect of the different distributions, distance between LICES, and other geometrical considerations that could affect the transition to turbulence.

- Although we expect that turbulence can be generated at higher T_l, we wish to verify this claim through numerical experiments. Furthermore, we would like to predict the distance at which the flow will transition to turbulence. This distance would be the analogous to τ^* in the simulations of incompressible LIKES. Characterizing this distance could provide valuable information to the design of a well controlled experimental configurations for shock turbulence interactions.

- The next step in complexity is to study the effect of TNE in controlled conditions. Ideally we would like to have LICES with TNE and control energy distributions (translational, rotational, vibrational). With a carefully designed LICES grid one can create a mean E_v gradient in the transverse direction to understand the evolution of E_v. Other simplified configurations could involve turbulence boundary layer with TNE, or other simple transition flows.

- Another potential implementation of the LICES technique is for relaminarization of flows. We have shown that introducing large temperature at the LICES delays or inhibits the transition to turbulence. It is of practical importance to understand if an already turbulent flow can be relaminarized through LICES. This could be an extremely useful tool for systems where turbulence noise is detrimental to the functionality of the system. It could also have practical applications to reduce drag or dynamically control flows. For example, LICES could be applied at the exit of a combustion chamber to relamizarize the flow and improve the efficiency of the exhaust process.

- A large number of scripts have been developed to automatize the process in which simulations are run. To make these more user friendly, a collaboration between our group and XSEDE was established. The main objective of this collaboration is to create a framework to run simulations and post processing on different supercomputers from our local machines, without requiring advance knowledge of the codes or supercomputing. An automatic workflow was successfully created to run the main simulation but achieving dynamic workflows of post processing is still a work in progress. Building the tools to perform DNS

in a user friendly fashion would be beneficial to the entire scientific community.

REFERENCES

Antonia, R. A., Djenidi, L. & Spalart, P. R. 1994 Anisotropy of the dissipation tensor in a turbulent boundary layer. *Physics of Fluids* **6**, 2475.

Bertolotti, F. P. 1998 The influence of rotational and vibrational energy relaxation on boundary-layer stability. *Journal of Fluid Mechanics* **372**, 93–118.

Birch, S.F. & Eggers, J.M. 1972 A critical review of the experimental data for developed free turbulent shear layers. *Free Turbulent Shear Flows, Volume I, ConferenceProceedings, NASA, SP-321* pp. 11–40.

Blaisdell, G. A., Mansour, N. N. & Reynolds, W. C. 1993 Compressibility effects on the growth and structure of homogeneous turbulent shear-flow. *Journal of Fluid Mechanics* **256**, 443–485.

Blaisdell, G. A., Spyropoulos, E. T. & Qin, J. H. 1996 The effect of the formulation of nonlinear terms on aliasing errors in spectral methods. *Applied Numerical Math* **21** (3), 207–219.

Bogdanoff, David W 1994 Advanced injection and mixing techniques for scramjet combustors. *Journal of Propulsion and Power* **10** (2), 183–190.

Booth, JP, Azamoum, Y, Sirse, N & Chabert, P 2012 Absolute atomic chlorine densities in a cl2 inductively coupled plasma determined by two-photon laser-induced fluorescence with a new calibration method. *Journal of Physics D: Applied Physics* **45** (19), 195201.

Briassulis, G, Agui, JH & Andreopoulos, Y 2001 The structure of weakly compressible grid-generated turbulence. *Journal of Fluid Mechanics* **432**, 219–283.

Buckmaster, John, Jackson, Thomas L & Kumar, Ajay 2012 Combustion in high-speed flows.

Choi, K.S. & Lumley, J. L. 2001 The return to isotropy of homogeneous turbulence. *Journal of Fluid Mechanics* **436** (1), 59–84.

Comte-Bellot, G. & Corrsin, S. 1966 Use of a contraction to improve isotropy of grid-generated turbulence. *Journal of Fluid Mechanics* **25** (Part 4), 657–682.

Corrsin, S. 1963 Turbulence: experimental methods. *Handbuch der Physik* **8**, 524.

Curran, ET, Heiser, WH & Pratt, DT 1996 Fluid phenomena in scramjet combustion systems. *Annual Review of Fluid Mechanics* **28** (1), 323–360.

De Silva, IPD & Fernando, HJS 1994 Oscillating grids as a source of nearly isotropic turbulence. *Physics of Fluids* **6** (7), 2455–2464.

Dimotakis, P. E. 2005 Turbulent mixing. *Annual Review of Fluid Mechanics* **37**, 329–356.

Dixon, RN 1986 The determination of the vector correlation between photofragment rotational and translational motions from the analysis of doppler-broadened spectral line profiles. *The Journal of Chemical Physics* **85** (4), 1866–1879.

Donzis, D. A. 2012 Amplification factors in shock-turbulence interactions: effect of shock thickness. *Physics of Fluids* **24**, 011705.

Donzis, D. A. & Jagannathan, S. 2013 Fluctuations of thermodynamic variables in stationary compressible turbulence. *Journal of Fluid Mechanics* **733**, 221–244.

Donzis, D. A. & Maqui, A. F. 2016 Statistically steady states of forced isotropic turbulence in thermal equilibrium and non-equilibrium. *Physics of Fluids* **(under review)**.

Donzis, D. A. & Sreenivasan, K. R. 2010*a* The bottleneck effect and the Kolmogorov constant in isotropic turbulence. *Journal of Fluid Mechanics* **657**, 171–188.

Donzis, D. A. & Sreenivasan, K. R. 2010*b* Short-term forecasts and scaling of intense events in turbulence. *Journal of Fluid Mechanics* **647**, 13–26.

Donzis, D. A., Sreenivasan, K. R. & Yeung, P. K. 2005 Scalar dissipation rate and dissipative anomaly in isotropic turbulence. *Journal of Fluid Mechanics* **532**, 199–216.

Ducros, F., Laporte, F., Soulres, T., Guinot, V., Moinat, P. & Caruelle, B. 2000 High-order fluxes for conservative skew-symmetric-like schemes in structured meshes: Application to compressible flows. *Journal of Computational Physics* **161** (1), 114–139.

Dugger, Gordon L 1961 Comparison of hypersonic ramjet engines with subsonic and supersonic combustion. *High Mach Number Air-breathing Engines.* Pergamon, Oxford, U.K., 1961 .

Eswaran, V. & Pope, S. B. 1988 An examination of forcing in direct: numerical simulations of turbulence. *Computers & Fluids* **16**, 257–278.

Ferri, Antonio 1960 Possible directions of future research in air-breathing engines. In *AGARD Combustion and Propulsion Colloquium*, pp. 3–15. Pergamon, London.

Ferri, Antonio 1973 Mixing-controlled supersonic combustion. *Annual Review of Fluid Mechanics* **5** (1), 301–338.

Fuller, Timothy J, Hsu, Andrea G, Sanchez-Gonzalez, Rodrigo, Dean, Jacob C, North, Simon W & Bowersox, Rodney DW 2014 Radiofrequency plasma stabilization of a low-reynolds-number channel flow. *Journal of Fluid Mechanics* **748**, 663–691.

Geckinli, Nezih C & Yavuz, Davras 1978 Some novel windows and a concise tutorial comparison of window families. *Acoustics, Speech and Signal Processing, IEEE Transactions on* **26** (6), 501–507.

Gence, Jean Noel 1983 Homogeneous turbulence. *Annual Review of Fluid Mechanics* **15** (1), 201–222.

Gibson, C.H. & Schwarz, W.H. 1963 The universal equilibrium spectra of turbulent velocity and scalar fields. *Journal of Fluid Mechanics* **16** (03), 365–384.

Goebel, Steven G & Dutton, J Craig 1991 Experimental study of compressible turbulent mixing layers. *AIAA Journal* **29** (4), 538–546.

Gorski, Joseph J, Wallace, James M & Bernard, Peter S 1994 The enstrophy equation budget of bounded turbulent shear flows. *Physics of Fluids (1994-present)* **6** (9), 3197–3199.

Gotoh, G., Fukayama, D. & Nakano, T. 2002 Velocity field statistics in homogeneous steady turbulence obtained using a high-resolution direct numerical simulation. *Physics of Fluids* **14**, 1065–1081.

Grant, HL & Nisbet, ICT 1957 The inhomogeneity of grid turbulence. *Journal of Fluid Mechanics* **2**, 263.

Grosch, Chester E, Seiner, JM, Hussaini, MY & Jackson, TL 1997 Numerical simulation of mixing enhancement in a hot supersonic jet. *Physics of Fluids (1994-present)* **9** (4), 1125–1143.

Gutmark, EJ, Schadow, C & Yu, KH 1995 Mixing enhancement in supersonic free shear flows. *Annual Review of Fluid Mechanics* **27** (1), 375–417.

Gad-el Hak, M. & Corrsin, S. 1974 Measurements of the nearly isotropic turbulence behind a uniform jet grid. *Journal of Fluid Mechanics* **62** (1), 115–143.

Harris, Fredric J 1978 On the use of windows for harmonic analysis with the discrete fourier transform. *Proceedings of the IEEE* **66** (1), 51–83.

Hideharu, M. 1991 Realization of a large-scale turbulence field in a small wind tunnel. *Fluid Dynamics Research* **8** (1), 53–64.

Hinze, JO 1959 Turbulence: An introduction to its mechanisms and theory.

Hirschfelder, J. O., Curtiss, C. F. & Bird, R. B. 1954 *Molecular Theory of Gases and Liquids*. New York: Wiley.

Honkan, A & Andreopoulos, J 1992 Rapid compression of grid-generated turbulence by a moving shock wave. *Physics of Fluids A: Fluid Dynamics (1989-1993)* **4** (11), 2562–2572.

Honkan, A, Watkins, CB & Andreopoulos, J 1994 Experimental study of interactions of shock wave with free-stream turbulence. *Journal of Fluids Engineering* **116** (4), 763–769.

Houston, Paul L 1987 Vector correlations in photodissociation dynamics. *Journal of Physical Chemistry* **91** (21), 5388–5397.

Hsu, Andrea G, Srinivasan, Ravi, Bowersox, Rodney DW & North, Simon W 2009*a* Two-component molecular tagging velocimetry utilizing *no* fluorescence lifetime and no_2 photodissociation techniques in an underexpanded jet flowfield. *Applied Optics* **48** (22), 4414–4423.

Hsu, Andrea G, Srinivasan, Ravi, W. Bowersox, Rodney D & North, Simon W 2009*b* Molecular tagging using vibrationally excited nitric oxide in an underexpanded jet flowfield. *AIAA Journal* **47** (11), 2597–2604.

Jagannathan, S. & Donzis, D.A. 2012 Massively parallel direct numerical simulations of forced compressible turbulence: a hybrid mpi/openmp approach. In *Proceedings of the 1st Conference of the Extreme Science and Engineering Discov-*

ery Environment: Bridging from the eXtreme to the campus and beyond, p. 23. ACM.

Jagannathan, S. & Donzis, D. A. 2015 Reynolds number scaling of compressible turbulence using high-resolution direct numerical simulations. *Journal of Fluid Mechanics* **(under review)**.

Kellogg, R.M. & Corrsin, S. 1980 Evolution of a spectrally local disturbance in grid-generated, nearly isotropic turbulence. *Journal of Fluid Mechanics* **96**, 641–669.

Kumar, Ajay, Bushnell, Dennis M & Hussaini, M Yousuff 1989 Mixing augmentation technique for hypervelocity scramjets. *Journal of Propulsion and Power* **5** (5), 514–522.

Ladeinde, F., Cai, X. & Alabi, A. 2009 A critical review of scramjet combustion simulation. In *47th AIAA Aerospace Sciences Meeting, AIAA Paper 2009* **127**. AIAA, Orlando, FL, Jan. 2009.

Landau, L. & Teller, E. 1936 Theory of sound dispersion. *Physik Z. Sowjetunion* **10**, 34.

Le Penven, L, Gence, JN & Comte-Bellot, G 1985 On the approach to isotropy of homogeneous turbulence: Effect of the partition of kinetic energy among the velocity components. In *Frontiers in Fluid Mechanics*, pp. 1–21. Springer.

Lee, K. & Girimaji, S. S 2013 Flow-thermodynamics interactions in decaying anisotropic compressible turbulence with imposed temperature fluctuations. *Theoretical and Computational Fluid Dynamics* **27** (1-2), 115–131.

Lee, S., Lele, S. K. & Moin, P. 1991 Eddy shocklets in decaying compressible turbulence. *Physics of Fluids* **3**, 657–664.

Lee, S., Lele, S. K. & Moin, P. 1997 Interaction of isotropic turbulence with shock waves: effect of shock strength. *Journal of Fluid Mechanics* **340**, 225–247.

Lele, S. K. 1989 Direct numerical simulation of compressible free shear flows. *AIAA Paper* **374**.

Lele, S. K. 1992 Compact finite-difference schemes with spectral-like resolution. *Journal of Computational Physics* **103**, 16–42.

Lele, S. K. 1994 Compressibility effects on turbulence. *Annual Review of Fluid Mechanics* **26**, 211–254.

Liao, W., Peng, Y. & Luo, L. S. 2010 Effects of multitemperature nonequilibrium on compressible homogeneous turbulence. *Physical Review E* **81**, 046704.

Lin, CC. 1987 On taylor's hypothesis and the acceleration terms in the navier-stokes equations. *Selected Papers of CC Lin: Fluid Mechanics and Applied Mathematics* **1** (4), 154.

Liu, K. & Pletcher, R. H. 2008 Anisotropy of a turbulent boundary layer. *Journal of Turbulence* (9), N18.

Lumley, J. L. 1978 Computational modeling of turbulent flows. *Advances in Applied Mechanics* **18** (123), 213.

Lumley, J. L. & Newman, G. R. 1977 The return to isotropy of homogeneous turbulence. *Journal of Fluid Mechanics* **82** (1), 161–178.

Mahesh, K., Lele, S. K. & Moin, P. 1997 The influence of entropy fluctuations on the interaction of turbulence with a shock wave. *Journal of Fluid Mechanics* **334**, 353–379.

Mansour, NN, Kim, J & Moin, P 1988 Reynolds-stress and dissipation-rate budgets in a turbulent channel flow. *Journal of Fluid Mechanics* **194**, 15–44.

Masaki, M & Yakura, J 1969 Transitional boundary-layer considerations for the heating analyses of lifting re-entry vehicles. *Journal of Spacecraft and Rockets* **6** (9), 1048–1053.

Mathieu, J. & Alcaraz, E. 1965 Rélisation d'une soufflerie á baut niveau de turbulence. *Comptes Rendus* **261**, 2435.

Menon, S 1989 Shock-wave-induced mixing enhancement in scramjet combustors. In *27th AIAA Aerospace Sciences Meeting* **1**. Reno, NV.

Mohsen, S 1990 The decay power law in grid-generated turbulence. *Journal of Fluid Mechanics* **219**, 195–214.

Monin, A. S. & Yaglom, A. M. 1975 Statistical fluid mechanics.

Morris, Philip J, Giridharan, Manampathy G & Lilley, Geoffrey M 1990 On the turbulent mixing of compressible free shear layers. In *Proceedings of*

the Royal Society of London A: Mathematical, Physical and Engineering Sciences **431**, pp. 219–243. The Royal Society.

Mydlarski, L. & Warhaft, Z. 1996 On the onset of high-reynolds-number grid-generated wind tunnel turbulence. *Journal of Fluid Mechanics* **320**, 331–368.

North, Simon W & Hall, Gregory E 1997 Vector and scalar correlations in statistical dissociation: The photodissociation of nccn at 193 nm. *The Journal of Chemical Physics* **106** (1), 60–76.

North, Simon W, Marr, Andrew J, Furlan, Alan & Hall, Gregory E 1997 Nonintuitive asymmetry in the three-body photodissociation of ch3cocn. *The Journal of Physical Chemistry A* **101** (49), 9224–9232.

Olejniczak, J. & Candler, G. V. 1995 Vibrational-energy conservation with vibration-dissociation coupling - general-theory and numerical-studies. *Physics of Fluids* **7** (7), 1764–1774.

Petersen, M. R. & Livescu, D. 2010 Forcing for statistically stationary compressible isotropic turbulence. *Physics of Fluids* **22**, 116101.

Pope, S. B. 2000 Turbulent flows.

Prandtl, L. 1932 *Herstellung Einwandfreier Luftströme (Windkanäle)*. Akademische Verlagsgesellschaft MBH.

Ribner, H. S. 1954 Shock-turbulence interaction and the generation of noise. *NACA TN-3255* .

Rich, J. W., Macheret, S. O. & Adamovich, I. V. 1996 Aerothermodynamics of vibrationally nonequilibrium gases. *Experimental Thermal and Fluid Science* **13** (1), 1–10.

Rich, J. W. & Treanor, C. E. 1970 Vibrational relaxation in gas-dynamic flows. *Annual Review of Fluid Mechanics* **2**, 355–396.

Rogallo, R. S. 1981 Numerical experiments in homogeneous turbulence p. NASA Tech. Memo. 81315.

Rogers, R Clayton, Capriotti, Diego P & Guy, R Wayne 1998 Experimental supersonic combustion research at nasa langley. *AIAA Paper* **98**, 2506.

Sagaut, P. & Cambon, C. 2008 Homogeneous turbulence dynamics.

Sánchez-González, Rodrigo, Bowersox, Rodney DW & North, Simon W 2012*a* Simultaneous velocity and temperature measurements in gaseous flowfields using the vibrationally excited nitric oxide monitoring technique: a comprehensive study. *Applied Optics* **51** (9), 1216–1228.

Sánchez-González, Rodrigo, Srinivasan, Ravi, Bowersox, Rodney DW & North, Simon W 2011 Simultaneous velocity and temperature measurements in gaseous flow fields using the venom technique. *Optics Letters* **36** (2), 196–198.

Sánchez-González, Rodrigo, Srinivasan, Ravi, Hofferth, Jerrod, Kim, Do Yong, Tindall, Andrew J, W. Bowersox, Rodney D & North, Simon W 2012*b* Repetitively pulsed hypersonic flow apparatus for diagnostic development. *AIAA Journal* **50** (3), 691–697.

Seiner, John M, Dash, SM & Kenzakowski, DC 2001 Historical survey on enhanced mixing in scramjet engines. *Journal of Propulsion and Power* **17** (6), 1273–1286.

Shy, SS, Tang, CY & Fann, SY 1997 A nearly isotropic turbulence generated by a pair of vibrating grids. *Experimental Thermal and Fluid Science* **14** (3), 251–262.

Simmons, LFG & Salter, C. 1934 Experimental investigation and analysis of the velocity variations in turbulent flow. *Proceedings of the Royal Society of London. Series A* **145** (854), 212–234.

Sinhuber, Michael, Bodenschatz, Eberhard & Bewley, Gregory P 2015 Decay of turbulence at high reynolds numbers. *Physical Review Letters* **114** (3), 034501.

Sreenivasan, K. R. 1984 On the scaling of the turbulence energy-dissipation rate. *Physics of Fluids* **27**, 1048–1051.

Sreenivasan, K. R. 1998 An update on the energy dissipation rate in isotropic turbulence. *Physics of Fluids* **10**, 528–529.

Sreenivasan, K. R. & Antonia, R. A. 1997 The phenomenology of small-scale turbulence. *Annual Review of Fluid Mechanics* **29**, 435–472.

Stouffer, S.D., Baker, N.R., Capriotti, D.P. & Northam, G.B. 1993 Effects of compression and expansion ramp fuel injector configuration on scramjet combustion and heat transfer. *AIAA Paper* .

Tavoularis, S, Corrsin, S & Bennett, JC 1978 Velocity-derivative skewness in small reynolds number, nearly isotropic turbulence. *Journal of Fluid Mechanics* **88** (1), 63–69.

Taylor, G.I. 1935 Statistical theory of turbulence. *Proceedings of the Royal Society of London. Series A, Mathematical and Physical Sciences* **151** (873), 421–444.

Taylor, GI 1938 Production and dissipation of vorticity in a turbulent fluid. *Proceedings of the Royal Society of London. Series A, Mathematical and Physical Sciences* pp. 15–23.

Tennekes, H. & Lumley, J. L. 1972 A first course in turbulence.

Tolstov, Georgi P 2012 *Fourier Series*. Courier Corporation.

Tucker, HJ & Reynolds, AJ 1968 The distortion of turbulence by irrotational plane strain. *Journal of Fluid Mechanics* **32** (04), 657–673.

Uberoi, M. S. & Mahinder, S. 1957 Equipartition of energy and local isotropy in turbulent flows. *Journal of Applied Physics* **28** (10), 1165–1170.

Uberoi, Mahinder S & Wallis, Stanley 1967 Effect of grid geometry on turbulence decay. *Physics of Fluids (1958-1988)* **10** (6), 1216–1224.

Vandsburger, U & Ding, C 1993 A self-excited wire method for control of the evolution of a turbulent mixing layer. *AIAA Paper* pp. 93–0443.

Vedula, P. & Yeung, P. K. 1999 Similarity scaling of acceleration and pressure statistics in numerical simulations of isotropic turbulence. *Physics of Fluids* **11**, 1208–1220.

Walker, Steven H, Sherk, Jeffrey, Shell, Dale, Schena, Ronald, Bergmann, John & Gladbach, Jonathan 2008 The darpa/af falcon program: the hypersonic technology vehicle# 2 (htv-2) flight demonstration phase. *AIAA Paper* **2539**, 2008.

Wang, J., Wang, L.-P., Xiao, Z., Shi, Y. & Chen, S. 2010 A hybrid numerical simulation of isotropic compressible turbulence. *Journal of Computational Physics* **229**, 5257 – 5279.

Williamson, J. H. 1980 Low-storage Runge-Kutta schemes. *Journal of Computational Physics* **35**, 48 – 56.

Wiltse, John M & Glezer, Ari 1998 Direct excitation of small-scale motions in free shear flows. *Physics of Fluids (1994-present)* **10** (8), 2026–2036.

Yakhot, V. & Sreenivasan, K. R. 2005 Anomalous scaling of structure functions and dynamic constraints on turbulence simulations. *Journal of Statistical Physics* **121**, 823–841.

Yamamoto, K. & Hosokawa, I. 1988 A decaying isotropic turbulence pursued by the spectral method. *Physical Society of Japan, Journal* **57**, 1532–1535.

Yeung, P. K., Brasseur, J. G. & Wang, Q. Z. 1995 Dynamics of direct large-small scale couplings in coherently forced turbulence - concurrent physical-space and fourier-space views. *Journal of Fluid Mechanics* **283**, 43–95.

Zwart, PJ, Budwig, R & Tavoularis, S 1997 Grid turbulence in compressible flow. *Experiments in Fluids* **23** (6), 520–522.